SATELLITE IMAGE PROCESSING USING DISCRETE FRACTIONAL TRANSFORMS

Thesis submitted in the partial fulfillment of requirement for the award of degree of

Master of Engineering

in

Electronics and Communication Engineering

Submitted by:

Rajinder Kumar

Roll No 801061022

Under the guidance of:

Dr. Kulbir Singh

Associate Professor

ELECTRONICS AND COMMUNICATION ENGINEERING DEPARTMENT

THAPAR UNIVERSITY

(Established under the section 3 of UGC Act, 1956)

PATIALA – 147004 (PUNJAB)

DECLARATION

I, Rajinder Kumar, hereby certify that the work which is being presented in this thesis entitled "SATELLITE IMAGE PROCESSING USING DISCRETE FRACTIONAL TRANSFORMS" by me in partial fulfilment of the requirements for the award of degree of Master of Engineering in Electronics and Communication Engineering from Thapar University (Deemed University), Patiala, is an authentic record of my own work carried out under the supervision of **Dr. Kulbir Singh**.

The matter presented in this thesis has not been submitted in any other University / Institute for the award of any other degree.

Date: 09/07/2012

Rajinder Kumar
Roll No. 801061022

It is certified that the above statement made by the student is correct to the best of my knowledge and belief.

Date: 09/07/2012

Dr. Kulbir Singh
Associate Professor, ECED
Thapar University, Patiala

Countersigned by:

Professor and Head ECED
Thapar University, Patiala
Date:

Dean of Academic Affairs
Thapar University, Patiala
Date:

ACKNOWLEGMENT

First of all, I give thanks to my **BABA Ji** - Supreme power for me, for providing me with the courage to express my deeply held spiritual beliefs in both my academic and professional endeavours. I am grateful for His Grace, Unconditional Love, and Forgiveness.

This Thesis would not have been possible without the unconditional support of my teacher and supervisor **Dr. Kulbir Singh**, Associate Professor, Electronics and Communication Engineering Department, Thapar University, Patiala. I am grateful for his unquestionable faith in my ability to achieve great things and for his wisdom and inspiration that forced me to push forward when the going got tough. I sincerely appreciated his candor, honesty and dedication. I am very lucky to have the opportunity to work with him. He has provided me help in technical writing and presentation style and I found this guidance to be extremely valuable.

I am very thankful to the Head of the Department, **Dr. Rajesh Khanna**, for his encouragement, support and providing facilities for the completion of this thesis.

I am also thankful entire faculty and staff members of Electronics and Communication Engineering Department for their unyielding encouragement. Also I would like to thanks ISRO for providing me a financial support during the course of work.

I greatly thank to all my friends for their gift of love, you are the fire that keeps my soul, spirit, love and passion aglow. You give meaning to my life.

Finally, I take this opportunity to express the profound gratitude from my deep heart to my beloved parents, my younger brother and sister for their love and continuous support – both spiritually and materially. Although they hardly understand what is research? And what a thesis is? Still they are willing to support any of my decisions. I take pride of myself being the son of such ideal parents and I put my head in the feet of my beloved parents for their sacrifice.

(Rajinder Kumar)

ABSTRACT

With the development of space technology, the huge amount of data generated by new generation satellites to be used for a variety of upcoming applications. In order to save storage space and channel bandwidth, remote sensing image must be compressed before transmitted from a spacecraft. To increase productivity, reduce cost, facilitate innovation and virtual collaborative environment for addressing new challenges there exist inherent security risk of unauthorized access. To fulfill such security and privacy needs in various applications encryption of data is required.

A lot of techniques are available for the above discussed applications and the hunger for improvement is underway. The fractional Fourier transform (FrFT) a generalization of Fourier transform (FT), introduced by Victor Namias in 1980 is an upcoming tool for the above applications because of an extra degree of freedom available to solve a problem [58]. With the advent of computers and enhanced computational capabilities the Discrete Fourier Transform (DFT) came into existence in evaluation of FT for real time processing. On similar lines, so there arises a need for discretization of FrFT. The Fractional transforms are almost in their infancy still having proved their worth to the optical and signal community by solving a variety of problems like, wave equation, Green's function associated with quantum mechanical harmonic oscillator, propagation in graded index medium, which remained unsolved by previous generation transforms [41].

Further the compression of satellite image data can be optimized using some feature which can be extracted by Fractional transforms by using fractional convolution and correlation which has been discussed by various authors [7], [24], [41]. The extra degree of freedom available with fractional transforms which gives an extra key for encryption and improved compression makes it an active research topic for satellite images. With variation of its parameter 'a', it is found that by using fractional transforms, high visual quality decompressed image can be achieved for same amount of compression. By varying 'a' to different values, an optimum value of 'a' can be achieved with low mean square error (MSE), better peak signal to noise ratio (PSNR) i.e. better quality of decompressed image. The two fractional transforms like DFrFT and DFrCT are used for the compression of satellite images. The performance of these transforms is compared based

on above said parameters i.e. MSE and PSNR. It has been observed that the performance of DFrFT is better than that of DFrCT. Moreover, the satellite images can be encrypted using fractional transforms which gives extra key for encryption provided by its fractional order. The performance of fractional transforms for satellite image encryption is compared based on PSNR and MSE. It has been observed that the value of PSNR is smaller for the case of DFrCT than that of DFrFT which proves the performance of DFrFT is better than DFrCT.

CONTENTS

LIST OF ABBREVIATION

AFT	Affine Fourier Transform
ASTER	Advanced Spaceborne Thermal Emission and Reflection Radiometer
BDC	Brightness Difference Compensation
BTC	Block Truncation Coding
CR	Compression Ratio
CT	Curvelet Transform
CCSDS	Consultative Committee for Space Data Systems
DAFT	Discrete Affine Fourier Transform
DCT	Discrete Cosine Transform
DFrCT	Disrete Fractional CosineTransform
DFrFT	Discrete Fractional Fourier Transform
DWT	Discrete Wavelet Transform
EROS	Earth Resources Observation System
ETM+	Enhanced Thematic Mapper Plus
FT	Fourier Transform
FFT	Fast Fourier Transform
FrCT	Fractional CosineTransform
FrFT	Fractional Fourier Transform
GIF	Graphical Interchange Format
GCCS	Global Command And Control System
HDTV	High Definition Television
IR	InfraRed
IDWT	Inverse Discrete Wavelet Transform
IFOV	Instantaneous Field Of View
JPEG	Joint Photographic Experts Group
JPEG2000	Joint Photographic Experts Group 2000
LZW	Lempel Ziv Welch

MS	Multi Spectral
MPW	Modified Patchwork-based Watermarking
MRA	Multi Resolution Analysis
MSE	Mean Square Error
MSS	Multispectral Scanner
NARA	National Archives Record Administration
NIMA	National Imagery and Mapping Agency
PSNR	Peak Signal-to- Noise Ratio
RBV	Return Beam Vidicon
RLE	Run Length Encoding
SW	Standing Wave
SLC	Scan Line Collector
SNR	Signal-to- Noise Ratio
SOM	Self-Organizing Map
TIFF	Tagged Image File Format
VCC	Vertex Chain Codes
USD	United States Dollars
USGS	United States Geological Survey

LIST OF FIGURES

LIST OF TABLES

CHAPTER-1
INTRODUCTION

1.1 SATELLITE IMAGES

The images captured by the new generation satellites are remotely sensed image used in weather reporting, regional planning, global positioning system, etc., also including fields of education welfare and intelligence as well [22]. These remotely sensed image data is to be communicated from remote area to receiver station, are facing with problem of storage and transmission of imagery data because of limited bandwidth, time of data transmission and increase in spatial resolution. Most of the satellites are operates on store-and-forward criterion; i.e. imagery is captured, stored on satellite and transmitted to ground station .This had increased the demand on storage because of lager volume of data is collected by high resolution satellite imagery system and requires more downlink time to transmit them to earth station.

Satellite images are very efficient for obtaining a better understanding of the earth's environment. They represent an important source of information for earth scientists. By reason of these, there is a constant growth not only in the number but also in the performance of remote sensing facilities, which larger amounts of data that have to be transmitted, processed and stored efficiently.

1.2 TYPES OF SATELLITE IMAGE

There are main three types of satellite images which are given below:

- Visible Satellite images
- Infrared Satellite images
- Water Vapor Satellite images

1.2.1 Visible Satellite Images

The visible channel of the satellite measures light using the same wavelengths as the human eye. In other words, looking at a visible satellite picture is the name as if an astronaut took a photo of the clouds and sent it to you. It can be shown in figure 1.1 (a). Visible satellite

pictures can only be viewed during the day, since clouds reflect the light from the sun. On these images, clouds show up as white, the ground is normally grey, and water is dark. In winter, snow-covered ground will be white, which can make distinguishing clouds more difficult. To help differentiate between clouds and snow, looping pictures can be helpful; clouds will move while the snow won't. Snow-covered ground can also be identified by looking for terrain features, such as rivers or lakes. Rivers will remain dark in the imagery as long as they are not frozen. If the rivers are not visible, they are probably covered with clouds. Visible imagery is also very useful for seeing thunderstorm clouds building. Satellite will see the developing thunderstorms in their earliest stages, before they are detected on radar. Objects with higher albedo (ability to reflect sunlight) appear brighter on the satellite image. Objects with lower albedo appear dark on the satellite image.

1.2.2 Infrared Satellite Images

Infrared satellite measures radiation output from the earth into space. In other words, it measures temperature and one can infer clouds based on the different temperatures being measured. It can be shown in figure 1.1 (b). The colder an item is, such as a high cloud or a cold air mass, the brighter it is. The warmer an item is, such as a warm lake or clouds near the ground, the darker it is. The sensors also measure heat radiating off the surface of the earth. Clouds will be colder than land and water, so they are easily identified. Infrared imagery is useful for determining thunderstorm intensity. Strong to severe thunderstorms will normally have very cold tops. Infrared imagery can also be used for identifying fog and low clouds. The fog product combines two different infrared channels to see fog and low clouds at night, which show up as dark areas on the imagery.

1.2.3 Water Vapor Satellite Images

Water vapor satellite measures radiation output just as infrared imagery does, but at a different wavelength (a wavelength of radiation that is heavily absorbed by moisture). Water vapor satellite pictures indicate how much moisture is present in the upper atmosphere (approximately from 15,000 ft to 30,000 ft). It can be show in figure 1.1 (c). The highest humidity will be the whitest areas while dry regions will be dark. Water vapor imagery is

useful for indicating where heavy rain is possible. Thunderstorms can also erupt under the high moisture plumes.

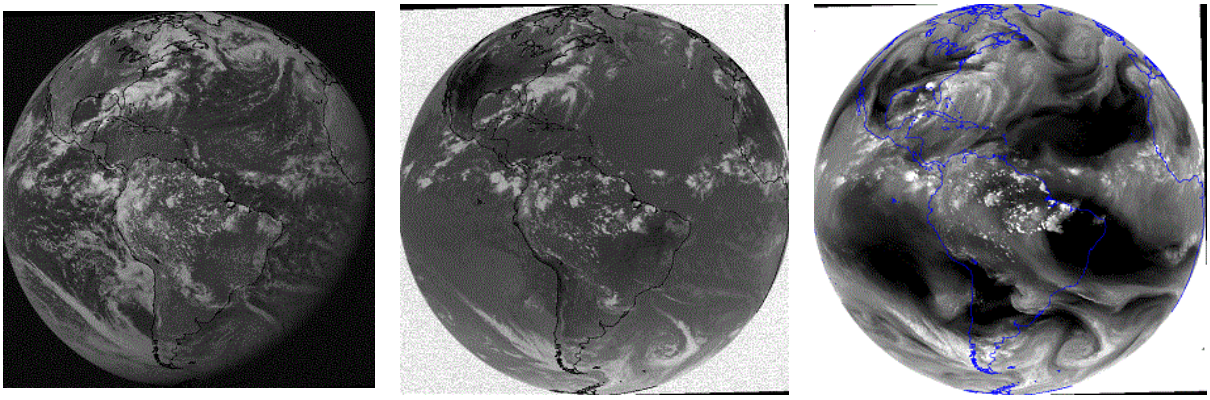

(a) Visible Satellite Image **(b) Infrared Satellite Image** **(c) Water Vapor Satellite Image**

Figure 1.1 Types of satellite Images

1.3 SATELLITE IMAGING SYSTEMS

A good understanding of the characteristics of satellite data should be developed in order to make best use of the information they contain. It is important to know their spectral characteristics to assess image quality for photointerpretation and for spectroradiometry studies. It is also important to appreciate their spatial characteristics particularly if these data are to be used in image analysis. The technical characteristics of image data must be well understood before image analysis begins.

Based on above discussed types of satellite images the following are the some satellite imagery systems are described as below.

1.3.1 Landsat 5 TM and Landsat 7 ETM+ Imagery

The Landsat program began in July 1972 with Landsat-1 and has operated continuously until the present day with Landsats 5 and 7. The Landsat Earth resources satellite system was the first designed to provide near global coverage of the Earth's surface on a regular and predictable basis. A description of how the multispectral data analysis technology, which has come to be synonymous with Landsat, was begun and how it developed and spread through to a broader research and user community is presented by Landgrebe in 1997 [56]. Four imaging systems have been flown on the Landsat satellites. These are the Return Beam

Vidicon (RBV), the Multispectral Scanner (MSS), the Thematic Mapper (TM), and the Enhanced Thematic Mapper Plus (ETM+). The RBVs were television camera-like instruments that captured image frames of 185Km x 185Km. Three RBV cameras were used in each Landsat 1(23/7/72-6/1/78) and Landsat 2 (22/1/75-27/7/83) satellites with different transmission filters (blue, red, near IR) and a spatial resolution of 79m. On Landsat 3 (5/3/78-7/9/83) two panchromatic RBVs were used, each with a data swath of 98km, overlapped to give 185 Km total. Thus, the spatial resolution was 40m. The MSS was the principal sensor on Landsat 1, 2 and 3. It has four wavelength bands (green, red, 2x near IR) with an additional thermal band in Landsat 3. The MSS isa mechanical scanning device, where six lines are simultaneously swept through an oscillating mirror, acquiring data by scanning the Earth's surface in strips normal to satellite's motion through 24 signal detectors (4 bands times 6 scan lines). The IFOV of each detector was 79Km x 79Km. However, it is sampled in time to produce discrete measurements across a scan line. The sampling rate corresponds to pixel centres of 56m giving a 23m overlap of the pixels. The IFOV of the MSS on Landsat 4 and 5 have been modified to 81.5m and 82.5m respectively. The pixel centre spacing of 56m has been retained.

The TM is a mechanical device like MSS, but with improved spatial, spectral and radiometric characteristics. Seven bands are used (blue, green, red, near IR, 2x mid IR, thermal) with 16 scan lines. The IFOV is 30 m x 30 m (120 m for the thermal band). It is included in Landsat 4 and 5. Landsat 4 (operated since 16/7/82) completed deorbiting manoeuvres in June 2001. Landsat 5 (operated since 1/3/84) will continue operations even in 2005 if there is enough funding. Landsat 6 failed to achieve orbit. In 1992, the US Congress authorised the procurement, launch and operation of a new Landsat satellite. On 15th April 1999, the Landsat 7 satellite was successfully launched. Landsat 7 was expected to have a unique and essential role in the realm of Earth observing satellites in orbit by the end of the 1990s. The Earth observing instrument on Landsat 7, the Enhanced Thematic Mapper Plus (ETM+), replicates the capabilities of the highly successful Thematic Mapper instruments on Landsat 4 and 5. The ETM+ also includes new features that make it a more versatile and efficient instrument than its predecessor for global change studies, land cover monitoring and assessment, and large area mapping. The primary new features on Landsat 7 are a panchromatic band with 15m spatial resolution, 5% absolute radiometric calibration, and a

thermal IR channel with 60m spatial resolution. The cost of a LANDSAT 7 level 1R scene covering a 185Km^2 area is 600 USD. The main mission of Landsat has always been the provision of environmental information. With a spatial resolution of 15 m in the panchromatic channel, Landsat could never be used as a substitute for aerial photography. However, the multispectral capability of Landsat can derive important environmental information that is of considerable value in archaeological landscape assessment explained by Drake et al. in 1999 [31]. It has been used to identify forest cover and change in Southern Madagascar by Clark et al. in 1998 [12]. It has been used in palaeoenvironmental studies in southern Tunisia combined with geomorphological and archaeological evidence and in the monitoring of the changing position of Nile Delta coastlines.

1.3.2 IKONOS Imagery

The IKONOS satellite was launched on 24th September 1999 with all detectors operable. It is the first of the new generation of high-resolution satellites, which was prepared by studies such as Ridley et al. in 1997 [43]. United States Dollars was launched into sun-synchronous orbit with an inclination of 98.1° to the equator at the altitude of 681 Km, and an orbital period of 98.3 minutes. Local crossing time at descending node is 10:30 a.m.

Unlike other sensors, IKONOS has the capability to collect data in either whiskbroom or pushbroom mode. The IFOV equates to 11 Km when at nadir and 13 Km off-nadir with 1 m spatial resolution. A contiguous area of 4700 sq. Km. can be acquired on a single pass in 128 sec with a GSD (Ground Sample Distance) of 1 m. In addition, IKONOS can image long stripes of 13 Km x 1000 Km for 1m GSD. Same pass stereo images can be acquired by pointing the sensor forward of nadir and then aft of nadir to create a stereo-pair. The satellite is designed to operate 120 minutes per day, but there were days of 200 minutes operation.

High resolution satellite data can provide: i) an alternative source of high resolution imagery to conventional aerial photography, ii) an alternative to topographic maps for field survey work in many developing countries and iii) a source of modern imagery to compare with historical CORONA data from the 1960s.

1.3.3 ASTER Imagery

ASTER (Advanced Spaceborne Thermal Emission and Reflection Radiometer) is an imaging

instrument that is flying on Terra, a satellite launched in December 1999 as part of NASA's Earth Observing System (EOS). ASTER is used to obtain detailed maps of land surface temperature, emissivity, reflectance and elevation. The EOS platforms are part of NASA's Earth Science Enterprise, whose goal is to obtain a better understanding of the interactions between the biosphere, hydrosphere, lithosphere and atmosphere.

1.3.4 HEXAGON KH-9 Imagery

On 14 August 2002, the NIMA delivered to NARA the original images from two more military satellites programs, the GAMBIT (with the KH-7 design satellite system), which is not examined in this thesis, and the HEXAGON (with the KH-9 design satellite system). NIMA gave a set of duplicate positives to NARA and a set of duplicate negatives to Earth Resources Observation System (EROS) Data Centre, where the public has access and may purchase them according to the prices below. The imagery that contains Israel is not declassified. The KH-9 system operated from March 1973 to October 1980. It flew 12 successful missions with durations from 42 to 119 days. It was a frame camera system, devoted solely to mapping, charting and geodesy. For each mission, it returned a single bucket of film to Earth. In total, it gave 29,000 frames, or 48,000 ft of film. The footprint on the ground was approximately 70x140 nautical miles (130x260Km)10. This image format increased the ground coverage and allowed for the creation of trilaps (three images of the same area), thus providing better control for height extraction. The ground resolution of KH-9 (6.00-9.00 m) may not be as good as KH-4B (1.80- 7.60 m), but the image is vertical and it is a frame camera. Also, most coverage of key control point areas was imaged in stereo and sometimes three times (called trilaps) on a single operation to give the geospatial analysts enough information to create precise maps and charts.

1.3.5 KOMSAT-2 Imagery

KOMPSAT-2 also known as Arirang 2, is a South Korean multipurpose satellite. It was launched from Plesetsk, Russia at 4:05 PM KST on 28 July 2006. It began to transmit signals at 11 PM the same day. Like the earlier Arirang-1 satellite, it takes its name from the popular Korean folk song Arirang. Its launch was the culmination of a project begun in 1999.

Arirang-2 orbits at a height of 685 kilometers, circling the Earth 14 times per day, and is expected to maintain that orbit for 3 years. It weighs 765 kilograms.

The satellite carries a high-powered digital camera which can distinguish to a 1-meter resolution, allowing the identification of individual vehicles on the ground. Among other purposes, this will allow the South Korean intelligence service to observe North Korean military activities. Prior to the launch of this satellite, the South Koreans had been largely dependent upon surveillance information provided by the United States. Spot Image is the distributor of KOMPSAT-2 imagery.

1.3.6 RapidEye Imagery

RapidEye is a German geospatial information provider focused on assisting in management decision-making through services based on their own Earth observation imagery. The company owns a five satellite constellation producing 5 meter resolution imagery that was designed and implemented by MacDonald Dettwiler (MDA) of Richmond, Canada. Originally located in Munich, the company relocated 60 km southwest of Berlinto Brandenburg an der Havel in 2004.

1.3.7 Cartsat 2 Imagery

Cartosat-2 is an Earth observation satellite in a sun-synchronous orbit. The satellite was built, launched and maintained by the Indian Space Research Organisation. Weighing around 680 Kg at launch, its applications will mainly be towards cartography in India. It was launched by the PSLV on January 10, 2007. Cartosat-2 carries a state-of-the-art panchromatic (PAN) camera that take black and white pictures of the earth in the visible region of the electromagnetic spectrum. The swath covered by these high resolution PAN cameras is 9.6 Km and their spatial resolution is less than 1 meter. The satellite can be steered up to 45 degrees along as well as across the track.

Cartosat-2 is an advanced remote sensing satellite capable of providing scene-specific spot imagery. The data from the satellite will be used for detailed mapping and other cartographic applications at cadastral level, urban and rural infrastructure development and management,

as well as applications in Land Information System (LIS) and Geographical Information System (GIS).

1.3.8 Indian Remote Sensing (IRS) Imagery

Indian Remote Sensing satellites (IRS) are a series of Earth Observation satellites, built, launched and maintained by Indian Space Research Organisation. The IRS series provides many remote sensing services to India. Indian Remote Sensing (IRS) satellite program to support the national economy in the areas of agriculture, water resources, forestry and ecology, geology, water sheds, marine fisheries and coastal management.

India established the National Natural Resources Management System (NNRMS) for which the Department of Space (DOS) is the nodal agency, providing operational remote sensing data services. Data from the IRS satellites is received and disseminated by several countries all over the world. With the advent of high-resolution satellites new applications in the areas of urban sprawl, infrastructure planning and other large scale applications for mapping have been initiated.

The IRS system is the largest constellation of remote sensing satellites for civilian use in operation today in the world, with 10 operational satellites. All these are placed in polar sun-synchronous orbit and provide data in a variety of spatial, spectral and temporal resolutions.

1.3.9 Pleiades Imagery

The Pleiades constellation is composed of two very-high-resolution optical Earth-imaging satellites. Pleiades 1 and Pleiades 2 will provide coverage of Earth's surface with a repeat cycle of 26 days. Designed as a dual civil/military system, Pleiades will meet the space imagery requirements of European defence as well as civil and commercial needs. Spot Image is the official and exclusive worldwide distributor of Pleiades products and services under a delegated public service agreement.

The Pleiades system is designed for a range of very-high-resolution (VHR) remote sensing applications which includes Land planning, Agriculture, Defense, Homeland Security, Forestry, Maritime and littoral surveillance and Civil Engineering/Asset Monitoring.

1.3.10 DMC-2 Surrey imagery

UK-DMC 2 is a British Earth imaging satellite which is operated by DMC International Imaging. It was constructed by Surrey Satellite Technology, based on the SSTL-100 satellite bus. It is part of Britain's contribution to the Disaster Monitoring Constellation, which is coordinated by DMC International Imaging. It is the successor to the UK-DMC satellite. The satellite has a mass of 120 Kilograms (260 lb) and a design life of five years. It carries a multi-spectral imager with a resolution of 22 metres (72 ft) and 660 Kilometres (410 mi) of swath, operating in green, red and near infrared spectra.

1.4 NEED FOR SATELLITE IMAGE COMPRESSION

Image compression is the art or science of efficiently coding digital images to reduce the number of bits required in the representing an image. The purpose of doing so is to reduce the storage and transmission costs while maintaining good quality. Now the new generated satellite are generate very high resolution images and these images require lager memory space for storing on satellite and large bandwidth for send it to satellite receiver at earth station. To store these images on satellite, and transmit them on earth station through downlink, compression in satellite image is required. Image compression addresses the problem of reducing the amount of data required to represent a satellite image. The underlying basis of the reduction process is the removal of redundant data. According to mathematical point of view, this amounts to transforming a two-dimensional pixel array into a statistically uncorrelated data set. The transformation is applied prior to storage or transmission of the image. At receiver, the compressed image is decompressed to reconstruct the original image or an approximation to it. The initial focus of research efforts in this field was on the development of analog methods for reducing video transmission bandwidth, a process called bandwidth compression. With the recent adoption of several key international image compression standards, the field is now poised for significant growth through the practical application of the theoretical work that began in the 1940s, when C.E. Shannon and others first formulated the probabilistic view of information and its representation, transmission, and compression. The example below clearly shows the importance of compression.

Let a digital image, 1024 pixel×1024 pixel×24 bit, without compression, would require 3 MB of storage and 7 minutes for transmission, utilizing a high speed, 64 kbits/s, ISDN line. If the image is compressed at a 10:1 compression ratio, the storage requirement is reduced to 300 KB and the transmission time drop to less than 6 seconds.

1.4.1 Principle behind compression

A common characteristic of most images is that the neighboring pixels are correlated and therefore contain redundant information. The foremost task then is to find less correlated representation of the image. Two fundamental components of compression are redundancy and irrelevancy reduction.

Redundancies reduction aims at removing duplication from the signal source (image/video).

Irrelevancy reduction omits parts of the signal that will not be noticed by the signal receiver, namely the Human Visual System.

In an image, which consists of a sequence of images, there are three types of redundancies in order to compress file size. They are:

- **Coding redundancy:** Fewer bits to represent frequent symbols.
- **Interpixel redundancy:** Neighboring pixels have similar values.
- **Psychovisual redundancy:** Human visual system cannot simultaneously distinguish all colors.

1.5 TYPES OF COMPRESSION TECHNIQUES

Compression can be divided into two categories, as Lossless and Lossy compression. In lossless compression, the reconstructed image after compression is numerically identical to the original image. In lossy compression scheme, the reconstructed image contains degradation relative to the original.

In the case of video, compression causes some information to be lost; some information at a detail level is considered not essential for a reasonable reproduction of the scene. This type of compression is called lossy compression. Audio compression on the other hand, is not lossy, it is called lossless compression. An important design consideration in an algorithm that causes permanent loss of information is the impact of this loss in the future use of the stored data.

Lossy technique causes image quality degradation in each compression/decompression step. Careful consideration of the human visual perception ensures that the degradation is often unrecognizable, though this depends on the selected compression ratio. In general, lossy techniques provide far greater compression ratios than lossless techniques.
The following are the some of the lossless and lossy data compression techniques:

1.5.1 Lossless coding techniques

- Run length encoding
- Huffman encoding
- Arithmetic encoding
- Entropy coding
- Area coding

1.5.2 Lossy coding techniques

- Predictive coding
- Transform coding (FT/DCT/Wavelets)

1.5.3 Applications

Over the years, the need for image compression has grown steadily. Currently it is recognized as an "enabling technology." It plays a crucial role in many important and diverse applications such as:

- Satellite images, where the data loss is undesirable because of image collecting cost.
- Medical images, where difference in original image and uncompressed one can compromise diagnostic accuracy.
- Remote sensing.
- Space and hazardous waste control applications.
- Control of remotely piloted vehicles in military.
- Facsimile transmission (FAX).

Image compression has been and continues to be crucial to the growth of multimedia computing. In addition, it is the natural technology for handling the increased spatial resolutions of today's imaging sensors and evolving broadcast television standards.

1.6 SATELLITE IMAGE ENCRYPTION

We are living in the information age, we need to keep information about every aspect for our lives. In other words, information is an asset that has a value like any other asset. As an asset, information needs to be secured from attacks. During the last two decades, computer networks created a revolution in the use of information. Authorized people can send and receive information from a distance using computer networks. To be secured, information needs to be hidden from unauthorized access (confidentiality), protected from unauthorized change (integrity), and available to an authorized entity, when it is needed (availability). Although the three previously mentioned requirements have not changed, they now have some new dimensions. Not only should information be confidential, when it is stored in a computer, there should also be away to maintain its confidentiality, when it is transmitted from one computer to another [9].

Information transmitted over computer networks nowadays is not only text, but also audio, image, and other multimedia types. The field of multimedia security has matured in the last decade to provide a class of tool-sets and design insights for the protection and enhancement of digital media under a number of diverse attack scenarios. Research in multimedia security was first motivated, in part, by the increasing use of digital means to communicate, store and represent entertainment information such as music and video. The digital form allowed the perfect duplication of information and almost seemless manipulation and tampering of the data. This created new types of security attacks not (as seriously) addressed in the past by the entertainment industry. The paradigm shift from analog to digital multimedia for entertainment has had an enormous impact for artists, publishers, copyright holders and consumers alike providing flexible and more accessible business models [34]. In such a setting, one natural question that arises is the security and confidentiality of a digital packet of multimedia information.

Satellite systems can provide extremely secure communications. They are both reliable and resilient and with the correctly considered encryption and security techniques they can be made highly secure. The satellite industry is constantly striving to make their communications more secure than ever. We all know how important it is to prevent ourselves from becoming victims of those who intercept our personal information. Our reliance on

satellites may not always be obvious but those systems that are in place to protect them, in turn protect us.

1.6.1 Principle behind encryption

The basic idea of encryption is to modify the message in such a way that only a legal recipient can reconstruct its content [53], [36]. A discrete-valued cryptosystem can be characterized by:

- a set of possible Image, P.
- a set of possible encrypted keys, K.
- a set of possible encryption and decryption transformations, E and D.

An encryption system is also called a cryptosystem. The message for encryption is called *plaintext*, and the encrypted message is called *ciphertext*. Denote the image and the encrypted image by P and C, respectively. The encryption procedure of a Image can be described as:

$$C = E_K (P) \qquad (2.1)$$

where *K* is the encryption key and *E* is the encryption function. Similarly, the decryption procedure is defined as:

$$P = D_K (C) \qquad (2.2)$$

where *D* is the decryption function. The security of a cipher should only rely on the decryption key *K*, since an adversary can recover the plaintext from the observed cipher text

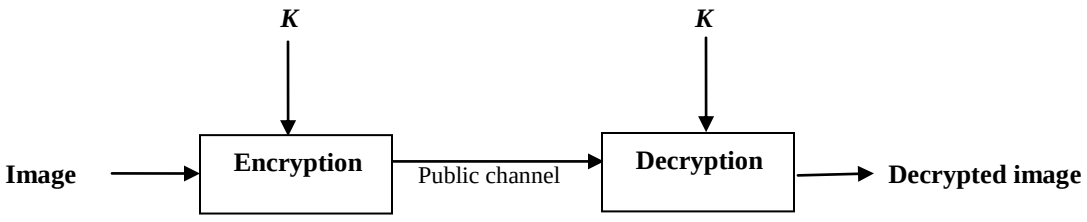

Figure 1.2 Encryption/Decryption Model

once he gets *K*. Figure 1.2 shows a block diagram for encryption/decryption of a cipher.

1.7 FRACTIONAL TRANSFORM

The Fourier transform is the most important tool used in signal processing and image processing. The fractional Fourier transform is representation of time and frequency domain. The fractional Fourier transform is the generalization of Fourier transform.

1.7.1 Development of FrFT

The FrFT, which is a generalization of the ordinary Fourier transform (FT), was introduced 75 years ago, but only in the last two decade it has been actively applied in signal processing, optics and quantum mechanics. The Fourier Transform (FT) is undoubtedly one of the most valuable and frequently used tools in signal processing and analysis. Little need be said of the importance and ubiquity of the ordinary Fourier transform in many areas of science and engineering. A generalization of Fourier Transform, the Fractional Fourier Transform (commonly referred as FrFT in available literature) was introduced in 1980 by Victor Namias [58] and it was established in the same year that the other transforms could also be fractionalized [59]. McBride and Keer explored the refinement and mathematical definition in 1987 [2]. In a very short span of time, FrFT has established itself as a powerful tool for the analysis of time varying signals [17], [23]. Furthermore, a general definition of FrFT for all classes of signals (one-dimensional & multidimensional, continuous & discrete and periodic & non-periodic) was given by Cariolario et al. in. But when FrFT is analyzed in discrete domain there are many definitions of Discrete Fractional Fourier Transform [11], [25], [48]. It is also established that none of these definitions satisfies all the properties of continuous FrFT. Santhanam and McClellan first reported the work on DFrFT in 1995. Thereafter within a short span of time a lot many definitions of DFrFT came into existence and these definitions are classified according to the methodology used for calculations in 2000 by S.C. Pie et al.

1.7.2 Applications

The FRFT has been found to have several applications in the areas of optics and signal processing and it also lead to generalization of notion of space (or time) and frequency domains which are central concepts of signal processing. FrFT has been related to a certain

class of wavelet transforms, to neural networks, and has also inspired the study of the fractional versions of many other transforms employed in signal analysis and processing.

FrFT has many applications in solution of differential equations [46], [58]-[59], optical beam propagation and spherical mirror resonators, optical diffraction theory, quantum mechanics, statistical optics, optical system design and optical signal processing, signal detectors, correlation and pattern recognition, space or time variant filtering, multiplexing, signal recovery, restoration and enhancement, study of space or time–frequency distributions etc.

It is believed that these are only a fraction of the possible applications. Despite the fact that most of the publications in this area have so far appeared in mathematics, optics, and signal processing journals, it is believed that the Fractional Fourier transform will have a significant impact also in other areas of science and engineering where Fourier concepts are used.

1.8 MOTIVATION

Firstly, due to high resolution, limited bandwidth and size of satellite imagery, there is strong motivation to compress the satellite images using fractional transforms. Secondly, satellite systems can provide extremely secure communications. The satellite industry is constantly striving to make their communications more secure than ever. So there is motivation towards the satellite image encryption using fractional transforms. The extra degree of freedom available with fractional transforms which gives an extra key for encryption and improved compression makes it an active research topic for satellite images.

1.9 OBJECTIVES OF THE THESIS

This thesis has following objectives:

(i) To achieves satellite image compression using discrete fractional Fourier transform and fractional Cosine transform.

(ii) To implement of different fractional transforms, for satellite image encryption.

(iii) To compare the performance of these transforms i.e. discrete fractional Fourier transform and discrete fractional Cosine transform.

1.10 ORGANIZATION OF THESIS

This thesis consists of total seven chapters which are organized as below:

Chapter 1: Introduction, it consist of brief introduction to satellite images, introduction to satellite image compression, satellite image encryption and fractional transforms, objectives and motivation behind research.

Chapter 2: Literature Survey, vigorous study of research papers of related fields in sequence has been discussed.

Chapter 3: Image compression and encryption techniques, in this chapter the basic image compression techniques i.e. lossless compression and lossy compression techniques are presented. A general compression model is also discussed. Also discussed the encryption techniques.

Chapter 4: Fractional transforms, this chapter describes the fractional transforms i.e. fractional Fourier and fractional Cosine transform. The discrete version of these transform also discussed with mathematical definitions.

Chapter 5: This chapter includes satellite image compression and results obtained from compression.

Chapter 6: This chapter describes the satellite image encryption and results obtained from encryption.

Chapter 7: Conclusion and Future Work: enlists the important conclusions and prospects of the future work

CHAPTER-2
LITERATURE SURVEY

In this chapter, the overview of the work, regarding satellite image processing, satellite image compression and satellite image encryption and fractional transforms has been done.

2.1 SATELLITE IMAGE PROCESSING

S. Sarmaha and Dhruba K. Bhattacharyya [54] propose a grid density based clustering method for detecting the clusters present in satellite images. High resolution and high dimensional satellite images cause problems for clustering methods due to clusters of different sizes, shapes and densities as they contain huge amount of data. Due to this reason, most algorithms for clustering satellite data sacrifice the correctness of their results for fast processing time. The processing time may be greatly influenced by the use of grids. The clustering is based on both the band values as well as the texture features in the satellite images. Experimental results are presented to establish the efficiency of this technique in detecting the clusters present in satellite images.

D. Kaimaris and P. Patias [16] purpose of this study is to determine the factors that facilitate or hinder the detection of buried structures through high spatial resolution satellite imagery. In this study, pan sharpened images from the QuickBird-2 satellite were used, of a spatial resolution of 0.60-0.70 m. This study concerns the detection of marks of the ancient Via Egnatia, from the ancient Amphipolis to Philippi (Eastern Macedonia, Greece). In this paper, authors studied different types of vegetation in the region and their phenological cycle. Taking into account the vegetation phenological cycle of the study area as well as the meteorological data, four pan sharpened QuickBird-2 images of a spatial resolution of 0.60–0.70 m. were used, during four different seasons. The application of this methodology in the study area had positive results, and not only was the main purpose of this study – the detection of parts of the ancient via Egnatia–achieved, but the locations of dozens of other buried archaeological remains were also determined.

M. Jahjah and C. Ulivieri [38] in this paper the method proposed by the authors rely on an object-oriented approach based on a theory for the analysis of spatial structures called mathematical morphology. The term ‘‘morphology’’ stems from the fact that it aims at analysing object shapes and forms. It is mathematical in the sense that the analysis is based on the set theory, integral geometry, and lattice algebra. Mathematical morphology has proven to be a powerful image analysis technique; two-dimensional grey tone images are seen as three-dimensional sets by associating each image pixel with an elevation proportional to its intensity level. The shape and size of the structuring element must be selected according to the morphology of the searched image structures. Other two feature extraction techniques were used, e Cognition and ENVI module SW, in order to compare the results. These techniques were applied to different archaeological sites in Turkmenistan (Nisa) and in Iraq (Babylon); a further change detection analysis was applied to the Babylon site using two HR images as a pre–post second gulf war. The discussion of these techniques has the objective to provide the archaeological team with new instruments for the orientation and the planning of a remote sensing application.

B. Purna Kumaria and V.P. Subramanyam Rallabandi [8] propose a modified patchwork-based watermarking (MPW) scheme in the spatial domain because a major global satellite data provider, National Remote Sensing Agency, Department of Space, Government of India, needs to protect copyright associated with the data . The proposed MPW algorithm is capable of embedding a watermark with minimal manipulation of the original image pixel values. The watermark contains information about the provider and the intended recipient of the data. The MPW watermark embedding process does not create any visual artifacts and is imperceptible. The watermark retrieval process operates with the help of a key and does not require the original image. Our results demonstrate that the presented scheme successfully incorporates copyright requirements for satellite imagery.

J. Grazzini et al. [28] discuss about the use of computer vision tools for automatically analyzing the large amount of data acquired by remote sensing has grown in importance and number of different applications, ranging from basic research to industry. However, images displaying natural phenomena, especially turbulence, develop following complicated patterns

which are difficult to segment and to analyze with those tools. In this paper, the authors discuss on the use of new image processing methods to describe complicated flow and flow-like quantities, in applications such as meteorology. This paper show that this methodology can be further exploited in order to derive information about a dynamical property from still infrared images. Namely, the main goal of our study is to detect and characterize textural areas at which typical convective movements take place. For that purpose, they compare the actual graylevel distribution in images, providing information about the temperature distribution, and a synthetic graylevel distribution induced by the multifractal formalism, also reinterpreted by its connection with thermodynamics.

F. Nencini et al. [20] presents an image fusion method suitable for pan-sharpening of multispectral (MS) bands, based on non-separable multi resolution analysis (MRA). The low-resolution MS bands are resampled to the fine scale of the panchromatic (Pan) image and sharpened by injecting high pass directional details extracted from the high-resolution Pan image by means of the curvelet transform (CT). CT is a non-separable MRA, whose basis functions are directional edges with progressively increasing resolution. The advantage of CT with respect to conventional separable MRA, either decimated or not, is twofold. Firstly, directional detail coefficients matching image edges may be preliminarily soft-thresholded to achieve a noise reduction that is better than that obtained in the separable wavelet domain. Secondly, modeling of the relationships between high-resolution detail coefficients of the MS bands and of the Pan image is more fitting, being accomplished in the directional multiresolution domain. Experiments are carried out on very-high-resolution MS + Pan images acquired by the QuickBird and Ikonos satellite systems. Depending on the datasets, however, the performance ranking of fusion methods may be different. In particular, on the Ikonos dataset the proposed method outperforms the Gram–Schmidt spectral sharpening method, which is implemented in the software package ENVI and constitutes the baseline algorithm from which commercial Pan-sharpened products are achieved.

K. Rajesh et al. [32] propose a non-causal eight neighborhood image restoration model based on autocorrelation and triple correlation functions of the noise corrupted satellite image. The image reconstruction is being done by the estimated parameters. In addition to

image smoothing, the edges are also preserved while reconstruction. A quantitative analysis of the restored images is also carried out by comparing the features of modeled images with that of shift-variant regularization approach. The non-causal modeling scheme used shows encouraging results for noise removal. It has been observed that HOS sharpens the edge pixels and reduces image blurring problem thus obviating usually associated problems with traditional spatial domain filters. Quantitative assessment of modeled outputs has been done by evaluating its mean, standard deviation, fractal dimension and entropy. When compared with the features of shift-variant regularization approach, the results are found to be fairly good.

A.J. Richardson et al [3] describe the self-organizing map (SOM), a type of artificial neural network adept at pattern identification. The ability of the SOM to extract patterns from a variety of satellite data, including scatterometer and thermal imagery, is illustrated by example. The authors characterize inter-annual, seasonal and event-scale variability by using the SOM and relate the output to auxillary variables by using a number of techniques that enhance interpretation. Practical recommendations for the fruitful application of SOMs are given. Although the SOM has only rarely been used in oceanography previously, it is a promising applied mathematical tool for pattern extraction from many types of data, especially large and complex satellite data sets. An advantage of SOMs over other multivariate techniques is that the algorithm is robust in handling missing data, without a priori estimation.

2.2 SATELLITE IMAGE COMPRESSION

X. Delaunay et al. [60] propose a novel compression scheme to perform better than the Consultative Committee for Space Data Systems (CCSDS) standard while preserving low complexity and easy rate control. In the proposed scheme the three level DWT decomposition is applied to an images and then further redundancies between the DWT coefficients is exploited with further transformed independently. For an on-board satellite compression application, processing small blocks is less memory intensive and requires less computational capabilities. Blocks of size 4x4 are circularly shifted according to nine different orientations before DCT derivation. The best orientation is selected by optimization

of a rate-distortion criterion. The optimization requires the derivation of the nine possible shifts and their associated DCT on each block. Results compares the performance of the post-transform with the Hadamard basis and bandelet transform with 15 bases to the CCSDS and JPEG2000 coder at bit- rates close to the targeted bit-rate of 2.0 bpp. JPEG2000 scan-based results may be around 0.6 dB better than those of the CCSDS. Thus, with a post- transform compression scheme having a low complexity, the results obtained may be only around 0.5 dB lower than those of JPEG2000 in scan-based.

I. Hacihaliloglu and M. Kartal [26] discuss this study aims to compare most of the well-known compression techniques namely discrete cosine transform and discrete wavelet transform because with the improvement of synthetic aperture radar technology, larger areas are being imaged and the resolution of the images has increased. Larger images have to be transmitted and stored. So these techniques make compression of SAR images with minimal loss of information important. It investigates RADARSAT and SPOT images of different regions of different characteristics. The studies showed that compression ratios changed according to the pixel classification. The second purpose of this study is to compare the two compression algorithms. The DWT based algorithm gave the minimum Mean Square Error compared to the DCT bared compression algorithm. The results changed according to the quantization process and the transform-coding algorithm.

Guoxia Yu et al. [21] proposed an automatic onboard multispectral image compression system, for LEO Earth Observation satellites. This system has combined tiling, sub-pixel band registration, radiometric calibration, and multispectral image compression, to achieve automatic on-board image processing requirement. Two radiometric calibration methods are compared, and Brightness Difference Compensation (BDC) is preferred. A new robust band registration technique, which is gradient image based phase correlation (GradPC), is proposed. Experimental work based on natural satellite test images is given and results validate the system design.

Chien-Wen Chen et al. [14] a near lossless image compression algorithm is presented for high quality satellite image compression. The proposed algorithm makes use of the

recommendation for image data compression from the Consultative Committee for Space Data Systems (CCSDS) and specific residue image bit-plane compensation. Comparing with the recommendation for satellite image compression from CCSDS, the proposed algorithm can reconstruct near lossless images with less bit rate than the recommendation of CCSDS does. Benefited from run-length coding and specific residue image bit-plane compensation, the proposed algorithm can obtain higher quality satellite image at similar bit rate or lower bit rate at the similar image quality. These results are valuable for reducing transmission time of high quality satellite image data. This work can be further improved by combining other binary compression techniques and the extension of this work may offer a VLSI or a DSP implementation of the proposed algorithm. Satellite image transmission and storage system can benefit by the proposed algorithm.

M. Liu et al. [37] explain that the aim of data compression techniques is to reduce the amount of data needed to accurately represent an image, such that this image can be economically transmitted or received. Increasing the bandwidth is another method, but the cost sometimes makes this a less attractive solution. The easiest way to reduce the size of the image file is to reduce the size of the image itself. By shrinking the size of the image, fewer pixels need to be stored and consequently the file will take less time to load. The problem with this is that if an image file is reduced the quality of the image is reduced. Thus two types of image compression exists "Lossless "and "Lossy" compression. Currently Digital Video Interface, Joint Photographic Experts Group (JPEG), and Motion Pictures Experts Group (MPEG) are the three compression techniques that are widely used. In general, lossy techniques provide far greater compression ratios than lossless techniques.

Tsung-Han Tsai et al. [56] presents EBCOT algorithm exhibits state-of-the-art compression performance while producing a bit-stream with a rich set of features, including resolution and SNR scalability together with a "random access" property. The algorithm has modest complexity and is suitable for applications involving remote browsing of large compressed images. The algorithm lends itself to explicit optimization with respect to MSE as well as more realistic psychovisual metrics, capable of modelling the spatially varying visual masking phenomenon. While EBCOT has the best

compression rate of all and is adopted by JPEG2000, it requires much more complex multi-layer coding procedures, multiple coding tables and arithmetic coding techniques. These make the hardware implementation of EBCOT codec more difficult and expensive.

S. A. Corona et al. [47] proposes Bi Level image compression based on both chain codes and entropy encoders. In this paper author claims that there exist a higher degree correlation between adjacent pixels that causes dependencies among the chain coders. The first techniques employ three symbol instead of five symbol in previous scheme developed by Bribiesca and is known as three orthogonal directional chain codes(3OT) comprise of three symbol{0,1,2}. The second chain codes techniques also developed by Bribiesca and is known as Vertex Chain Codes (VCC). VCC codes represent the number of connecting vertices between two adjacent boundary pixels and also comprise of three symbol{0,1,2}.The third techniques uses eight symbol that represent the relative angle change that occurs while moving between contiguous boundary pixels and is known as Angled Freeman 8 (AF8) chain codes comprise of symbol {0,1,2,3,4,5,6,7}.

C. Saravanan et al. [13] a new compression technique proposed to achieve more compression ratio by reducing number of source symbols. The source symbols are reduced by applying source symbols reduction and further the Huffman coding is applied to achieve compression. The source symbols reduction technique reduces the number of source symbols by combining together to form a new symbol. Therefore, the number of Huffman code to be generated also reduced. The Huffman code symbols reduction achieves better compression ratio. The experiment has been conducted using the proposed technique and the Huffman coding on standard images. This paper analyzed and shows that the newly proposed compression technique achieves 10% more compression ratio than the regular Huffman coding.

M. Sharma et al. [39] compares the Huffman algorithm with other common compression techniques like Arithmetic, Lempel Ziv Welch (LZW) and Run Length Encoding (RLE). These techniques for compression are compared on the basis of their use in different applications and their advantages and disadvantages. This paper concluded that arithmetic

coding is very efficient for more frequently occurring sequences of pixels with fewer bits and reduces the file size dramatically. RLE is simple to implement and fast o execute. LZW algorithm is better to use for tagged image file format (TIFF), graphical interchange format (GIF) and Textual Files. It is easy to implement, fast and lossless algorithm whereas Huffman algorithm is used in JPEG compression. It produces optimal and compact code but relatively slow. Huffman algorithm is based on statistical model which adds to overhead. The above discussed techniques use lossless compression technique.

U. B. Shankar et al. [57] explain the techniques for image compression. Image compression is achieved by exploiting redundancies in the image. These redundancies could be spatial, spectral, or temporal redundancy. The techniques for image compression are Huffman coding & Run length encoding. Run-length coding is a scheme for image compression that exploits special redundancies. It is very easy to implement, but would not necessarily reduce the size of image. Greater compression ratio is achieved in crowded image using RLE. Huffman coding is widely utilized in hardware as well as software coders for commercial application. This is minimum redundancy and optimal code. Compression ratio is higher than RLE. Huffman coding can provide optimal compression and error free decompression.

J. H. Pujar et al. [30] proposed the Lossless method of image compression and decompression using a simple coding technique called Huffman coding. This technique is simple in implementation and utilizes less memory. A software algorithm has been developed and implemented to compress and decompress the given image using Huffman coding techniques in a MATLAB platform. This paper concludes that Huffman coding is efficient technique for image compression and decompression to some extent & the result of the decompressed image is almost same as that of the input image so that indicates that there is no loss of information during transmission.

R. Hassan et al. [45] present a novel technique that subdivides the original symbol sequence into two or more subsequences. We then apply Huffman coding on each of the subsequences. This proposed scheme gives approximately 10-20% better compression in comparison with that of straightforward usage of Huffman coding. The results from the proposed method of

sub dividing a block for coding are encouraging. Some researchers have previously tried to split the dataset recursively; however we found that subdividing the dataset at most into three sub-blocks results in better compression of the dataset. The proposed method can be used in any lossless image data compression.

D. Anil et al. [15] proposed a modified three level block truncation coding for Image compression. Block Truncation Coding (BTC) is a lossy data compression technique used for compression of images. BTC is a simple and fast image compression algorithm with less computational complexity than former schemes proposed. In this paper author makes use of one bit to express the result of quantizing p_i unlike the two bits used in the conventional three level BTC. The proposed methodology for BTC gives more compression ratio as well as very less PSNR when compared to the conventional three-level BTC. The MSE and the PSNR for lena image is 118.454 and 27.3953 respectively as compare to conventional three level BTC is 195.2842 and 25.224 respectively. Bit rate for this BTC is also lower than the conventional BTC. The average of MSE of all the images for the conventional three-level BTC is 181.4601 which is far greater than that of the proposed three-level BTC.

K. Singh et al. [46] in this paper, Wavelet Transform, fractional Fourier transform and fractional Cosine Transform (FrCT) are compared using Mean Square Error and Peak signal-to- Noise Ratio in the field of image compression. Wavelet provides better MSE and PSNR at lower Compression Ratio (CR), whereas FrFT provides good result at higher compression ratio and FrCT provides same results as that of Wavelet at higher CR. In conclusion, Daubechies wavelet provides better PSNR, less MSE and high compression ratios compared to other Wavelets and the techniques used for image compression FrFT and FrCT make full use of the additional parameter ‘a’ to achieve better PSNR, less MSE and high compression ratio.

I. S. Yetik et al. [27] discuss the application of Fractional Fourier transform based filtering configurations to image representation and compression. An image can be approximately represented (and stored or transmitted) as the coefficients of the minimum mean square filtering configuration approximating the image matrix. In this paper, there is a novel way of

representing images based on Fractional Fourier domain filtering configurations, leading to a method for image compression.

2.3 SATELLITE IMAGE ENCRYPTION

M. Usama et al. [40] propose a new chaos-based symmetric-key encryption technique for satellite imagery. This scheme utilizes multiple chaotic maps e.g. Logistic, Henon, Tent, Cubic, Sine and Chebyshev for enhancing the key space, robustness and security of satellite imagery. Authors perform key sensitivity, statistical and performance analysis experiments to determine the security, reliability, and speed of our algorithm for satellite imagery. The proposed algorithm presents several interesting features, such as a high level of security, large enough key space, pixel distributing uniformity and an acceptable encryption speed as compared to AES, 3-DES, and DES. According to the comparative, theoretical and experimental results, it conclude that the proposed chaos-based satellite image cryptosystem is useful for real-time satellite image encryption and decryption, in order to keep the storage and transmission process secure and reliable. The proposed system is not just limited to this area, but can also be widely applied in the secure storage and transmission of confidential multimedia images over the Internet and/or any shared network environment.

A. S. Alghamdi et al. [5] introduces a technique for the encryption and decryption of satellite imagery in order to securely transmit it during the war. Global command and control system (GCCS-Joint) is a command, control, communications, computers and intelligence (C4I) system which consists of hardware, software, procedures and standards and which provides directory services, enterprise services and security services by exchanging imagery, intelligence, status of forces and planning information. In order to secure this exchange of imagery and information, we need more secure techniques and algorithms to be implemented. During the war, the commanders and forces needs the information and images of the exact location to which they are going to target and these images can be easily taken from the satellite. But the main problem of these satellite images is its transmission over the unsecure electronic media. The research work is carried out by using the Henon and logistic maps.

X. Zhang et al. [61] propose a new image encryption algorithm for remote sensing images in hybrid domains. This algorithm makes full use of the advantages of image encryption in both spatial domain and transform domain. First, the low-pass subband coefficients of image DWT (discrete wavelet transform) decomposition are sorted by a PWLCM system in transform domain. Second, the image after IDWT (inverse discrete wavelet transform) reconstruction is diffused with 2D (two-dimensional) Logistic map and XOR operation in spatial domain. The experiment results and algorithm analyses show that the new algorithm possesses a large key space and can resist brute-force, statistical and differential attacks. Meanwhile, the proposed algorithm has the desirable encryption efficiency to satisfy requirements in practice. Therefore, this algorithm is meant to be a good candidate to ensure the security of remote-sensing image transmission.

2.4 FRACTIONAL TRANSFORMS

V. Namias [58] introduced the concept of Fourier transforms of fractional order, the ordinary Fourier transform being a transform of order 1. The integral representation of this transform can be used to construct a table of fractional order Fourier transforms. A generalized operational calculus is developed, paralleling the familiar one for the ordinary transform. Its application provides convenient technique for solving the certain class of ordinary and partial differential equations which arise in quantum mechanics from classical quadratic Hamiltonians. The method of solution is first illustration its application to the free and to the force quantum mechanical harmonics oscillator. The corresponding Green's functions are obtained in closed form. The new techniques are extended for 3-dimensional problems and applied to the quantum mechanical description of motion of electrons in a constant magnetic field. The stationary states, energy level and evolution of initial wave are packet are obtained by systematic application rules of generalized operational calculus.

L. B. Almeida [33] introduced the FrFT and number of its properties and some new results: interpretation as the rotation in time frequency plane and the FrFT's relationship with the time-frequency representation such as the Wigner distribution, ambiguity function, the short time Fourier transform and its spectrogram. The relationship has very simple and natural form and supports the FrFT's interpretation as rotation operation. In this paper some

examples of FrFT of simple signals are given. And also explain the example of its applications, showing how the use of FrFT allows a treatment of swept-frequency filters that is very similar to classical treatment of shift-invariant filter with the Fourier transform. The author presented the extension of Fourier transform which is designated as fractional Fourier transform. The linear transform depends upon the parameter alpha and can be interpreted as a rotation by angle alpha in time frequency plane.

S. C. Pei and M. H. Yeh [48] exploring the continuous fractional Fourier transform (FrFT) represents a rotation of signal in time-frequency plane, and it becomes an important tool for signal analysis. A discrete version of fractional Fourier transform has been developed but its results do not match those of continuous case. In this paper, authors propose a new version of discrete fractional Fourier transform (DFrFT). This new DFrFT will provide similar transforms as those of continuous fractional Fourier transform and also hold the rotation properties. This DFrFT provide a method for implementing DFrFT in digital electronic system.

C. Candan et al. [11] propose and consolidate a definition of the discrete fractional Fourier transform that generalizes the discrete Fourier transform (DFT) in the same sense that the continuous fractional Fourier transform generalizes the continuous ordinary Fourier transform. This definition is based on a particular set of eigenvectors of the DFT matrix, which constitutes the discrete counterpart of the set of Hermite–Gaussian functions. The definition is exactly unitary, index additive, and reduces to the DFT for unit order. One of the most interesting avenues for future research is the establishment of the relationship of the discrete fractional Fourier transform with the discrete Wigner distribution. It might expect the study of the relationship of the Wigner distribution with the fractional Fourier transform to contribute to the establishment of a definitive definition of the discrete Wigner distribution, leading to a consolidation of the theory of discrete time-frequency analysis.

S. C. Pei and J. J. Ding [51] introduced a new type of DFrFT, which are unitary, reversible, and flexible; in addition, the closed-form analytic expression can be obtained. The discrete fractional Fourier transform (DFrFT) is the generalization of discrete Fourier transform.

Many types of DFrFT have been derived and are useful for signal processing applications. It works in performance similar to the continuous fractional Fourier transform (FrFT) and can be efficiently calculated by FFT. Since the continuous FrFT can be generalized into the continuous affine Fourier transform (AFT) so-called canonical transform, they also extend the DFRCT into the discrete affine Fourier transform (DAFT). They will derive two types of the DFrFT and DAFT. Type 1 will be similar to the continuous FRFT and AFT and can be used for computing the continuous FrFT and AFT. Type 2 is the improved form of type 1 and can be used for other applications of digital signal processing. Meanwhile, many important properties continuous FrFT and AFT are kept in closed-form DFrFT and DAFT, and some applications, such as the filter design and pattern recognition, will also be discussed. The closed-form DFrFT they introduce will have the lowest complexity among all current DFrFT's that are still similar to the continuous FrFT.

S. C. Pei and M. H. Yeh [49] develops a 2D-DFrFT which can preserve the rotation properties and provide similar results to continuous FrFT. Fractional Fourier transform (FRFT) performs a rotation of signals in the time-frequency plane, and it has many theories and applications in time-varying signal analysis. Because of the importance of fractional Fourier transform, the implementation of discrete fractional Fourier transform will be an important issue. Recently, a discrete fractional Fourier transform (DFrFT) with discrete Hermite eigenvectors has been proposed, and it can provide similar results to match the continuous outputs. On the other hand, the two dimensional continuous fractional Fourier transform is also proposed for 2D signal analysis.

CHAPTER-3

IMAGE COMPRESSION AND ENCRYPTION TECHNIQUES

3.1 FUNDAMENTALS

The term data compression refers to reducing amount of data required to represent a given amount of information. There should be a clear distinction between data and information. In fact, data are the form of information representation. Thus the same information may be represented by completely different data. If certain information has two representations differing in size, one of them is said to have data redundancy [44]. The data redundancy is a quantifiable entity. If n_1 and n_2 are the number of information units in two data sets representing the same information, the relative data redundancy R_D of the first data set (the one characterized by n_1) is defined as

$$R_D = 1 - \frac{1}{C_R} \tag{3.1}$$

where C_R commonly called the compression ratio, is

$$C_R = \frac{n_1}{n_2} \tag{3.2}$$

For the case $n_1 = n_2$, $C_R = 1$ and R_D indicating that (relative to the second data set) the first representation of the information contains no redundant data.

When $n_2 << n_1$, C_R and, R_D implying significant compression and highly redundant data. In the final case, $n_2 >> n_1$, C_R and R_D indicating that the second data set contains much more data than the original representation. This is of course, is the normally undesirable case of data expansion. In general C_R and R_D, lie in the open intervals $(0,\infty)$ and $(-\infty, 1)$ respectively. A compression ratio 8:1 means that the first data set has 8 information carrying units per every 1 unit in the second or compressed data set. The corresponding redundancy of 0.875 implies that 87.5 percent of the data in the first data set is redundant.

3.2 IMAGE COMPRESSION

The rapid growth of digital imaging applications, including desktop publishing, multimedia, teleconferencing and high definition television (HDTV) has increased the need for effective and standardized image compression techniques [44]. Image data compression aims at taking

advantage of this redundancy to reduce the number of bits required to represent an image. Basic image compression techniques are of two types these are lossless compression techniques and lossy compression techniques. These techniques are used for reducing the amount of data required to represent an image are lossless compression and lossy compression. In both of these techniques one or more redundancies as discussed in last chapter is removed.

Image encryption is one of the most important applications in transferring images through the internet and cellular phones, as well as being important in encryption of the satellite images. The amount of visual information available in digital format has grown exponentially in recent years. Retrieving particular images in a way that is both effective and efficient remains an open problem. With the further development of multimedia technologies and the rapid spread of computer networks, the rapid development of computer communication and the Internet makes it very easy to loose exchange data via networks . Internet and wireless networks offer powerful channels to deliver and exchange images. The increased popularity of image exchange places a great demand on efficient image storage and transmission techniques. The major hurdle for allowing much broader access of digital images lies in how to make sure that an image is used for its intended purpose by its intended recipients. Sensitive and confidential information is vulnerable to various kinds of misuse when data in or transmitted to/from computer system, then the development of secure management usage of digital images becomes one of the important applications in image processing. The wide use of digital images and videos in various applications brings serious attention to the security and privacy issues today. Many different encryption algorithms have been issues today. Many different encryption algorithms have been proposed in recent years as possible solutions to the production of digital images and videos.

3.3 A GENERAL IMAGE COMPRESSION MODEL

A general compression model is shown in figure 3.1. It shows that encoder and decoder consist of two relatively independent functions or sub blocks. The encoder is made up of source encoder, which removes input redundancies and a channel encoder, which increases the noise immunity of the source encoder's output. Similarly, the decoder includes a channel decoder followed by a source decoder. If the channel between the encoder and decoder is noise free, the

channel encoder and decoder are omitted, and the general encoder and decoder is noise free, the channel encoder and decoder are omitted, and the general encoder and decoder become the source encoder and decoder, respectively.

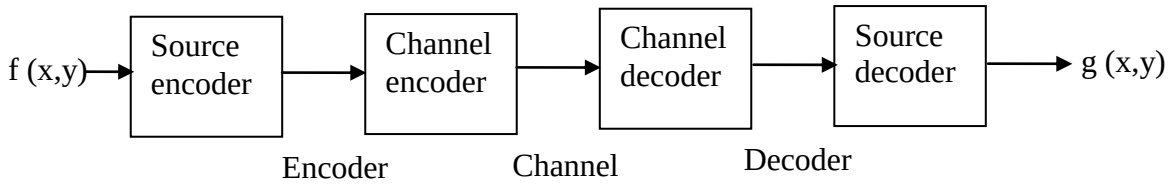

Figure 3.1 General Compression Model

3.3.1 Source Encoder

The source encoder is responsible for reducing or eliminating any coding, interpixel, or

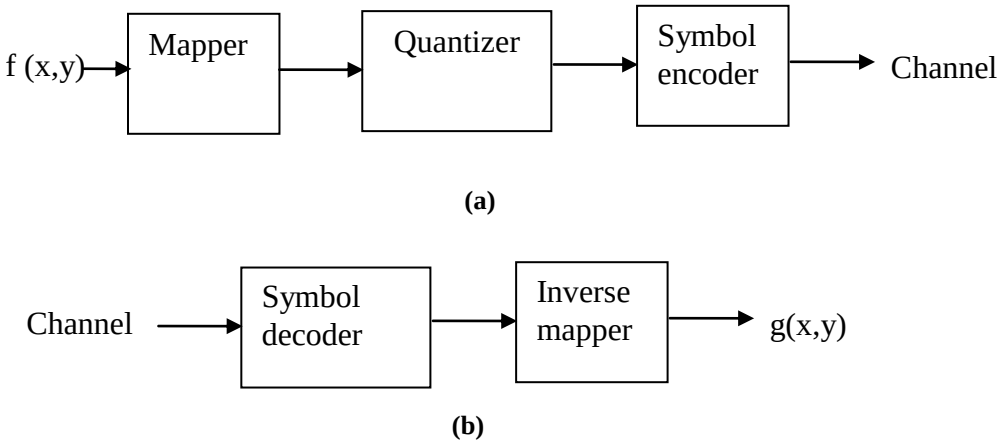

Figures 3.2 (a) Source encoder (b) Source decoder

psychovisual redundancies in the input image. The specific application dictates the best encoding approach. Normally, the approach can be modeled by a series of three independent operations. Operation is designed to reduce one of the three redundancies discussed earlier.

3.3.2 Mapper

In the first stage of the source encoding process, the mapper transforms the input data into a (usually non-visual) format designed to reduce interpixel redundancies in the input image. This operation generally is reversible and may or may not reduce directly the amount of data required to represent the image.

3.3.3 Quantizer

The second stage or quantizer block reduces the accuracy of the mapper's output in accordance with some pre-established fidelity criterion. This stage reduces the Psychovisual redundancies of the input image. This operation is irreversible. Thus, it must be omitted when error-free compression is desired.

3.3.4 Symbol Encoder

In the third and final stage of source encoding processes, the symbol coder creates a fixed or variable-length code to represent the quantizer output and maps the output in accordance with the code. The term symbol coder distinguishes this coding operation from the overall source encoding processes. In most cases, a variable length code is used to represent the mapped and quantized data set. It assigns the shortest code words to the most, frequently occurring output values and thus reduces coding redundancy. The operation is completely reversible. Upon completion of symbol coding step, the input image has been processed to remove each of the three redundancies discussed earlier. It is shown that the source encoding processes consist three successive operations, but all three operations are not necessarily included in every compression. For example, the quantizer must be omitted when error free compression is desired. In addition, some compression techniques normally are modeled by merging blocks that are physically separate in figure 3.2 (a).

3.3.5 Source Decoder

The source decoder shown in figure contains only two components: a symbol decoder and an inverse mapper. These blocks perform, in reverse order, the inverse operations of the source encoder's symbol encoder and mapper blocks. Because quantization results in irreversible information loss, an inverse quantizer block is not included in the general source decoder model shown in the figure 3.2 (b).

3.3.6 Channel Encoder and Decoder

The channel encoder and decoder play an important role in the overall encoding-decoding process when the channel of above figure 3.1 is noisy or prone to error. They are designed to reduce the impact of channel noise by inserting a controlled form of redundancy into the

source-encoded data. As the output of the source encoder contains little redundancy, it would be highly sensitive to transmission noise without the addition of this "controlled redundancy".

3.4 LOSSLESS IMAGE COMPRESSION TECHNIQUES

In lossless compression, the reconstructed image after compression is numerically identical to the original image on the pixel-by-pixel basis [35]. Lossless compression is sometimes preferred for artificial images such as technical drawings, icons or comics. This is because lossy compression methods, especially when used at low bit rates, introduce compression artifacts. Lossless compression methods may also be preferred for high value content, such as medical imagery or image scans made for archival purposes [42]. Lossless methods yield lower compression ratios but preserve every pixel in the original image. In lossless compression scheme, the reconstructed image after compression, is numerically identical to the original image, i.e. original image can be reconstructed without any errors. However lossless compression can only achieve modest amount of compression. This is important for applications like compression of text. It is very important that the reconstruction is identical to the original text, as very small differences can result in statements with very different meanings.

Consider the sentences, **"You can now send money"** and **"You can not send money"**. A similar argument holds for computer files and for certain types of data such as bank records. Various techniques for lossless compression are below:

3.4.1 Run Length Coding

Run length encoding is a very simple method for compression of sequential data. It takes advantage of the fact that, in many data streams, consecutive single tokens are often identical. Run-length encoding is a simple method to encode long runs of the same symbol. Run length encoding checks the stream for this fact and inserts a special token each time a chain of more than two equal input tokens are found. This special input advises the decoder to insert the following token n times into his output stream [44]. The technique of run length coding exploits the high interpixel redundancy that exists in relatively simple images [4]. In run length coding we look for gray levels that repeat along each row of the image. A 'run' of consecutive pixels whose gray level is identical is replaced with two values the length of the

run and the gray level of all the pixels in the run. Hence, the sequence (50, 50, 50, and 50) becomes (4, 50). Run length coding can be applied on a row-by-row basis, or we can consider the image to be a one-dimensional data stream in which the last pixel in a row is adjacent to the first pixel in the next row. This can lead to slightly higher compression ratio if the left and right–hand sides of the image are similar.

For the special case of binary images, we don't need to record the value of a run, unless it is the first run of the row. This is because there are only two possible values for a pixel in binary image. If the first run has one of the values, the second run implicitly has the other value; the third run implicitly has the same value as the first, and so on. Note that, if the run is of length 1, run length coding replaces one value with a pair of values. It is therefore possible for run length coding to increase the size of the dataset in images where run of length 1 are numerous. This might be the case in noisy or highly textured images. For this reason, it is most useful for the compression of binary images or very simple grayscale images. One advantage of this method is that it is sequential; once a particular series has been counted it could be transmitted.

Consequently the principles of this method are employed by the consultative committee for international telephony and telegraphy (CCITT) codec for fax communication in conjunction with the Huffman code. Run length coding is easily implemented, either in software or in hardware. It is fast and very well verifiable, but its compression ability is very limited.

3.4.2 Arithmetic Coding

Arithmetic coding has a complete approach in the way of producing variable-length codes. It is a method of encoding data using a variable number of bits. The number of bits used to encode each symbol varies according to the probability assigned to that symbol. Low probability symbols use many bits; high probability symbols use fewer bits. So far, this makes Arithmetic Coding sound very similar to Huffman coding. However, there is an important difference.

An arithmetic encoder doesn't have to use an integral number of bits to encode a symbol. If the optimal number of bits for a symbol is 2.4, a Huffman coder will probably use 2 bits per symbol, whereas the arithmetic encoder uses very close to 2.4. This means an arithmetic coder can usually encode a message using fewer bits. Arithmetic coding generates non-block

codes. In arithmetic coding, a one-to-one correspondence between source symbols and code words does not exist. Instead an entire sequence of source symbols or message is assigned a single arithmetic code word. The code word itself defines an interval or real numbers between 0 and 1. As the number of symbols in the message increases, the interval used to represent it becomes smaller and the number of information units (say, bits) required to represent the interval becomes larger. Each symbol of the message reduces the size of the

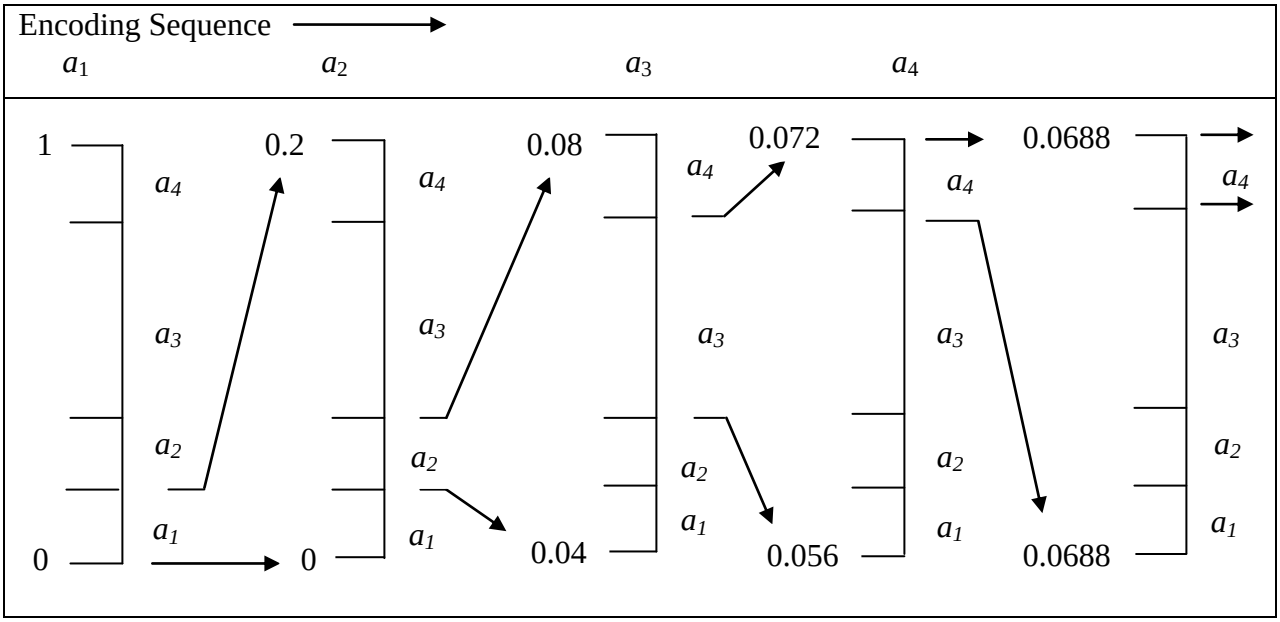

Figure 3.3: Arithmetic Coding Procedure

interval in accordance with its probability of occurrence.

It is especially useful when dealing with sources with small alphabet, such as binary sources, and alphabets with highly skewed probabilities. An arithmetic coder accepts at its input the symbols in a source sequence along with their corresponding probability estimates, and produces at its output a code stream with a length equal to the combined ideal code lengths of the input symbols. An important fact about arithmetic coding is that the amount of patents covering it influenced JPEG file format to use Huffman coding instead.

3.4.3 Huffman Coding

This algorithm, developed by D.A. Huffman, is based on the fact that in an input stream certain tokens occur more often than others. Huffman coding is a lossless method of image compression which is based on the frequency of occurrence of a data item (pixel in images).

The principle is to use a lower number of bits to encode the data that occurs more frequently. Codes are stored in a code book which may be constructed for each image or a set of images [39].

In all cases the code book plus encoded data must be transmitted to enable decoding. Huffman code procedure is based on the two observations [35].

1. More frequently occurred symbols will have shorter code words than symbol that occur less frequently.
2. The two symbols that occur least frequently will have the same length.

Table 3.1: Huffman Source Reductions

Original Source		**Source Reduction**			
Symbol	**Probability**	**1**	**2**	**3**	**4**
a_2	**0.4**	**0.4**	**0.4**	**0.4**	**0.6**
a_6	**0.3**	**0.3**	**0.3**	**0.3**	**0.4**
a_1	**0.1**	**0.1**	**0.2**	**0.3**	
a_4	**0.1**	**0.1**	**0.1**		
a_3	**0.06**	**0.1**			
a_5	**0.04**				

The Huffman code is designed by merging the lowest probable symbols and this process is repeated until only two probabilities of two compound symbols are left and thus a code tree is generated and Huffman codes are obtained from labeling of the code tree [30]. An example of how this is done is shown in table 5.1.

The source symbols and their probabilities are ordered from top to bottom in terms of decreasing probability values. To form the first source reductions, the bottom two probabilities, 0.06 and 0.04 are combined to form a "compound symbol" with probability 0.1. This compound symbol and its associated probability are placed in the first source reduction column so that the probabilities of the reduced source are also ordered from the most to the least probable. This process is than repeated until a reduced source with two symbols (at the far right) is reached. The second step if Huffman's procedure is to code each reduced source,

starting with the smallest source and working back to its original source. The minimal length binary code for a two-symbol source, of course, is the symbols 0 and 1.

As shown in table 5.2, these symbols are assigned to the two Symbols on the right (the assignment is arbitrary; reversing the order of the 0 and would work just and well). As the reduced source symbol with probabilities 0.6 was generated by 24 combining two symbols in the reduced source to its left, the 0 used to code it is now assigned to both of these symbols, and a 0 and 1 are arbitrary appended to each to distinguish them from each other. This operation is then repeated for each reduced source until the original course is reached.

The final code appears at the far-left in table 5.2. The average length of the code is given by the average of the product of probability of the symbol and number of bits used to encode it. This is calculated below:

L_{avg} = (0.4) (1) + (0.3)(2) + (0.1)(3) + (0.1)(4) + (0.06)(5) + (0.04)(5) = 2.2 bits/ symbol

and the Entropy of the source is

Entropy = 2.14 bits/symbol, and

Resulting Huffman code efficiency is

$$\eta_{hc}=2.14/2.2 = 0.973.$$

Table 3.2: Huffman Code Assignment Procedure

Original Source		**Source Reduction**				
Sym.	**Prob.**	**Code**	**1**	**2**	**3**	**4**
a_2	**0.4**	**1**	**0.4 1**	**0.4 1**	**0.4 1**	**0.6 0**
a_6	**0.3**	**00**	**0.3 00**	**0.3 00**	**0.3 00**	**0.4 1**
a_1	**0.1**	**011**	**0.1 011**	**0.2 010**	**0.3 01**	
a_4	**0.1**	**0100**	**0.1 0100**	**0.1 011**		
a_3	**0.06**	**01010**	**0.1 0101**			
a_5	**0.04**	**01011**				

Huffman's procedure creates the optimal code for a set of symbols and probabilities subject to the constraint that the symbols be coded one at a time. After the code has been created, coding and/or decoding is accomplished in a simple look-up table manner. The code itself is

an instantaneous uniquely decodable block code. It is called a block code, because each source symbol is mapped into a fixed sequence of code symbols.

3.5 LOSSY IMAGE COMPRESSION TECHNIQUES

Lossy compression schemes involve some loss of information, and data that have been compressed using lossy techniques generally cannot be recovered or reconstructed exactly. Often this is because the compression completely discards redundant information. However, lossy schemes are capable of achieving much higher compression. This is important for applications like TV signals, teleconferencing.

Here is tradeoff between compression and accuracy. Lossy methods deliver higher compression ratios, but sacrifice the ability reproduces the original, uncompressed pixel for pixel. JPEG is the best known lossy compression standard and widely used to compress still images stored on compact disc. It is considerably more complicated than RLE, but it produces correspondingly higher compression ratios even for images containing little or no redundancy. Except where every piece of information of a scan is critical, for example, scientific data – a scan must only provide enough information to meet the needs of the reproduction process and the viewer.

3.5.1 Lossy Predictive Coding

A lossy predictive coding has an additional quantizer that also executes rounding, compared to the lossless predictive coding while the decoder is the same as the lossless predictive coding.

The quantizer, that also executes rounding, is added between the calculation of the prediction error e_n and the symbol encoder. It maps e_n to a limited range of values $\overline{e_n}$ and determines both the amount of extra compression and the deviation of the error-free compression [35], [4]. This happens in a closed circuit with the predictor to restrict an increase in errors.

The predictor does not use e_n but rather $\overline{e_n}$, because both the encoder and decoder know it. Below figure 3.4 shows the lossy predictive coding model for encoder and decoder.

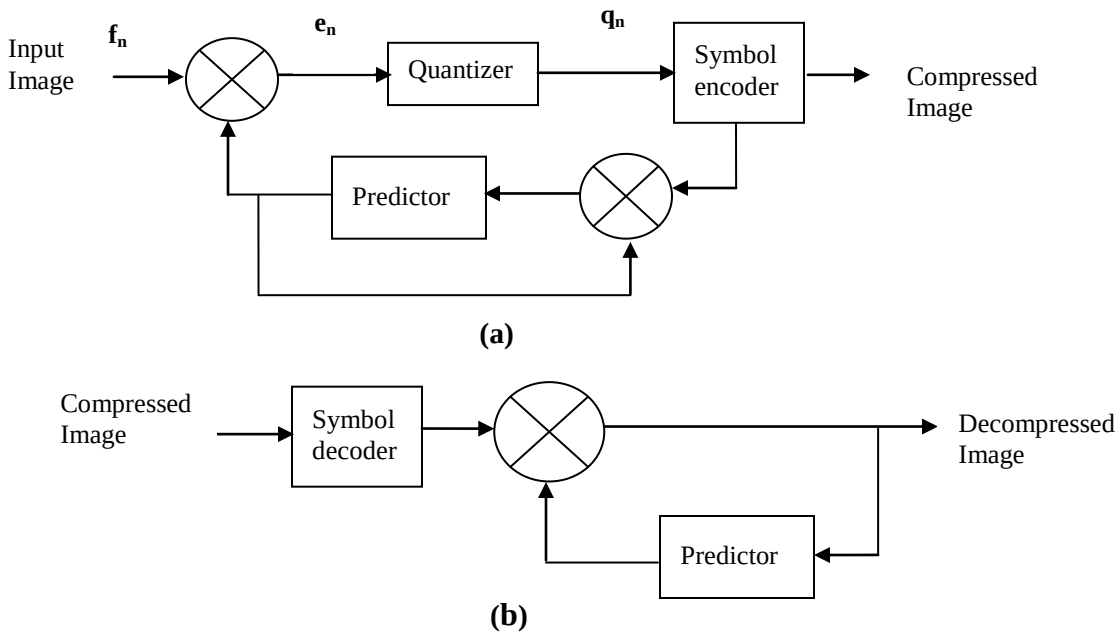

Figure 3.4 A lossy predictive coding model: (a) encoder; (b) decoder

3.5.2 Transform Coding

A general transform coding scheme involves subdividing an N×N image into smaller n×n blocks and performing a unitary transform on each sub-image. A unitary transform is a reversible linear transform whose kernel describes a set of complete, orthonormal discrete basic functions. Transform coding first transforms the image from its spatial domain representation to a different type of representation using some well-known transform and then codes the transformed values or coefficients.

The goal of the transformation process is to decorrelate the pixels of each sub image, or to pack as much information as possible into the smallest number of transforms coefficients [1]. This method provides greater data compression compared to predictive methods, although at the expense of greater computational requirements. The choice of particular transform in a given application depends on the amount of reconstruction error that can be tolerated and the computational resources available. By transforming an image from one space to another, we can not only separate different visual properties, but we can also change the predictive (and thus information containing) properties of the data. If we can transform it so that there is more coding or interpixel redundancy, we can compress the image better. For a transform coding scheme, logical modeling is done in two steps: a segmentation one, in which the

image is subdivided in bi-dimensional vectors which are possibly of different sizes and a transformation step, in which the chosen transform (e.g. FrFT) is applied.

As shown in figure 3.5 (a) encoder performs three relatively straightforward operations i.e. Sub image decomposition, Transformation and Quantization. The decoder implements the inverse sequence of steps with the exception of the quantization function of the encoder shown in figure 3.5 (b). An N × N input image is first subdivided into sub images of size n×n, which are then transformed to generated $(N/n)^2$, n×n sub image transform arrays. The quantization stage selectively eliminates or more coarsely quantize the co-efficient that carry the least information.

In transform coding system any kind of transformation can be chosen, such as Discrete Cosine transform, Walsh-Hadamard transform, Fourier transform etc.

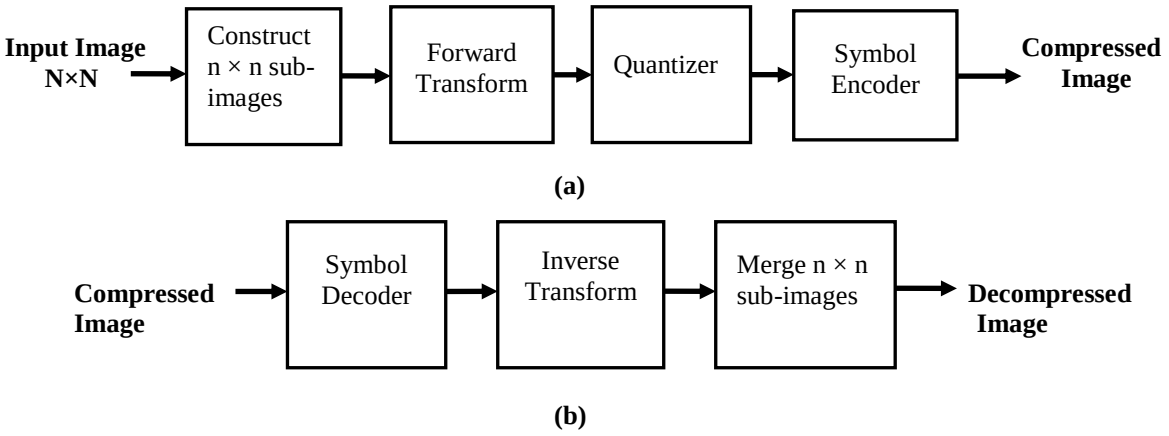

Figure 3.5 A transform coding system: (a) encoder; (b) decoder

The choice of a particular transformation in a given application depends on the amount of reconstruction error that can be tolerated and the computational resources available [19], [42]. To receive good result the transform should have the following properties:

- Fast to compute.
- Decorrelate transform coefficient to remove redundancies.
- Pack energy into only a few transform coefficients.
- Preserve energy.

3.6 IMAGE ENCRYPTION TECHNIQUES

Image security is based on cryptography. In fact, some basic concepts from cryptography are used as building blocks for applications in image security. Image encryption is necessary for future multimedia Internet applications. Password codes to identify individual users will likely be replaced are biometric images of fingerprints and retinal scans in the future. However, such information will likely be sent over a network. When such images are sent over a network, an eavesdropper may duplicate or reroute the information. By encrypting these images, a degree of security can be achieved. Furthermore, by encrypting noncritical images as well, an eavesdropper is less likely to be able to distinguish between important and non-important information [53]. Image encryption can also be used to protect privacy. An example for image encryption to protect privacy is in medical imaging applications. Recently, in order to reduce the cost and to improve service, electronic forms of medical records have been sent over networks from laboratories to medical centers. According to the law, medical records, which include many images, should not be disclosed to any unauthorized persons. Medical images, therefore, should be encrypted before they are sent over networks [36]. Unlike the conventional cryptographic algorithms, which are mainly based on discrete mathematics, chaos-based cryptography is relied on the complex dynamics of nonlinear systems or maps, which are deterministic but simple. Chaotic maps present many desired cryptographic qualities such as simplicity of implementation that leads to high encryption rates, and excellent security. Therefore, it can provide a fast and secure means for data protection, which is crucial for image data transmission over fast communication channels, such as the broadband Internet communication.

3.6.1 Goal of Encryption

Encryption is a technique that is used to accomplish the following four goals:

Confidentiality: Confidentiality refers to the protection of information from unauthorized access. An undesired communicating party, called adversary must not be able to access the communication material. This goal of cryptography is a basic one that has been always addressed and enforced throughout the history of cryptographic practice.

Data integrity: It ensures that information has not been manipulated in an unauthorized way. If the information is altered, all communicating parties can detect this alteration.

Authentication: Authentication methods are studied in two groups; entity authentication and message authentication. Entity authentication is the process whereby one party is assured of the identity of a second party involved in a protocol, and that the second has actually participated immediately prior to the time the evidence is acquired. Message authentication is a term used analogously with data origin authentication. It provides data origin authentication with respect to the original message source and data integrity, but no uniqueness and timeliness guarantees.

Non-repudiation: It means that the receiver can prove to everyone that the sender did indeed send the message; i.e., the sender cannot claim that he or she did not encrypt and/or sign certain digital information.

3.7 CLASSIFICATION OF ENCRYPTION ALGORITHMS

Encryption algorithms can be classified in different ways; according tostructures of the algorithms, according to keys, or according to the percentage of the data encrypted.

3.7.1 Classification According to Encryption Structure

Encryption algorithms can be classified according to encryption structure into block ciphers and stream ciphers.

A block cipher is a type of symmetric-key encryption algorithms that transforms a fixed-length block of plaintext data into a block of ciphertext data of the same length. The fixed length is called the block size. For many block ciphers, the block size is 64 or 128 bits. The larger the block size is, the more secure is the cipher, but the more complex are the encryption, decryption algorithms and devices. Modern block ciphers have the following features

(a) Variable key size.

(b) Mixed arithmetic operations, which can provide non-linearity.

(c) Data-dependent rotations and key-dependent rotations.

(d) Lengthy key schedule algorithm.

Block ciphers can be characterized by:

(a) Block size. Larger block sizes mean greater security.

(b) Key size. Larger key sizes mean greater security.

(c) Number of rounds. Multiple rounds increase security.

Unlike block ciphers that operate on large blocks of data, stream ciphers typically operate on smaller units of plaintext, usually bits. So, stream ciphers can be designed to be exceptionally fast, much faster than a typical block cipher. Usually, the bitwise XOR operation is chosen to perform ciphering. Stream ciphers have the following properties:

(a) They don't have perfect security.

(b) Security depends on the properties of the PRNG.

(d) Typical stream ciphers are very fast.

3.7.2 Classification According to Keys

According to keys, there are two kinds of ciphers following the relationship of *Ke* and *Kd*. Where K_e and K_d, the cipher is called a private-key cipher or a symmetric cipher. For private-key ciphers, the encryption/decryption key must be transmitted from the sender to the receiver via a separate secret channel. When K_e and K_d the cipher is called a public-key cipher or an asymmetric cipher. For public-key ciphers, the encryption key K_e is published and the decryption key K_d is kept private, for which no additional secret channel is needed for key transfer. In conventional encryption, the sender encrypts the data (plaintext) using the encryption key and the receiver decrypts the encrypted data (ciphertext) into the original data (plaintext) using the decryption key. In symmetric encryption, both encryption and decryption keys are identical. Instead of one key, there are two different keys; a public (K_e) and a private (K_d). Public key cryptography solves the problem of conventional cryptosystems by distributing the key [60-61]. Table 3.1 shows a comparison between symmetric encryption and asymmetric encryption.

Table 3.3 Comparison between symmetric encryption and asymmetric encryption

Symmetric Encryption	Asymmetric Encryption
Requirements to work:	Requirements to work:
(i) The same algorithm with the same key can be used for encryption and decryption. (ii) The sender and receiver must share the algorithm and the key.	(i) One algorithm is used for encryption and decryption with a pair of keys, one for encryption and one for decryption. (ii) The sender and receiver must each have one of the matched pair of keys.
Requirements for security:	Requirements for security:
(i) The key must be kept secret. (ii) It must be impossible or at least impractical to decipher a message if no other information is available. (iii) Knowledge of the algorithm plus samples of the ciphertext must be insufficient to determine the key.	(i) The decryption key must be kept secret. (ii) It must be impossible or at least impractical to decipher a message if no other information is available. (iii) Knowledge of the algorithm, the encryption key and samples of the ciphertext must be insufficient to determine the decryption key.

In general, there are two types of encryption systems:

(a) Symmetric (private) key encryption systems.

(b) Asymmetric (public) key encryption systems.

Most people have chosen to call the first group simply symmetric key encryption systems, and the popular name for the second group is just public key encryption systems.

3.7.3 Classification According to Percentage of Encrypted Data

With respect to the amount of encrypted data, the encryption can be divided into full encryption and partial encryption (also called selective encryption), according to the percentage of the data encrypted.

In the satellite images encryption, the cascaded encryption techniques are used for encrypting the satellite images. The advantage of using these techniques is the security strength of encryption is greatly enhanced.

CHAPTER-4

FRACTIONAL TRANSFORMS

4.1 FRACTIONAL OPERATIONS

Going from the whole of an entity to fractions of it represents a relatively major conceptual leap. The fourth power of 3 may be defined as 3^4= 3x3x3x3, but it is not obvious from this definition how one might define $3^{3.5}$. It must have taken sometime before the common definition $3^{3.5} = 3^{7/2} = \sqrt{3^7}$ emerged. The first and second derivatives of the function $f(x)$ are commonly denoted by:

$\frac{df(x)}{dx}$ and $\frac{d^2 f(x)}{dx} = \frac{d}{dx}\left[\frac{df(x)}{dx}\right] = \frac{d[df(x)/dx]}{dx} = \left(\frac{d}{dx}\right)^2 f(x)$ respectively.

Higher order derivatives are defined similarly. Now let us generalize this property by replacing n with the real order '**a**' and take it as the a[th] derivative of $f(x)$. Thus to find $\frac{d^a f(x)}{dx^a}$, the a[th] derivative of $f(x)$, find the inverse Fourier transform of $(i2\pi\mu)^a F(\mu)$. In both of these examples we are dealing with the fractions of an operation performed on an entity, rather than fractions of the entity itself. $2^{0.5}$ is the square root of the integer 2. The function $[f(x)]^{0.5}$ is the square root of the function $f(x)$. But $\frac{d^{0.5} f(x)}{dx^{0.5}}$ is the 0.5^{th} derivative of $f(x)$ with $\left(\frac{df(x)}{dx}\right)^{0.5}$ being the square root of the derivative operator $\frac{d}{dx}$. The process of going from the whole of an entity to fractions of it underlies several of the more important conceptual developments e.g. fuzzy logic, where the binary 1 & 0 are replaced by continuous values representing our certainty or uncertainty of a proposition [46].

4.2 FRACTIONAL FOURIER TRANSFORM

The FrFT is a generalization of the ordinary Fourier transform with an order parameter 'a' and is identical to the ordinary Fourier transform when this order α is equal to π/2 [33]. Since the ordinary Fourier transform and related techniques are of importance in various different areas like communications, signal processing and control systems, it is natural to expect the FrFT to find many applications in these fields as well. The FrFT belongs to the class of time–

frequency representations that have been extensively used by the signal processing community. In all the time–frequency representations, one normally uses a plane with two orthogonal axes corresponding to time and frequency. If we consider a signal x(t) to be represented along the time axis and its ordinary Fourier transform X(f) to be represented along the frequency axis, then the Fourier transform operator (denoted by F) can be visualized as a change in representation of the signal corresponding to a counter clockwise rotation of the axis by an angle $\pi/2$ [59].

This is consistent with some of the observed properties of the Fourier transform (FT). For example, two successive rotations of the signal through $\pi/2$ will result in an inversion of the time axis. Moreover, four successive rotations will leave the signal unaltered since a rotation through 2π of the signal should leave the signal unaltered. The FrFT is a linear operator that corresponds to the rotation of the signal through an angle which is not a multiple of $\pi/2$, i.e. it is the representation of the signal along the axis u making an angle α with the time axis.

4.2.1 Historical Development of FrFT

The FRFT, which is a generalization of the ordinary Fourier transform (FT), was introduced 75 years ago, but only in the last two decade it has been actively applied in signal processing, optics and quantum mechanics. The FT is undoubtedly one of the most valuable and frequently used tools in signal processing and analysis. Little need be said of the importance and ubiquity of the ordinary Fourier transform in many areas of science and engineering. A generalization of Fourier Transform- the Fractional Fourier Transform was introduced in 1980 by Victor Namias [58] and it was established in the same year that the other transforms could also be fractionalized [59]. He was apparently unaware of the previous works of N. Wiener in 1929, H. Weyl in 1930, E. U. Condon in 1937, H. Kober in 1939, A. P. Guinand in 1956, A. L. Patterson in 1959, V. Bargmann in 1961, De Bruijn in 1973 and R. S. Khare in 1974, and of others. Though the idea was the same, these authors discussed the FRFT in a broader context and not by the same name Mustard [2] in 1987 did considerable work considering Condon and Bargmann as his base without citing Namias' work. McBride and Keer explored the refinement and mathematical definition in 1987 [2].

In a very short span of time, FRFT has established itself as a powerful tool for the analysis of time varying signals [17],[23]. Furthermore, a general definition of FRFT for all classes of signals (one-dimensional & multidimensional, continuous & discrete and periodic & non-

periodic) was given by Cariolario et al. in. But when FrFT is analyzed in discrete domain there are many definitions of Discrete Fractional Fourier Transform [11], [25]. It is also established that none of these definitions satisfies all the properties of continuous FRFT. Santhanam and McClellan first reported the work on DFrFT in 1995. Thereafter within a short span of time a lot many definitions of DFrFT came into existence and these 10 definitions are classified according to the methodology used for calculations in 2000 by Pie et al. The FrFT has been found to have several applications in the areas of optics and signal processing and it also lead to generalization of notion of space (or time) and frequency domains which are central concepts of signal processing.

4.2.2 Mathematical Definition of FrFT

The FRFT is a generalization of the ordinary Fourier transform with an order parameter a and is identical to the ordinary Fourier transform when this order α is equal to π/2. The FRFT belongs to the class of time–frequency representations that have been extensively used by the signal processing community.

In all the time–frequency representations; one normally uses a plane with two orthogonal axes corresponding to time and frequency. The FRFT is defined with the help of the transformation kernel K_α, as [33]

$$K_\alpha(t,u)=\begin{cases}\delta(t-u) & \text{if } \alpha \text{ is a multiple of } 2\pi \\ \delta(t+u) & \text{if } \alpha+\pi \text{ is a multiple of } 2\pi \\ \sqrt{\dfrac{1-j\cot\alpha}{2\pi}}\,e^{j\left(\left(u^2+t^2\right)/2\right)\cot\alpha-jut\operatorname{cosec}(\alpha)} & \text{if } \alpha \text{ is not a multiple of } \pi\end{cases}. \tag{4.1}$$

Another useful form of writing the square root factor preceding the transformation kernel K_α, can be obtained using the relation

$$\sqrt{\frac{1-j\cot\alpha}{2\pi}}=\sqrt{\frac{-je^{j\alpha}}{2\pi\sin\alpha}} \tag{4.2}$$

The FRFT is defined using this kernel as (FRFT of order α of x (t) denoted by $X_\alpha(u)$)

$$X_\alpha(u) = \int_{-\infty}^{\infty} x(t) K_\alpha(t,u)\, dt, \tag{4.3}$$

Where

$$X_\alpha(u) = \begin{cases} \sqrt{\dfrac{1-j\cot\alpha}{2\pi}}\, e^{j\left(u^2\cot\alpha/2\right)} \displaystyle\int_{-\infty}^{\infty} x(t) e^{j\left(t^2\cot\alpha/2\right) - jut\,\mathrm{cosec}(\alpha)}\, dt, & \text{if } \alpha \text{ is not a multiple of } \pi \\ X(t) & \text{if } \alpha \text{ is a multiple of } 2\pi \\ X(-t) & \text{if } \alpha+\pi \text{ is a multiple of } 2\pi \end{cases}. \tag{4.4}$$

Where $\alpha = a\dfrac{\pi}{2}$

Let F_α the operator corresponding to the FRFT of angle α. Under this notation, when $\alpha = a\dfrac{\pi}{2}$. Some of the important properties of the FRFT operator are listed below:

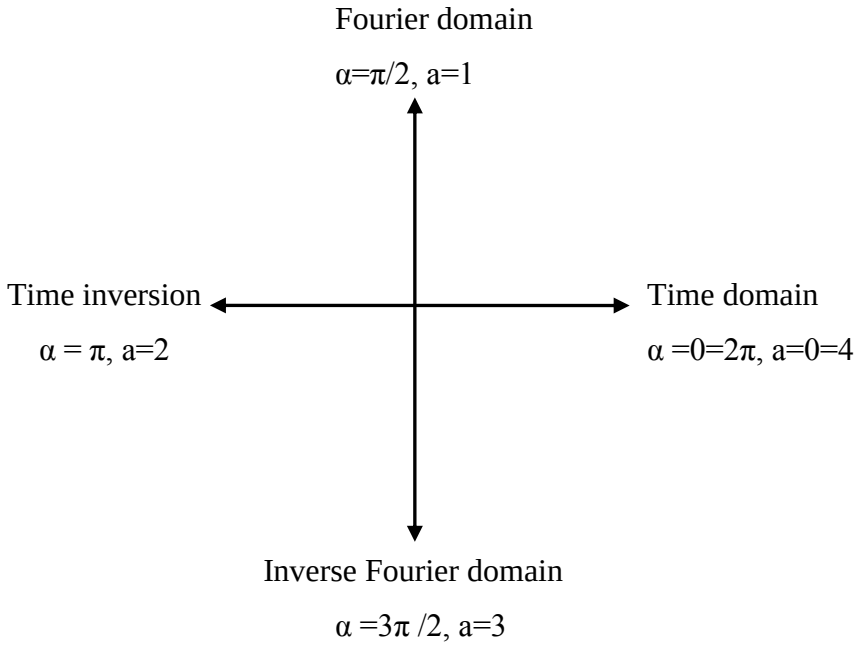

Fig. 4.1: FRFT domain in time-frequency plane

The Fig 4.1 shows the FRFT domain in t-f plain. The FRFT of a signal x(t) as given by Eq. (4.4) can be computed by four steps process [33]:

1. Multiplying the function with a chirp,
2. Taking its Fourier transform,
3. Again multiplying with a chirp, and
4. Then multiplication with an amplitude factor.

It is found that the FRFT of a signal $x(t)$ exists under the same conditions in which its Fourier transform exists. In order to discuss the various properties of the FRFT, it would be ideal to denote the FRFT in an operator notation.

4.2.3 Properties of fractional Fourier transform

Properties of fractional Fourier transform are given in table1 as below:

Table 4.1 Properties of fractional Fourier transform

Sr. No.	**Operation**	**Signal, $x(t)$**	**Fractional Fourier Transform, $X_\alpha(u)$**
1	Time shift	$x(t-\tau)$	$e^{j(\tau^2/2)\sin\alpha\cos\alpha - ju\tau\sin\alpha} X_\alpha(u-\tau\cos\alpha)$
2	Modulation	$x(t)\, e^{jvt}$	$e^{-jv^2(\sin\alpha\cos\alpha)/2 + juv\cos\alpha} X_\alpha(u-v\sin\alpha)$
3	Inversion of time axis	$x(-t)$	$X_\alpha(-u)$
4	Scaling of time axis	$x(ct)$	$\sqrt{\frac{1-j\cot\alpha}{c^2-j\cot\alpha}}\, e^{j(u^2/2)\cot\alpha\left(1-\left(\cos^2\beta/\cos^2\alpha\right)\right)}$
5	Differentiation	$x'(t)$	$X'_\alpha(u)\cos\alpha + ju\sin\alpha X_\alpha(u)$
6	Integration	$\int_a^t x(t')dt'$	$\sec\alpha e^{-j(u^2/2)\tan\alpha}\int_a^u X_\alpha(z) e^{j(z^2/2)\tan\alpha} dz$ if $\alpha - \pi/2$ is not a multiple of π
7	Multiplication with ramp	$tx(t)$	$u\cos\alpha X_\alpha(u) + j\sin\alpha X'_\alpha(u)$
8	Convolution	$x(t) * g(t)$	$F^{-a}\left[\left(F^a x\right)\left(F^a g\right)\right]$

4.3 FRACTIONAL COSINE TRANSFORM

Fractional cosine has been derived by authors [55]. The fractional cosine transforms are derived by taking the real part of FrFT kernel. The real part is chosen as the kernels for FrCT as in case of cosine transform (CT). The FrCT can be derived from FrFT as given as

$$F_C^a[f(x)] = \int_{\infty}^{-\infty} Re[K^a(x,X)]\, f(x)dx$$

The cosine (CT) which is based on half-range expansions of a function over cosine basis functions, respectively, are also important tools in signal processing. Despite of some lack of elegance in their properties compared to the FT, the CT has its own areas of applications. The idea of fractionalization of the CT was proposed in [6]. There the real and imaginary parts of the fractional FT kernel were chosen as the kernels for a fractional CT and a fractional ST, respectively.

The fractional Cosine transform have advantages that transform results are real for real input but they do not demonstrate the additivity property and inverse transform.

4.4 DISCRETE FRACTIONAL FOURIER TRANSFORM

With the advent of computers and enhanced computational capabilities the Discrete Fourier Transform (DFT) came into existence in evaluation of FT for real time processing. Further these capabilities are enhanced by the introduction of DSP processors and Fast Fourier Transform (FFT) algorithms. On similar lines, so there arises a need for discretization of FrFT. Furthermore, DFT is having only one basic definition and nearly 200 algorithms are available for fast computation of DFT. But when FrFT is analyzed in discrete domain there are many definitions of Discrete Fractional Fourier Transform (DFrFT) [2], [11], [25]. It is also established that none of these definitions satisfies all the properties of continuous FRFT. Santhanam and McClellan first reported the work on DFrFT in 1995. Thereafter within a short span of time a lot many definitions of DFrFT came into existence and these definitions are classified according to the methodology used for calculations in 2000 by Pie et al.

4.4.1 Mathematical definition of DFrFT

The computation of DFrFT is based upon the eigen-decomposition of the DFT kernel matrix

[48].The kernel matrix of DFT has only four distinct eigenvalues [l, **-** *j***,** -1, *j*] shown in [10], [29].

The eigenvectors construct a vector space same eigenvalue because these eigenvectors of DFT kernel are not uniquely determined. A matrix **S** to evaluate the eigenvectors of **F** with real values [29]. The matrix **S** is defined as follows:

$$\mathbf{S} = \begin{bmatrix} \mathbf{2} & \mathbf{1} & \mathbf{0} & \mathbf{0} & \dots & \mathbf{1} \\ \mathbf{1} & \mathbf{2}\boldsymbol{cos\omega} & \mathbf{1} & \mathbf{0} & \dots & \mathbf{0} \\ \mathbf{0} & \mathbf{1} & \mathbf{2}\boldsymbol{cos2\omega} & \mathbf{1} & \dots & \mathbf{0} \\ \vdots & \vdots & \vdots & \ddots & & \\ \mathbf{1} & \mathbf{0} & \mathbf{0} & \mathbf{0} & \dots & \mathbf{2cos}(\boldsymbol{N-1})\boldsymbol{\omega} \end{bmatrix}$$

where $\boldsymbol{\omega} = \frac{2\pi}{N}$. It satisfies the following commutative property.

$$\mathbf{SF = FS} \tag{4.5}$$

The eigenvectors of **S** matrix are same as that of the eigenvectors of **F** having different corresponding eigenvalues. Due to symmetric property of S matrix, all eigenvalues of S matrix are real and the eigenvectors are orthonormal each other. The eigen-decomposition of matrix **S** is written as:

$$\mathbf{S} = \sum_{k=0}^{N-1} \gamma_k \boldsymbol{v_k} \tag{4.6}$$

where $\boldsymbol{v_k}$ is the eigenvector of the matrix **S** corresponding to the eigenvalue γ_k. The eigen-decomposition of DFT kernel matrix **F** is written as:

$$\mathbf{F} = \sum_{k\in E1} \boldsymbol{v_k v_k^*} + \sum_{k\in E2} (-j)\boldsymbol{v_k v_k^*} + \sum_{k\in E3} (-1)\boldsymbol{v_k v_k^*} + \sum_{k\in E4} (j)\boldsymbol{v_k v_k^*} \tag{4.7}$$

where *E1,E2,E3* and *E4* is the set of indices for eigenvectors belongs to eigenvalues [l, **-** *j***,** -1, *j*] respectively. From equation (4.7) the eigenvalues of DFT kernel is determined. By taking fractional powers of these eigenvalues, the transform kernel of DFrFT can be easily defined as

$$\boldsymbol{R^{\alpha}} = \boldsymbol{F^{\frac{2\alpha}{\pi}}}$$

$$= \begin{cases} \sum_{k=0}^{N-1} e^{-jN\alpha} \boldsymbol{v_k v_k^*} & \text{N is odd} \\ \sum_{k=0}^{N-2} e^{-jN\alpha} \boldsymbol{v_k v_k^*} + e^{-jN\alpha} \boldsymbol{v_{N-1} v_{N-1}^*} & \text{N is even} \end{cases}$$

where $\boldsymbol{v_k}$ is the eigenvector obtained from matrix **S**. The DFrFT of signal *x(n)* can be computed through equation

$$X_\alpha(n) = R_\alpha x(n) = F^{\frac{2\alpha}{\pi}} x(n) = VD^{\frac{2\alpha}{\pi}} V^* x(n) \tag{4.8}$$

The signal *x(n)* can also be recovered from its DFrFT through an operation with parameter *(-α)* as

$$x(n) = R_{-\alpha} X_\alpha(n) = VD^{\frac{-2\alpha}{\pi}} V^* X_\alpha(n) \tag{4.9}$$

4.4.2 Properties of DFrFT

Properties of discrete fractional Fourier transform kernels are below

Table 4.2 properties of DFrFT kernels

1.	Unitary	$\boldsymbol{R_\alpha^* = R_\alpha^{-1} = R_{-\alpha}}$
2.	Angle Additivity	$\boldsymbol{R_\alpha R_\beta = R_{\alpha+\beta}}$
3.	Time inversion	$\boldsymbol{R_\alpha} x(-n) = X_\alpha(-n)$
4.	Periodicity	$\boldsymbol{R_{\alpha+2\pi} = R_\alpha}$
5.	Symmetric	$\boldsymbol{R_\alpha}(a,b) = \boldsymbol{R_\beta}(b,a)$

4.5 DISCRETE FRACTIONAL COSINE TRANSFORM

Discrete fractional cosine transform is extended by discrete fractional fourier transform. DFrCT is a general form of discrete cosine transform (DCT) [51]. The DFrCT share many useful properties of the regular DCT, and it has a free parameter, its fraction. When the fraction is zero, we get the cosine modulated version of the input signal. When it is unity, we get the conventional DCT. The DCT-I eigenvectors can be attained from the DFT eigenvectors.

If $[\eta 0, \eta 1, \ldots \eta N\text{-}2, \eta N\text{-}1, \ldots \eta 1]^T$ is an even eigenvector of the (2*N* -2) point DFT kernel matrix F_{2N-2} $\eta=\lambda\eta$ (λ=1,-1). Then $\eta = [\eta 0, \sqrt{2}\,\eta 1 \ldots \sqrt{2}\,\eta N\text{-}2, \eta N\text{-}1]$ will be an eigenvector of the N point DCT-I kernel matrix, where λ is the corresponding eigenvalue. The eigenvalues of DCT-I kernel matrices are only 1 and –1.

Similar to DFrFT, the *N* point DFrCT kernel can be determined as $\mathbf{C}^\alpha = \mathbf{H}.\mathbf{D}^{2\alpha/\pi}.\mathbf{H}^T$

Where **H** is the matrix whose columns consists of the discrete hermite Gaussian vectors, **H**=

$[|\mathbf{H}_0|\mathbf{H}_1|.....|\mathbf{H}_{N-1}|]$ and $\mathbf{D}^{2\alpha/\pi}$ is the diagonal matrix of eigenvalues and α indicates the rotation angle of transform in time-frequency plane.

The steps for constructing the *N* point DFrCT kernel with angular parameter α are summarized [52] as follow:

Step 1: Compute the M_c point DFT hermite even eigenvectors. Where $M_c = 2(N - 1)$

Step 2: Use Step 1 to compute the DCT-I eigenvectors from the DFT hermite even eigenvectors.

Step 3: Find the DFrCT transform kernel by the following equation. $\mathbf{C}^{\alpha} = \mathbf{H}.\mathbf{D}^{2\alpha/\pi}.\mathbf{H}^{T}$

The above definitions of DFrFT/DFrCT are applicable for one dimensional signals such as speech waveform. For analysis of two-dimensional (2D) signals such as images, we need a 2D version of the DFrFT/DFrCT. For an M×N matrix, the 2D DFrFT/DFrCT is computed in a simple way: The 1D DFrFT/DFrCT is applied to each row of matrix and then to each column of the resultant matrix. The 2D transformation kernel is defined with separable form as [49]:

$$\boldsymbol{R}_{(\boldsymbol{\alpha},\boldsymbol{\beta})} = \boldsymbol{R}_{\boldsymbol{\alpha}} \otimes \boldsymbol{R}_{\boldsymbol{\beta}}$$

The 2D forward and inverse DFrFT are computed from above 2D transformation kernel as:

$$X_{(\alpha,\beta)}(m,n) = \sum_{p=0}^{M-1} \sum_{q=0}^{N-1} x(p,q) \;\; R_{(\alpha,\beta)}(p,q,m,n)$$

$$x(p,q) = \sum_{m=0}^{M-1} \sum_{n=0}^{N-1} X_{(\alpha,\beta)}(m,n) \;\; R_{(-\alpha,-\beta)}(p,q,m,n)$$

In two-dimensional DFrFT we have to consider two angles of rotation $\alpha=a\pi/2$ and $\beta=b\pi/2$ and If one of these angles is zero, the 2D transformation kernel reduces to the 1D transformation kernel.

CHAPTER-5

SATELLITE IMAGE COMPRESION USING DISCRETE FRACTIONAL TRANSFORMS

In image processing, an important part is the compression. This means the reducing the dimensions of the images, to a level that can be easily used or processed. Satellite Image compression using transform coding yields extremely good compression, with controllable degradation of image quality. In the present implementation DFrFT and DFrCT, generalization of DFT and DCT has been chosen. One of the reasons for this is that, these transforms provides additional degree of freedom to the problem as parameter 'a' gives multidirectional application. With the extra degree of freedom provided by these transforms, its fractional order 'a', high visual quality decompressed image can be achieved for same amount of compression.

5.1 FRACTIONAL TRANSFORM BASED COMPRESSION MODEL

In Satellite image compression using DFrFT and DFrCT, a compression model encoder performs three relatively straightforward operations i.e. Subimage decomposition, Transformation and Quantization. The decoder implements the inverse sequence of steps of encoder. Because quantization results in irreversible information loss, so inverse quantizer block is not included in the decoder as shown in figure 5.1 (b).

5.1.1 Subimage decomposition

An image is first partitioned into non-overlapped n×n subimages as shown in figure 5.1(a). The most popular subimage sizes are 8×8, 16×16. In present implementation subimage size chosen is 8×8. As subimage size increases, error decreases but computational complexity increases. Compression techniques that operate on block of pixels i.e. subimages are often

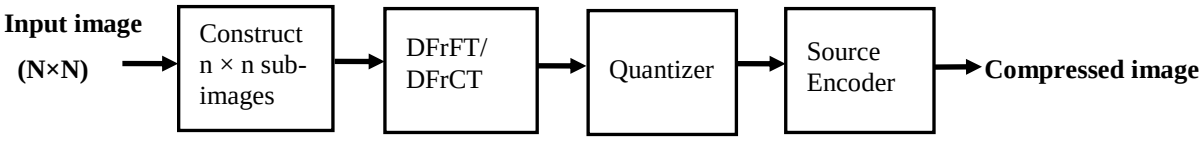

(a)

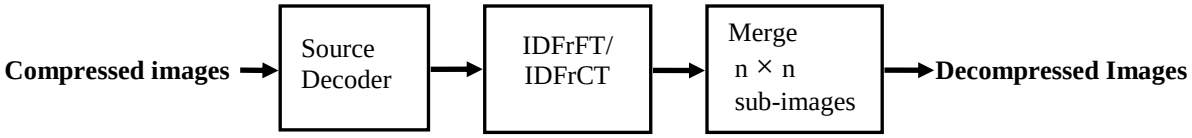

(b)

Figure 5.1 Compression model: (a) encoder; (b) decoder

described as block coding techniques. The transform of a block of pixels may suffer from discontinuity effects resulting in the presence of blocking artifacts in the image after it has been decompressed.

5.1.2 Transformation

In this step, a 2D-DFrFT/DrCT is applied to each block to convert the gray levels of pixels in the spatial domain into coefficients in the frequency domain as shown in figure 5.1(a). By using these transforms large amount of information is pack into smallest no. of transform coefficients, hence small amount of compression is achieved at this step. At decoder inverse DFrFT and DFrCT is applied and by changing the value of parameter 'a' to '-a' we get inverse DFrFT and DFrCT respectively.

5.1.3 Quantization

The final step in compression process is quantized the transformed coefficients according to cutoff selected and variation of 'a'. By adjusting the cutoff of the transform coefficients, a compromise can be made between image quality and compression factor. With these fractional transforms by varying its free parameter 'a', high compression ratio can achieve even for same cutoff. The quantized coefficients are then rearranged in a zig-zag scan order to form compressed image which can be stored or transmitted.

At decoder simply inverse process of encoder is performed by using inverse 2D-DFrFT and 2D-DFrCT. The non-overlapped subimages merged to get decompressed image. Since this techniques comes in the category of lossy compression techniques, the dequantizer is not present here. As we know it is lossy compression technique so there is some error between decompressed image and original image which can be evaluate.

5.2 PARAMETERS USED IN SATELLITE IMAGE COMPRESSION

The quality of compressed image can be measured by many parameters. The most commonly used parameters are Mean square Error and Peak Signal to Noise Ratio. The PSNR can be defined as the difference between the decoded image and its original image. The larger the PSNR value, the better will be the decoded image quality. The average of the square of the difference between the desired response and the actual system output (the error) or the mean square error is a measure of the differences between values predicted and the values actually observed. In lossless compression, the reconstructed image after compression is numerically identical to the original image but in the case of lossy compression, the reconstructed image is only an approximation to the original. MSE and PSNR are defined as:

$$MSE = \frac{1}{MN}\sum_{i=0}^{M-1}\sum_{j=0}^{N-1}[\overline{f}(i,j) - f(i,j)]^2$$

$$PSNR = 10\log_{10}\left[\frac{M \times N}{MSE}\right]$$

Where M×N the size of the images is, $\overline{f}(i,j)$ is the matrix elements of the decompressed and $f(i,j)$ is the matrix elements of the original images at (i,j) pixel.

In order to evaluate the performance of image compression systems, compression ratio metric is often employed. In our results, compression ratio is computed as the ratio of non-zero entries in the original image to the non-zero entries in the resultant hybrid image [44].

$$CR = \frac{Original\ image\ size\ in\ bytes}{Compressed\ image\ size\ in\ bytes}$$

$$CR\% = \left(1 - \left(\frac{1}{CR}\right)\right) \times 100$$

5.3 RESULTS AND SIMULATIONS USING DFrFT

The simulation result of the of four different satellite images using DFrFT at different CR at 10%, 20%, 30%, 40%, 50% and 70% are given below.

5.3.1 Result of satellite image 1 of 512×512 size

Image 1 is satellite image of 512×512 pixel size. Figure 5.2 shows the variation of PSNR with fractional order atdifferent CR. Figure 5.3 shows the variation of MSE with fractional order at different CR.

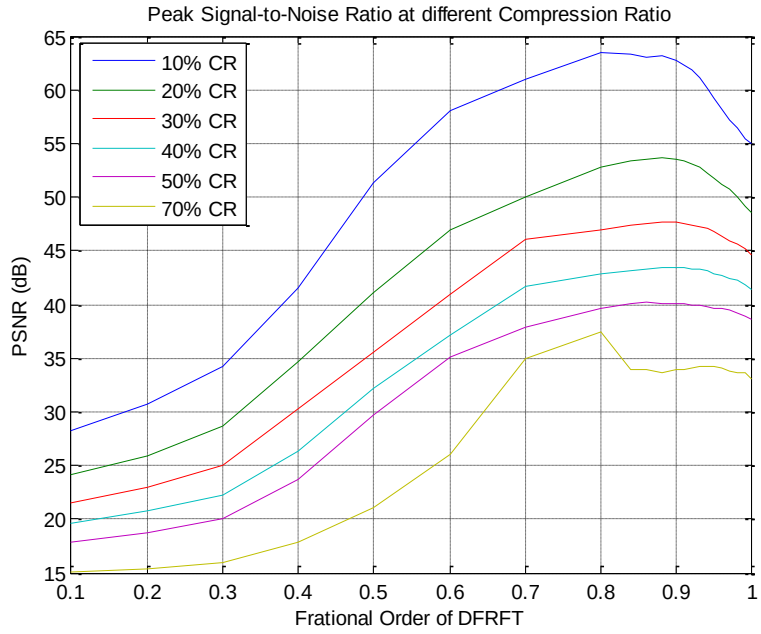

Figure 5.2 PSNR versus fractional order at different CR of image 1

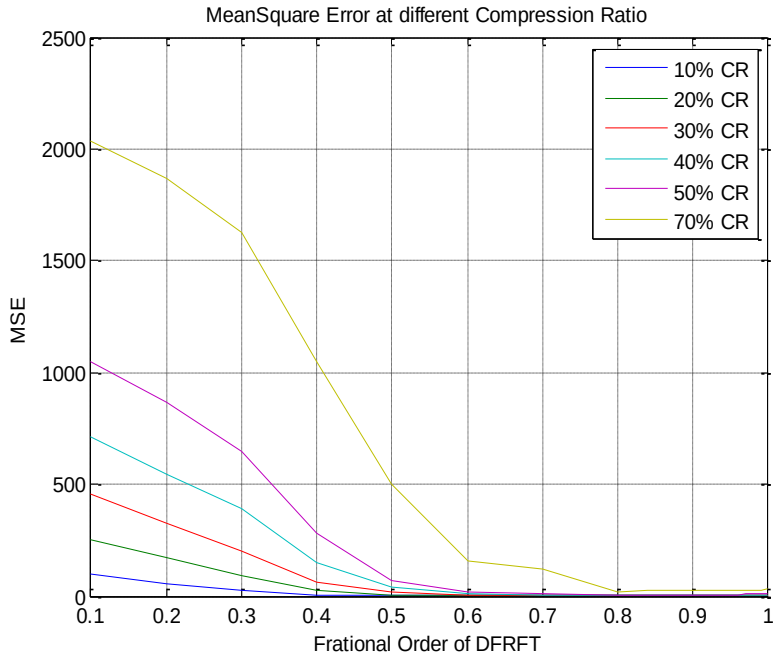

Figure 5.3 MSE versus fractional order at different CR of image 1

At 30% of Compression Ratio

The results of satellite image using DFrFT are shown below. Figure 5.4 shows four images. Figure 5.4 (a) is the original image, figure 5.4 (b), (c) and (d) are decompressed image at different fractional order 0.5, 0.9 and 1 respectively.

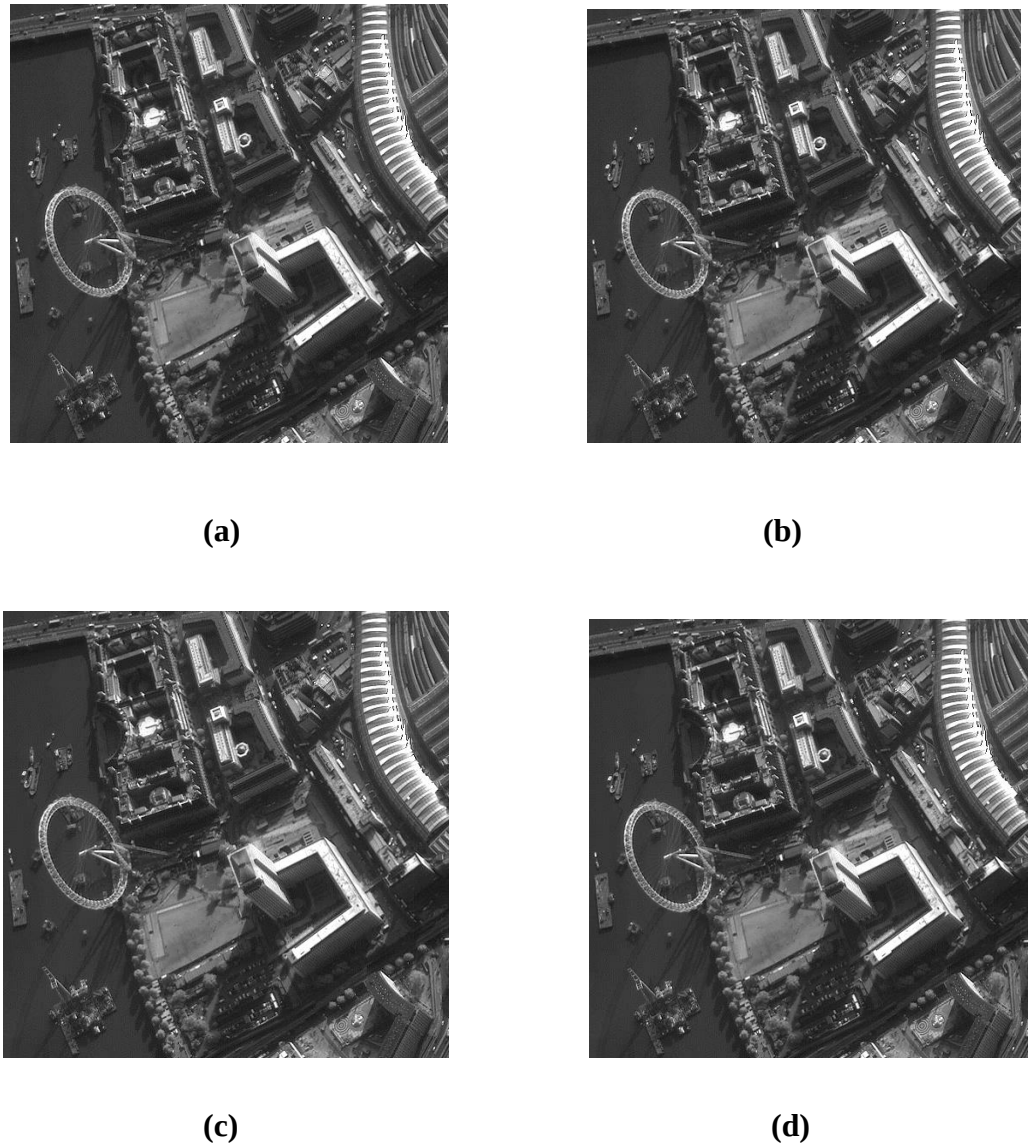

(a) **(b)**

(c) **(d)**

Figure 5.4 Satellite Image 1 at different value of fractional order (a) original images, (b) decompressed image at '0.5' fractional order , (c) decompressed image at optimum fractional order '0.9' and (d) decompressed image at fractional order '1'

At 50% of Compression Ratio

At 50 % CR, the original satellite image shown in figure 5.5 (a), figure 5.5(c) is decompressed satellite image at optimum value of fractional order in which the best results are obtained and figure 5.5 (d) is decompressed satellite image at fractional order 1.

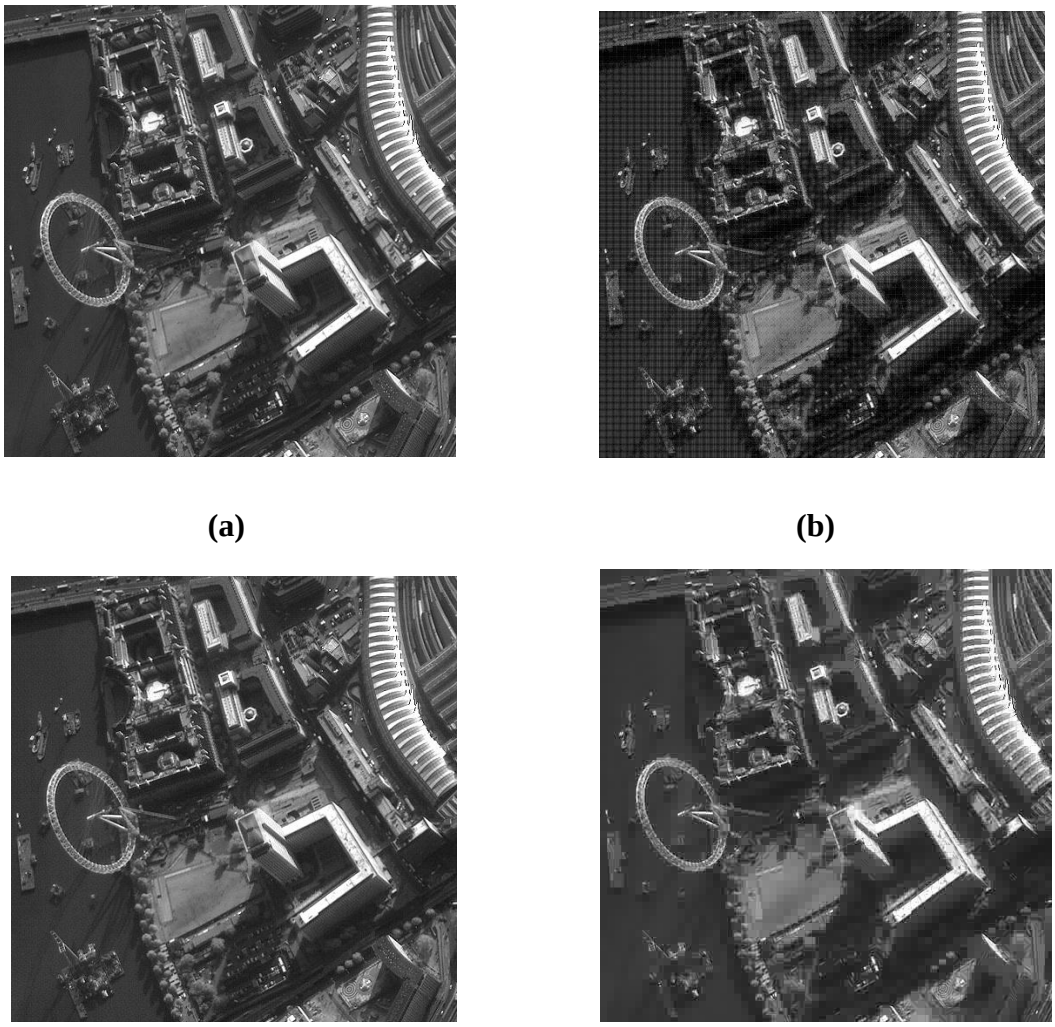

(a) **(b)**

(c) **(d)**

Figure 5.5 Satellite Image 1 at different value of fractional order (a) original images, (b) decompressed image at '0.5' fractional order , (c) decompressed image at optimum fractional order '0.86' and (d) decompressed image at fractional order '1'

At 70% of Compression Ratio

Using DFrFT, the results are shown in figure 5.6 at 70% CR. At optimum value of fractional order, the satellite image shown in figure 5.6 (c). Figure 5.6 (d) shows decompressed satellite image at fractional order 1.

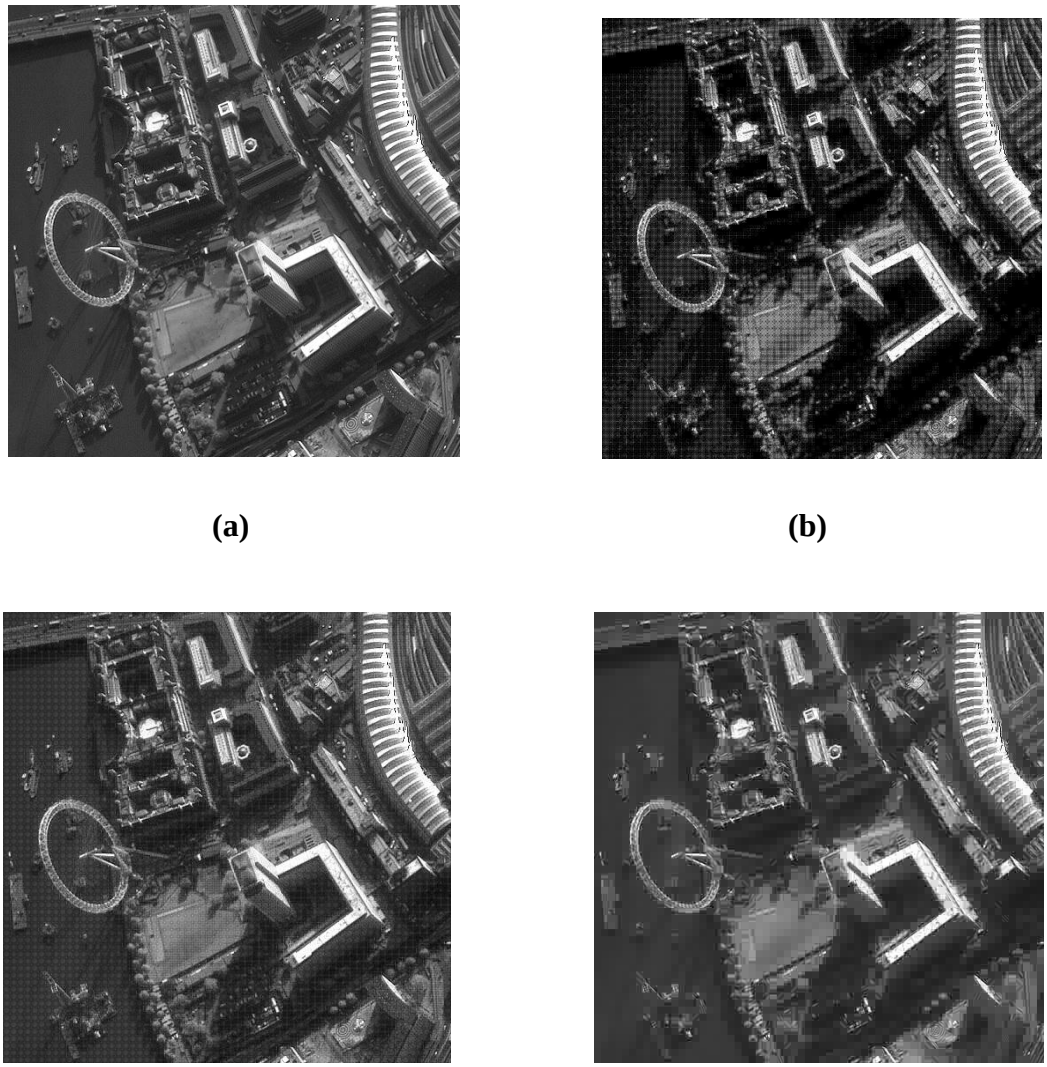

(a) **(b)**

(c) **(d)**

Figure 5.6 Satellite Image 1 at different value of fractional order (a) original images, (b) decompressed image at '0.5' fractional order , (c) decompressed image at optimum fractional order '0.74' and (d) decompressed image at fractional order '1'

By using DFrFT, it is clear that for same CR, it gives better-decompressed image as compared to FT. Figure 5.4(c), 5.5(c) and 5.6 (c) shows decompressed images at optimum fractional order a=0.9, 0.86 and 0.74 in which best result are achieved for 30 %, 50% and 70% CR respectively. The corresponding MSE and PSNR are listed in table 5.9.

Table 5.1 Result of satellite image compression using DFrFT of Image 1 at different CR%

Fractional Order(a)	PSNR 10%	MSE 10%	PSNR 20%	MSE 20%	PSNR 30%	MSE 30%	PSNR 40%	MSE 40%	PSNR 50%	MSE 50%
0.1	28.2675	96.901	24.14	250.51	21.54	455.35	19.611	711.16	17.92	1048.7
0.2	30.6433	56.072	25.82	169.87	22.97	327.79	20.77	544.43	18.77	863.038
0.3	34.25	24.419	28.7	90.8	25.05	202.9	22.24	387.99	20.045	643.44
0.4	41.603	4.4497	34.63	22.36	30.24	61.49	26.40	148.74	23.63	281.26
0.5	51.39	0.472	41.039	5.12	35.49	18.33	32.17	39.93	29.723	69.29
0.6	58.11	0.1004	46.99	1.3	40.92	5.26	37.17	12.45	35.04	20.34
0.7	60.91	0.0526	50.05	0.6419	46.003	1.632	41.72	4.374	37.92	10.47
0.8	63.42	0.0295	52.76	0.3442	47.014	1.2932	42.89	3.3405	39.62	7.090
0.84	63.34	0.0301	53.45	0.2937	47.36	1.194	43.15	3.143	40.04	6.4313
0.86	63.06	0.0321	53.59	0.2844	47.54	1.145	43.35	3.002	40.15	6.27
0.88	63.13	0.0316	53.66	0.2796	47.70	1.102	43.47	2.922	40.11	6.339
0.9	62.737	0.0346	53.48	0.2915	47.71	1.1012	43.46	2.93	40.05	6.416
0.91	62.31	0.0381	53.36	0.2995	47.58	1.1345	43.44	2.943	40.03	6.456
0.92	61.84	0.0425	53.09	0.3189	47.45	1.167	43.35	3.001	39.97	6.53
0.93	61.071	0.0508	52.741	0.3458	47.26	1.2198	43.26	3.063	39.913	6.63
0.94	60.1046	0.0635	52.26	0.3864	47.07	1.27	43.11	3.174	39.81	6.78
0.95	59.26	0.077	51.78	0.4323	46.75	1.37	42.88	3.34	39.70	6.95
0.96	58.27	0.0967	51.25	0.4867	46.39	1.49	42.644	3.537	39.58	7.16
0.97	57.1917	0.1241	50.705	0.552	45.96	1.647	42.4	3.73	39.45	7.373
0.98	56.3832	0.1495	49.99	0.651	45.57	1.803	42.2	3.91	39.2399	7.746
0.99	55.4307	0.1862	49.18	0.7669	45.18	1.97	41.85	4.24	38.966	8.2507
1	54.93	0.289	48.548	0.9084	44.55	2.279	41.376	4.736	38.5381	9.06

5.3.2 Result of satellite image 2 of 512×512 size

Satellite image 2 of 512×512 pixel size. The variation of PSNR with fractional order at different CR is shown in figure 5.7 and the variation of MSE with fractional order at different CR shown in figure 5.8.

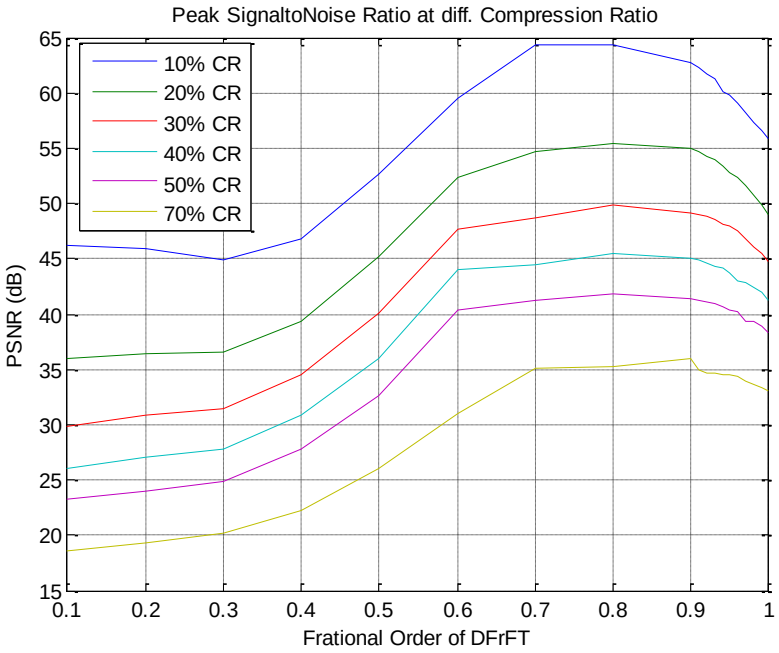

Figure 5.7 PSNR versus fractional order at different CR of image 2

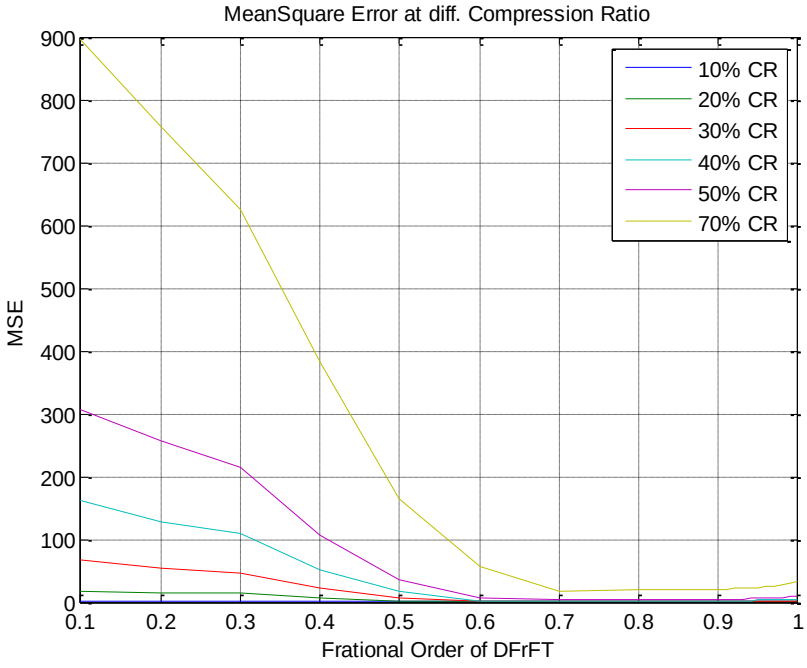

Figure 5.8 MSE versus fractional order at different CR of image 2

At 30% of Compression Ratio

Satellite image 2 is compressed by using DFrFT at 30% CR and results are shown in figure 5.9. Figure 5.9 (a) is original satellite image and remaining three images shown in figure 5.9 (b) to 5.9 (d) are decompressed satellite images at fractional order 0.5, 0.8 and 1 respectively.

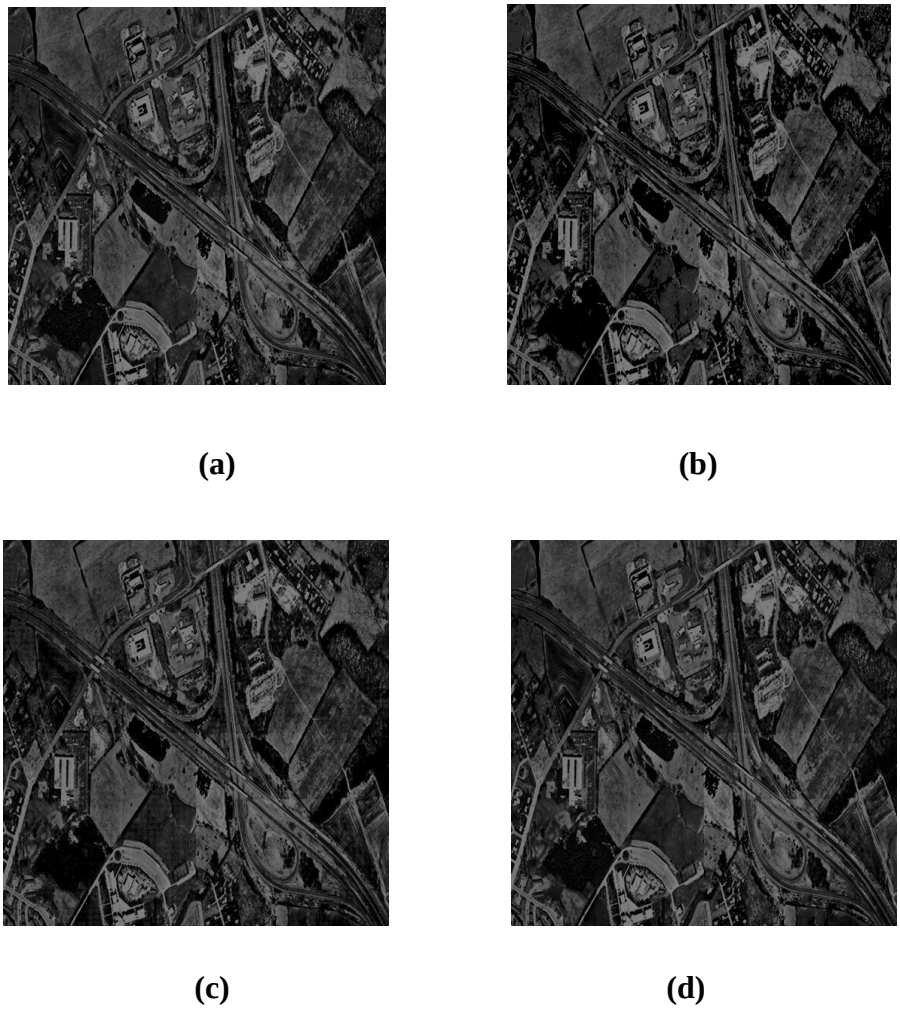

(a) **(b)**

(c) **(d)**

Figure 5.9 Satellite Image 2 at different value of fractional order (a) original images, (b) decompressed image at '0.5' fractional order , (c) decompressed image at optimum fractional order '0.8' and (d) decompressed image at fractional order '1'

At 50% of Compression Ratio

Similarly at 50% CR, the decompressed images are shown in figure 5.10 (b), 5.10 (c) and 5.10 (d) at fractional order 0.5, 0.8 and 1 respectively. Figure 5.10 (b) is decompressed satellite image in which best results are obtained i.e. maximum PSNR and minimum MSE are obtained.

(a)

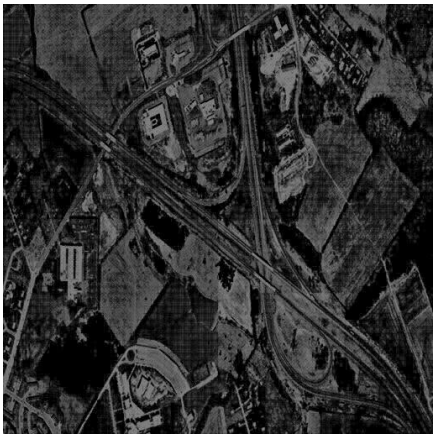

(b)

(c)

(d)

Figure 5.10 Satellite Image 2 at different value of fractional order (a) original images, (b) decompressed image at '0.5' fractional order , (c) decompressed image at optimum fractional order '0.8' and (d) decompressed image at fractional order '1'

At 70% of Compression Ratio

With 70% CR and using DFrFT for satellite image compression, the results for compression shown in figure 5.11 in four images. Out of four images figure 5.11 (a) is original satellite image, figure 5.11 (c) is decompressed satellite image at fractional order in which the

optimum results are obtained. And figure 5.11 (d) is decompressed satellite images at fractional order 1.

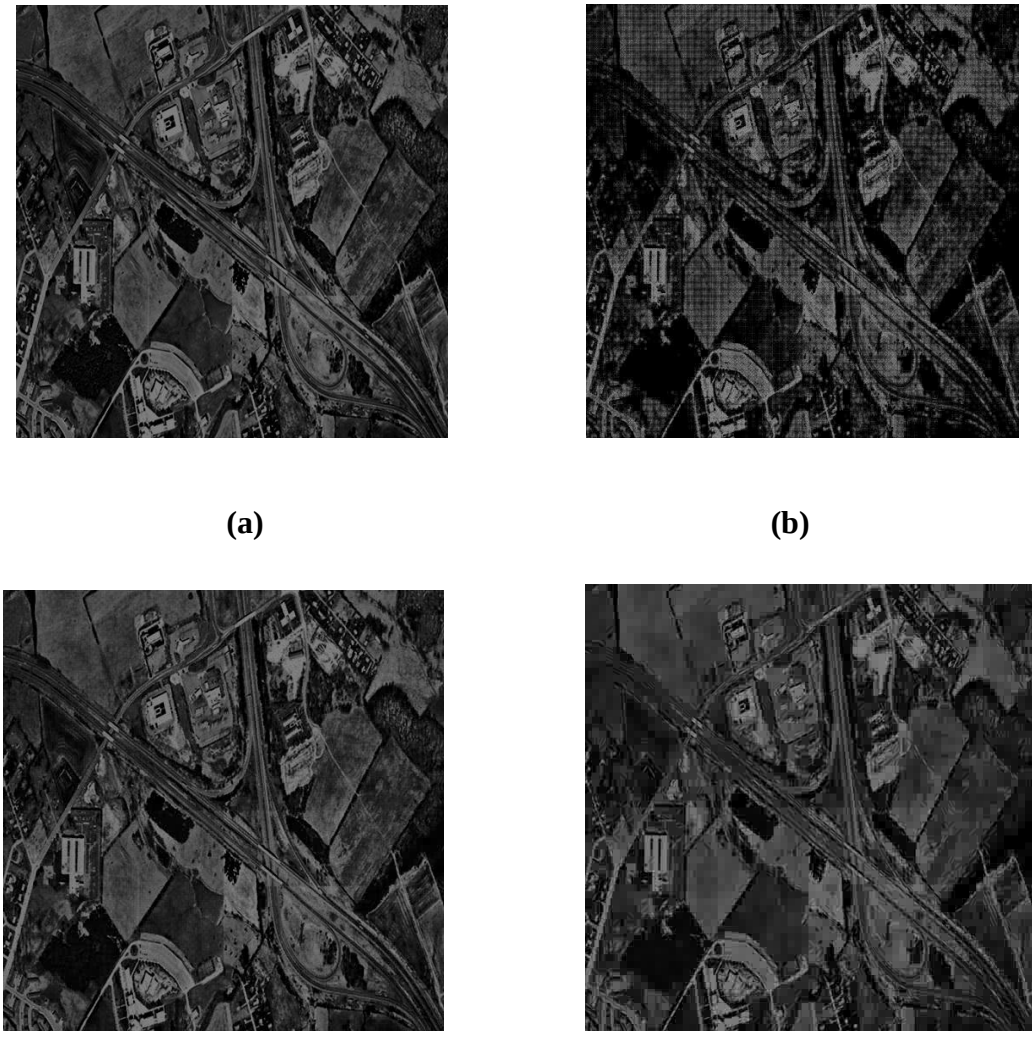

(a) **(b)**

(c) **(d)**

Figure 5.11 Satellite Image 2 at different value of fractional order (a) original images, (b) decompressed image at '0.5' fractional order , (c) decompressed image at optimum fractional order '0.9' and (d) decompressed image at fractional order '1'

Figure 5.9 (c), 5.10 (c), 5.11 (c) shows decompressed images at optimum fractional order a=0.8, 0.8 and 0.9 in which best result are achieved, for 30 %, 50% and 70% CR respectively. From this it is clear that better decompressed images are obtained as compared to FT. The corresponding MSE and PSNR are shown in table 5.9.

Table 5.2 Result of Satellite image compression using DFrFT of Image 2 at different CR%

Fractional Order(a)	PSNR 10%	MSE 10%	PSNR 20%	MSE 20%	PSNR 30%	MSE 30%	PSNR 40%	MSE 40%	PSNR 50%	MSE 50%
0.1	46.19	1.5601	35.93	16.5667	29.87	66.94	26.05	161.30	23.26	306.40
0.2	45.96	1.647	36.46	14.66	30.87	53.37	27.05	128.01	24.03	257.05
0.3	44.97	2.0703	36.62	14.13	31.45	46.56	27.75	109.11	24.83	213.45
0.4	46.85	1.3415	39.40	7.46	34.55	22.77	30.91	52.63	27.83	107.11
0.5	52.65	0.3538	45.12	1.997	40.11	6.33	36.01	16.28	32.56	36.015
0.6	59.53	0.0723	52.37	0.3762	47.63	1.12	44.06	2.5447	40.34	6.009
0.7	64.36	0.0238	54.71	0.2195	48.64	0.888	44.50	2.30	41.26	4.859
0.8	64.33	0.0240	55.38	0.1883	49.81	0.678	45.42	1.8642	41.83	4.262
0.9	62.70	0.0345	54.93	0.209	49.18	0.7854	44.99	2.058	41.40	4.70
0.91	62.25	0.0387	54.62	0.223	49.06	0.8059	44.83	2.13	41.30	4.8113
0.92	61.68	0.0441	54.25	0.244	48.83	0.8559	44.63	2.23	41.12	5.0223
0.93	61.26	0.0486	53.90	0.2646	48.54	0.9086	44.38	2.3704	40.93	5.2452
0.94	60.14	0.0629	53.40	0.2967	48.15	0.9934	44.101	2.528	40.67	5.56
0.95	59.85	0.0672	52.86	0.3362	47.07	1.0890	43.75	2.73	40.35	5.998
0.96	59.04	0.0810	52.29	0.3863	47.31	1.2063	41.58	3.063	40.15	6.27
0.97	58.15	0.995	51.59	0.4504	46.74	1.374	42.89	3.72	39.28	7.665
0.98	57.3005	0.1211	50.77	0.5438	46.12	1.5853	42.42	4.177	39.27	7.68
0.99	56.59	0.1465	49.81	0.6780	45.47	1.8434	41.92	4.80	38.96	8.447
1	55.86	0.1686	49.06	0.8070	44.74	2.1806	41.309	161.30	38.34	9.508

5.3.3 Result of satellite image 3 of 256×256 size

Figure 5.12 shows the variation of PSNR with fractional order atdifferent CR of satellite image 3. Figure 5.13 shows the variation of MSE with fractional order at different CR of satellite image 3.

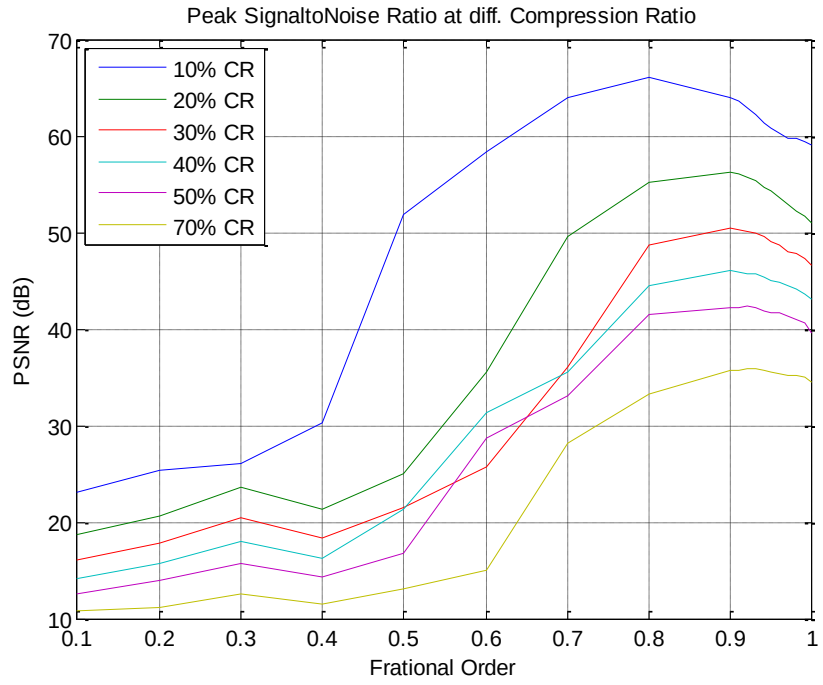

Figure 5.12 PSNR versus fractional order at different CR

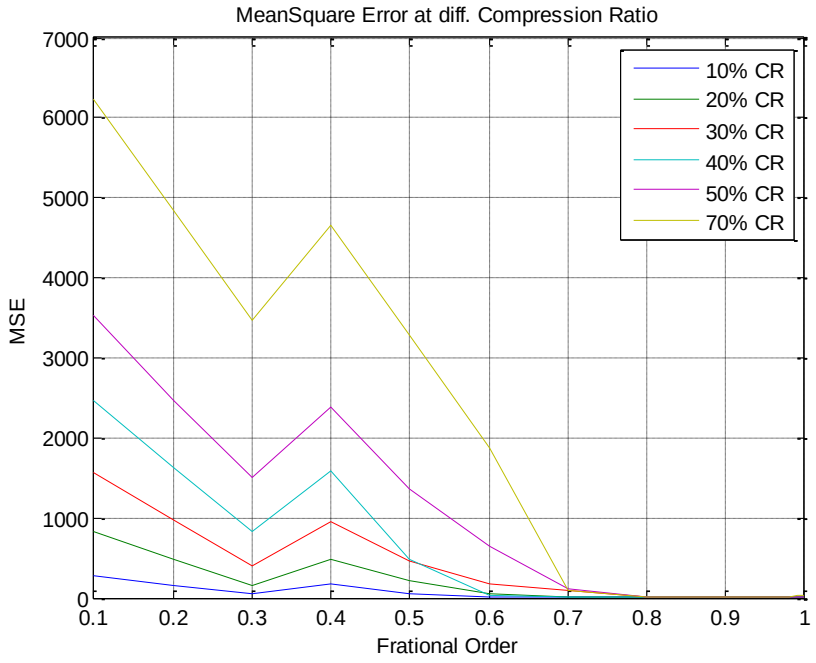

Figure 5.13 MSE versus fractional order at different CR

At 30 % of Compression Ratio

The compression results of satellite image using discrete fractional Fourier transform are shown in figure 5.14 at 30 % CR. The decompressed satellite images at different fractional

order are shown in figure 5.14 (b), 5.14 (c) and 5.14 (d). Figure 5.14 (c) is satellite decompressed images having optimum fractional order.

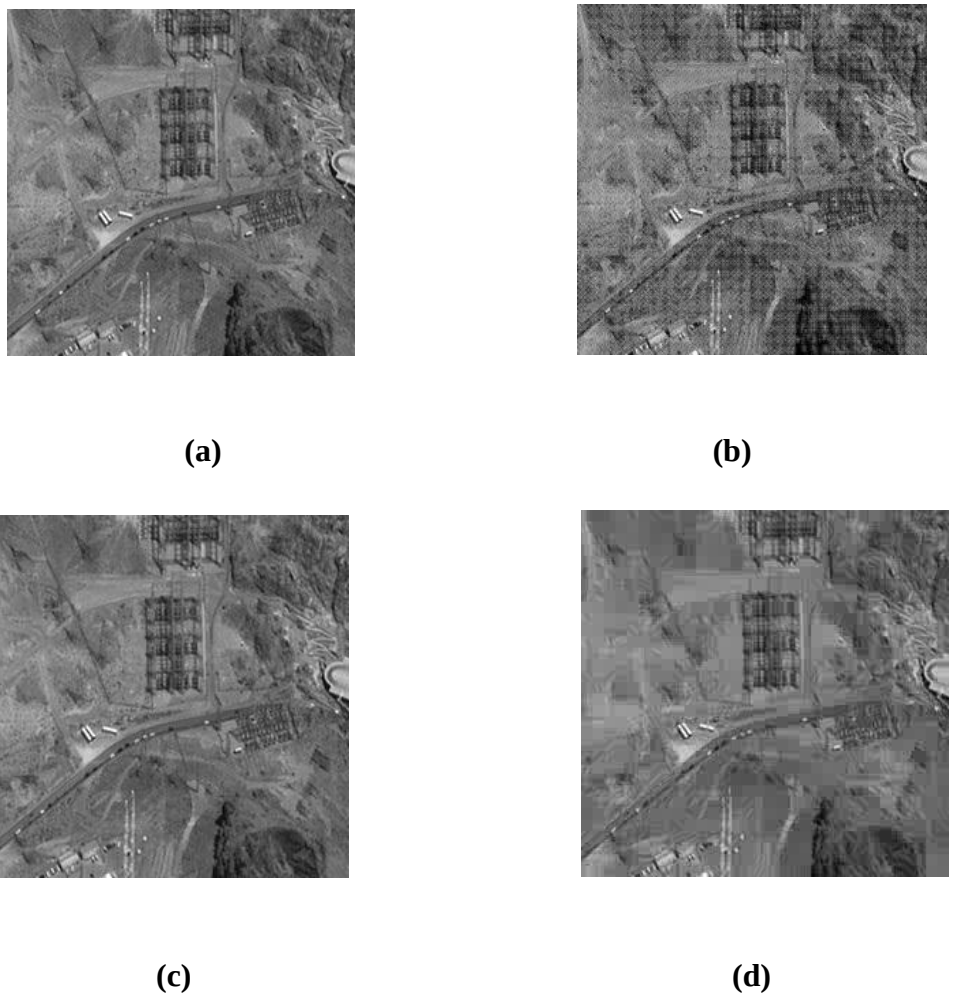

(a) **(b)**

(c) **(d)**

Figure 5.14 Satellite Image 3 at different value of fractional order (a) original images, (b) decompressed image at '0.5' fractional order , (c) decompressed image at optimum fractional order '0.9' and (d) decompressed image at fractional order '1'

At 50% of Compression Ratio

For the case of 50% CR, the results of satellite image compression of satellite image 3 are shown in figure 5.15. The optimum domain of DFrFT is a=0.92 and corresponding decompressed image shown in figure 5.15 (c) and figure 5.15 (d) is decompressed image having fractional order 1.

(a) **(b)**

(c) **(d)**

Figure 5.15 Satellite Image 3 at different value of fractional order (a) original images, (b) decompressed image at '0.5' fractional order , (c) decompressed image at optimum fractional order '0.92' and (d) decompressed image at fractional order '1'

At 70% of Compression Ratio

Similarly at 70 % CR, if we compared the four satellite images shown in figure 5.16, than it is clear that figure 5.16 (c) is the best quality of decompressed image and having best results as at this fractional order the minimum MSE and maximum PSNR obtained. Figure 5.16 (d) is decompressed satellite image at fractional order 1 i.e. conventional Fourier transform.

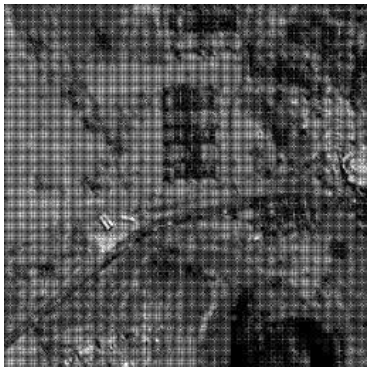

(a) **(b)**

(c) **(d)**

Figure 5.16 Satellite Image 3 at different value of fractional order (a) original images, (b) decompressed image at '0.5' fractional order , (c) decompressed image at optimum fractional order '0.91' and (d) decompressed image at fractional order '1'

With compression satellite images using DFrFT the figure 5.14 (c), 5.15 (c) and 5.16 (c) shows decompressed images at optimum fractional orders a=0.9, 0.92 and 0.91 in which best result are achieved for 30 %, 50% and 70% CR respectively. The MSE and PSNR are shown in table 5.9.

Table 5.3 Result of Satellite image compression using DFrFT of Image 3 at different CR%

Fractional Order(a)	PSNR 10%	MSE 10%	PSNR 20%	MSE 20%	PSNR 30%	MSE 30%	PSNR 40%	MSE 40%	PSNR 50%	MSE 50%
0.1	23.12	276.50	18.61	833.59	15.98	1573.35	14.058	2470.50	12.58	3537.59
0.2	25.28	153.39	20.67	482.231	17.83	976.064	15.75	1622.87	14.02	2473.5
0.3	26	45.9367	23.65	162.70	20.48	406.004	17.97	821.411	15.77	1495.8
0.4	30.34	164.00	21.33	481.89	18.35	958.055	16.144	1592.144	14.37	2391.41
0.5	51.86	60.46	24.94	209.93	21.57	456.48	21.27	488.38	16.84	1355.69
0.6	58.38	14.51	35.44	54.75	25.75	174.30	31.33	36.79	28.75	649.66
0.7	66.06	0.00892	49.49	0.34416	35.98	86.4	35.50	8.5922	33.02	112.49
0.8	63.98	0.004974	55.11	0.272	48.68	0.8281	44.42	2.3250	41.56	4.33
0.9	63.94	0.0259	56.17	0.1531	50.38	0.5766	46.0862	1.61	42.23	3.89
0.91	63.58	0.026321	56.0213	0.1582	50.26	0.5976	45.93	1.644	42.26	3.87
0.92	62.89	0.28641	55.67	0.17094	50.0677	0.6290	45.77	1.70	42.33	3.8960
0.93	62.19	0.33630	55.32	0.187	49.86	0.6621	45.65	1.765	42.11	4.0137
0.94	61.29	0.0395	54.73	0.257	49.54	0.715	45.41	1.8665	41.92	4.18
0.95	60.78	0.0485	54.26	0.24283	49.11	0.79	45.0653	2.032	41.74	4.34
0.96	60.22	0.0546	53.628	0.28921	48.73	0.867	44.77	2.17	41.59	4.5260
0.97	59.81	0.0622	52.87	0.3371	47.92	1.052	44.49	2.32	41.32	4.82
0.98	59.81	0.068	52.16	0.397	47.87	1.067	44.16	2.50	40.88	5.34
0.99	59.46	0.074	51.63	0.45	47.21	1.24	43.63	2.83	40.53	5.787
1	59	0.082	50.92	0.5293	46.54	1.45	43.01	3.27	39.6	6.556

5.3.4 Result of satellite image 4 of 256×256 size

Image 4 is satellite image of 256×256 pixel size. Figure 5.17 shows the variation of PSNR

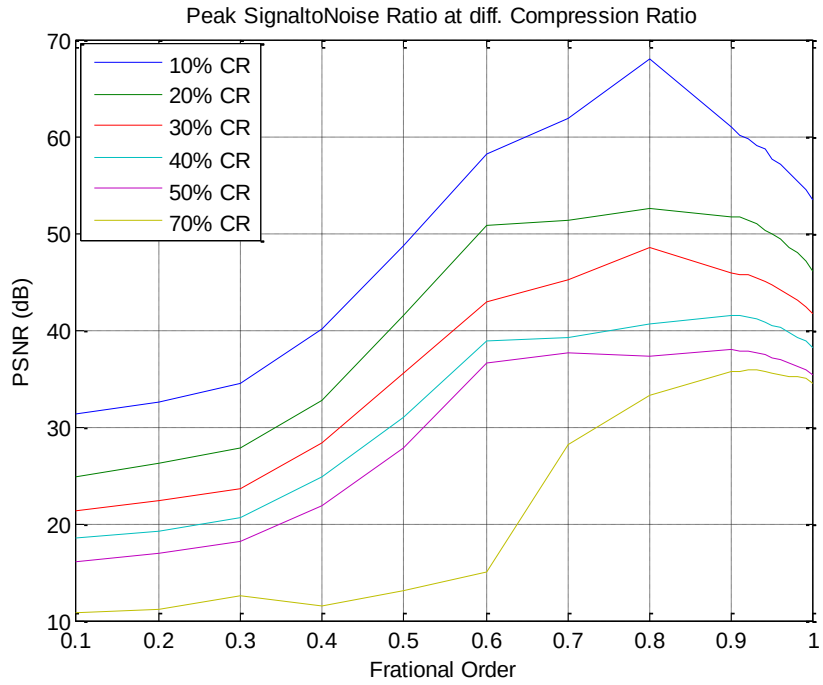

Figure 5.17 PSNR versus fractional order at different CR of image 4

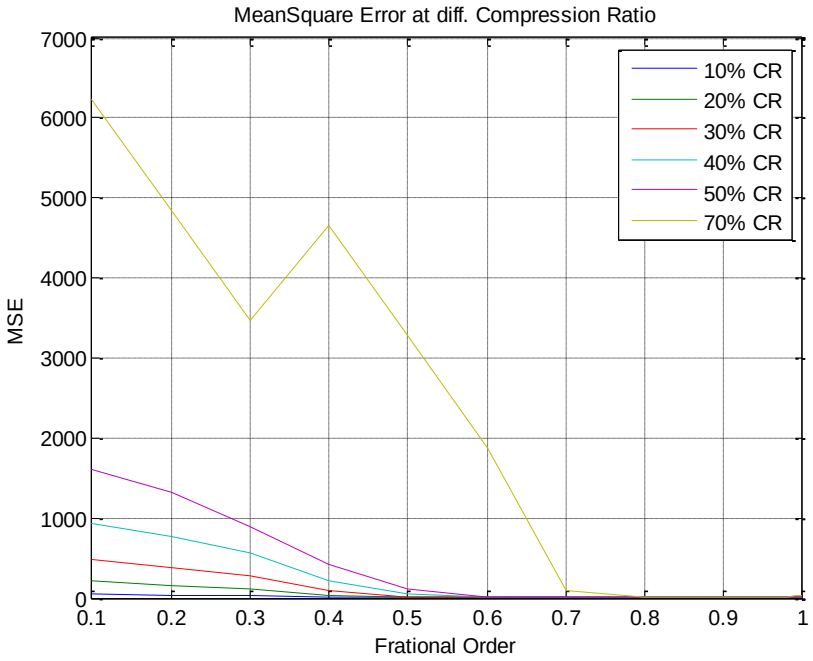

Figure 5.18 MSE versus fractional order at different CR of image 4

with fractional order atdifferent CR. Figure 5.18 shows the variation of PSNR with fractional order at different CR.

At 30 % of Compression Ratio

Using DFrFT, the results are shown in figure 5.19 at 30% CR. The optimum domain of DFrFT is a=0.9 and corresponding decompressed image shown in figure 5.19 (c) and figure 5.19 (d) is decompressed image having fractional order 1.

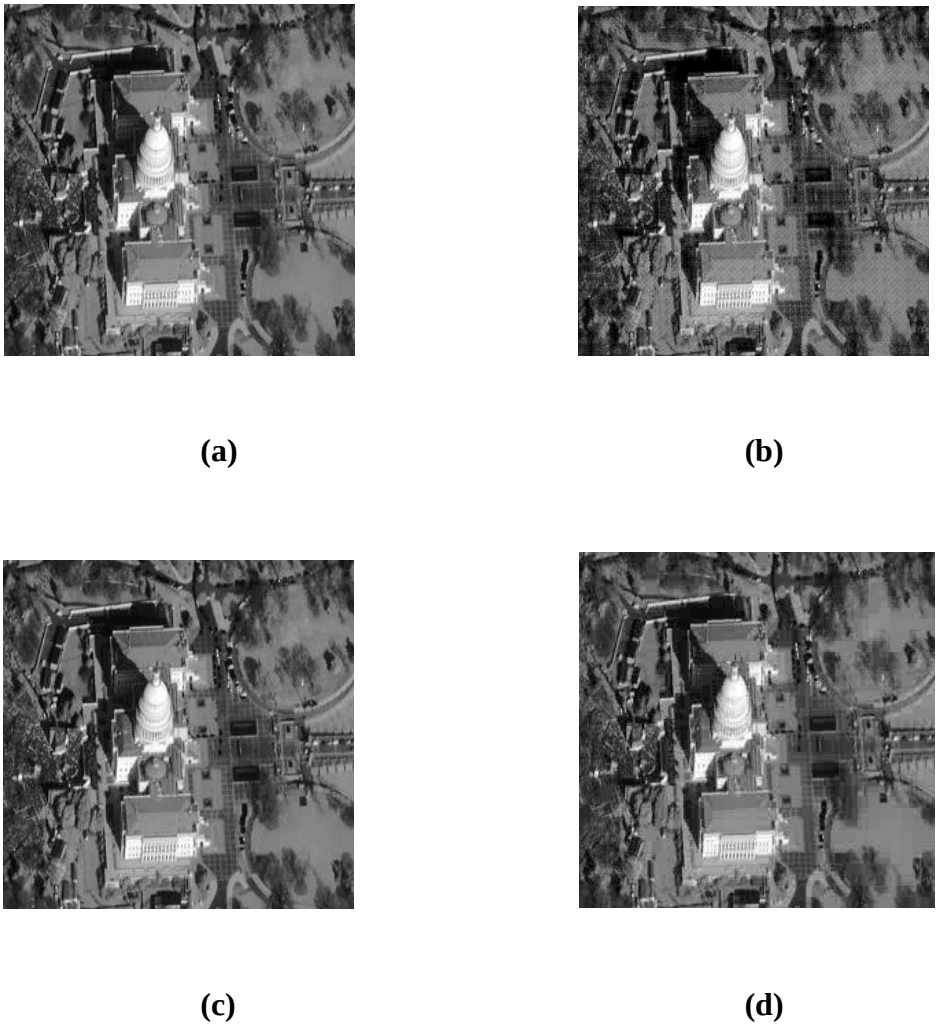

(a) **(b)**

(c) **(d)**

Figure 5.19 Satellite Image 4 at different value of fractional order (a) original images, (b) decompressed image at '0.5' fractional order , (c) decompressed image at optimum fractional order '0.9' and (d) decompressed image at fractional order '1'

At 50 % of Compression Ratio

In case of 50% CR, the results of satellite image compression of satellite image 3 are shown

in figure 5.20. The optimum domain of DFrFT is a=0.91 and corresponding decompressed image shown in figure 5.20 (c) and figure 5.20 (d) is decompressed image having fractional order 1.

(a)

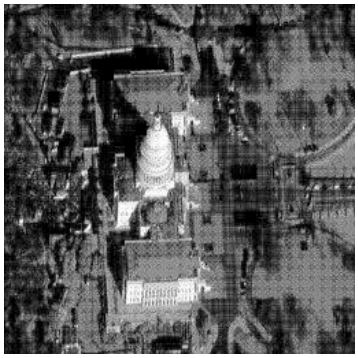

(b)

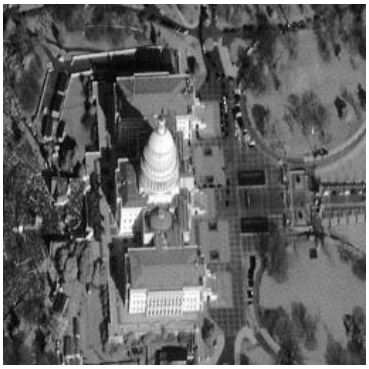

(c)

(d)

Figure 5.20 Satellite Image 4 at different value of fractional order (a) original images, (b) decompressed image at '0.5' fractional order , (c) decompressed image at optimum fractional order '0.91' and (d) decompressed image at fractional order '1'

At 70 % of Compression Ratio

At 70% CR and using DFrFT for satellite image compression, the results for compression shown in figure 5.21 in four images. Out of four images figure 5.21 (a) is original satellite image, figure 5.21 (c) is decompressed satellite image at fractional order in which the

optimum results are obtained. And figure 5.21 (d) is decompressed satellite images at fractional order 1.

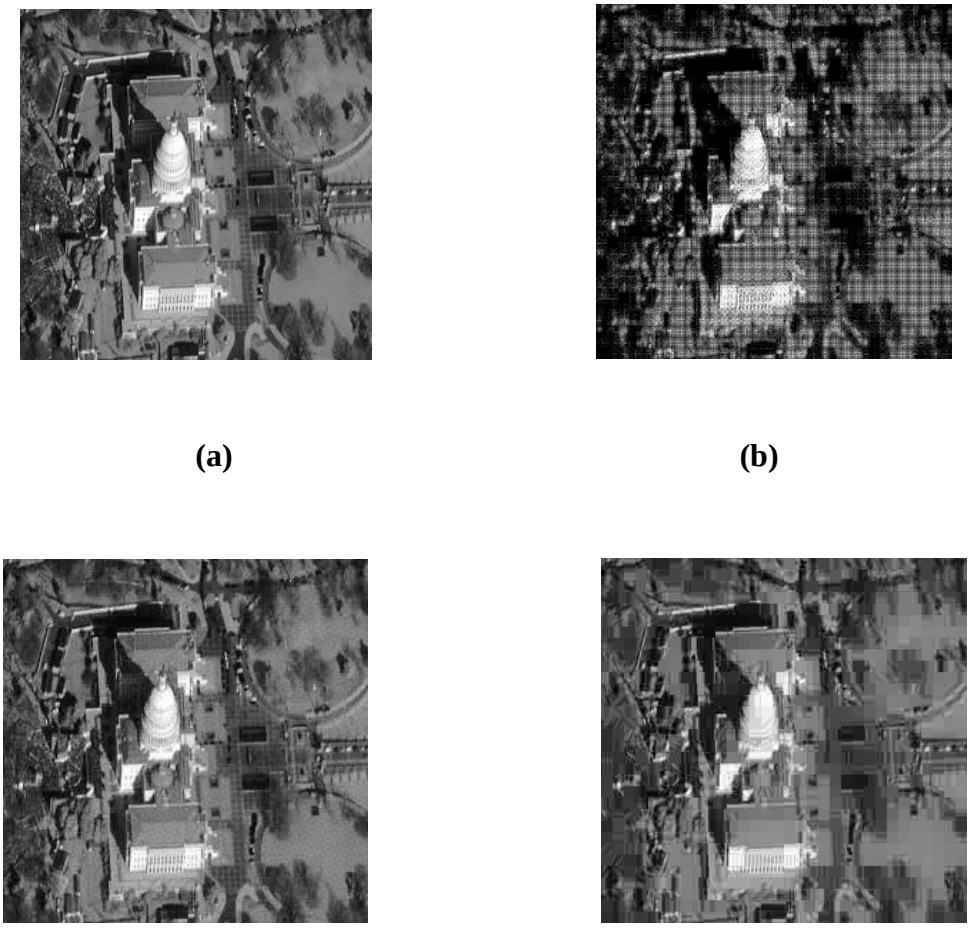

(a) **(b)**

(c) **(d)**

Figure 5.21 Satellite Image 4 at different value of fractional order (a) original images, (b) decompressed image at '0.1' fractional order , (c) decompressed image at optimum fractional order '0.93' and (d) decompressed image at fractional order '1'

The best results are shown in figure 5.19 (c), 5.20 (c) and 5.21 (c) which decompressed images at optimum fractional order a=0.91, 0.91 and 0.93 for 30 %, 50% and 70% CR respectively. The corresponding MSE and PSNR are shown in table 5.9.

Table 5.4 Result of Satellite image compression using DFrFT of Image 4 at different CR%

Fractional Order(a)	PSNR 10%	MSE 10%	PSNR 20%	MSE 20%	PSNR 30%	MSE 30%	PSNR 40%	MSE 40%	PSNR 50%	MSE 50%
0.1	31.2602	48.64	24.906	210.08	21.286	484.15	18.44	930.24	16.0918	1599.2
0.2	32.604	35.35	26.227	155.17	22.30	382.27	19.29	764.01	16.93	1318.1
0.3	34.5	23.04	27.72	109.82	23.64	280.78	20.64	560.62	18.174	898.9
0.4	40.128	6.313	32.79	34.170	28.32	95.71	24.77	216.34	21.81	428.3
0.5	48.76	0.8640	41.41	4.693	35.54	18.127	30.94	52.25	27.73	109.59
0.6	58.128	0.101	52.56	0.3600	48.45	0.9580	39.29	7.651	37.55	10.90
0.7	67.896	0.0106	50.74	0.547	42.85	3.36	38.91	8.35	36.61	14.18
0.8	61.81	0.0429	51.34	0.476	45.14	1.99	40.66	5.57	37.36	11.91
0.9	60.90	0.0528	51.74	0.43	45.88	1.677	41.526	4.57	37.960	10.54
0.91	60.090	0.0649	51.70	0.439	45.78	1.716	41.41	4.69	37.8312	10.71
0.92	59.812	0.067	51.32	0.479	45.64	1.7714	41.26	4.864	37.74	10.923
0.93	59.054	0.0808	50.96	0.529	45.34	1.898	41.08	5.062	37.61	11.2665
0.94	58.655	0.886	50.24	0.614	45.004	2.054	40.8	5.406	37.44	11.71
0.95	57.61	0.1127	49.97	0.654	44.60	2.253	40.5	5.782	37.188	12.42
0.96	57.12	0.126	49.32	0.759	44.14	2.50	40.22	6.17	36.87	13.35
0.97	56.21	0.1554	48.52	0.9124	43.61	2.828	39.76	6.86	36.53	14.4507
0.98	55.30	0.1915	48.01	1.027	42.997	3.2611	39.29	7.647	36.19	15.61
0.99	54.42	0.2345	47.18	1.2431	42.39	3.747	38.85	8.465	35.84	16.94
1	53.42	0.2958	46.11	1.5895	41	4.45	38.20	9.81	35.33	19.044

5.4 RESULTS AND SIMULATIOS USING DFrCT

The simulation result of the of four different satellite images using DFrCT at different Compression ratio at 10%, 30%, 50% and 70% are given below.

5.4.1 Result of satellite image 1 of 512×512 Size

Using DFrCT, the result of satellite image 1 shown in figure 5.22 and 5.23. Figure 5.22 shows the variation of PSNR with fractional order at different CR. Figure 5.23 shows the variation of PSNR with fractional order at different CR.

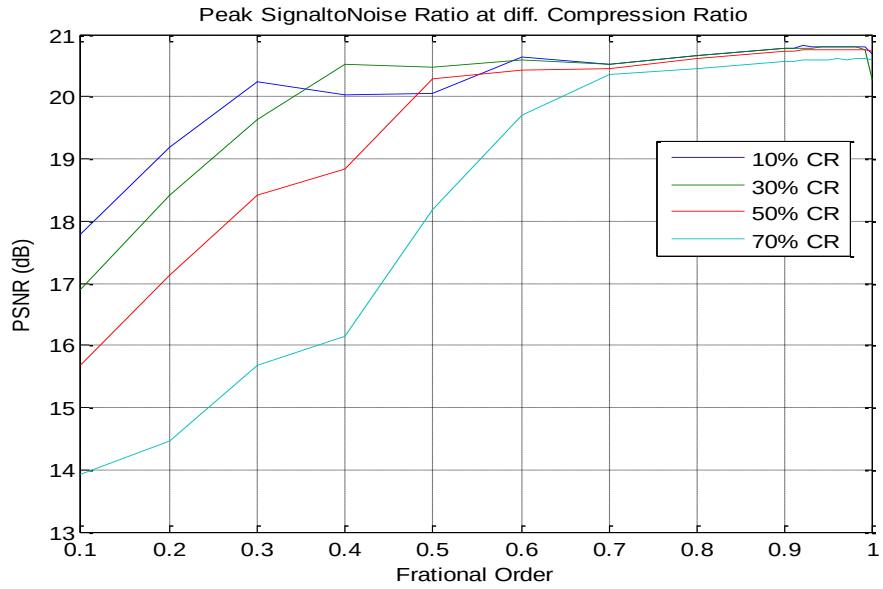

Figure 5.22 PSNR versus fractional order at different CR

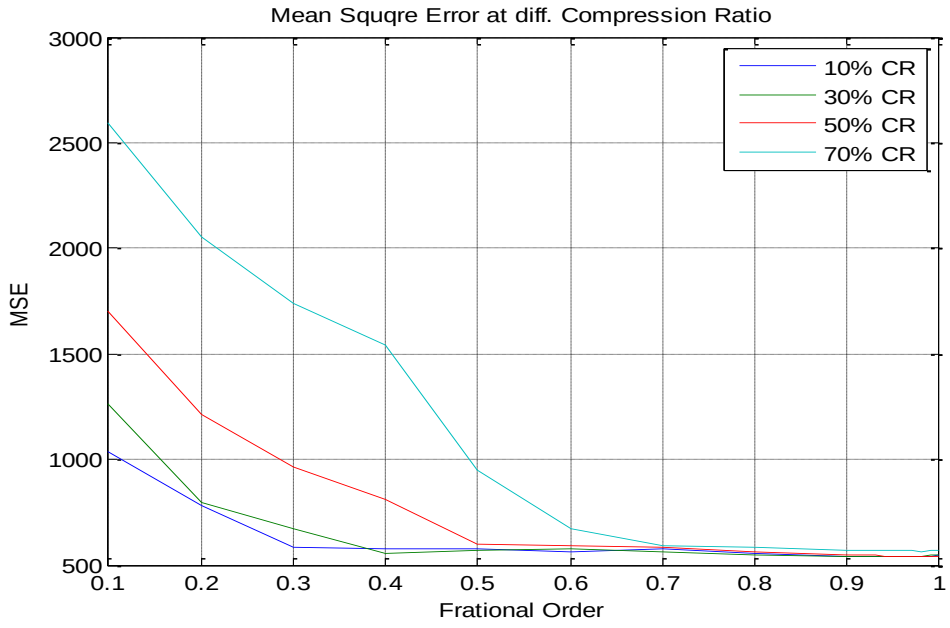

Figure 5.23 MSE versus fractional order at different CR

At 30 % of Compression Ratio

At 30% CR and using DFrFT for satellite image compression, the results for compression shown in figure 5.24 in four images. Figure 5.24 (a) is original satellite image, figure 5.24 (c) is decompressed satellite image at fractional order in which the optimum results are obtained. And figure 5.24 (d) is decompressed satellite images at fractional order 1.

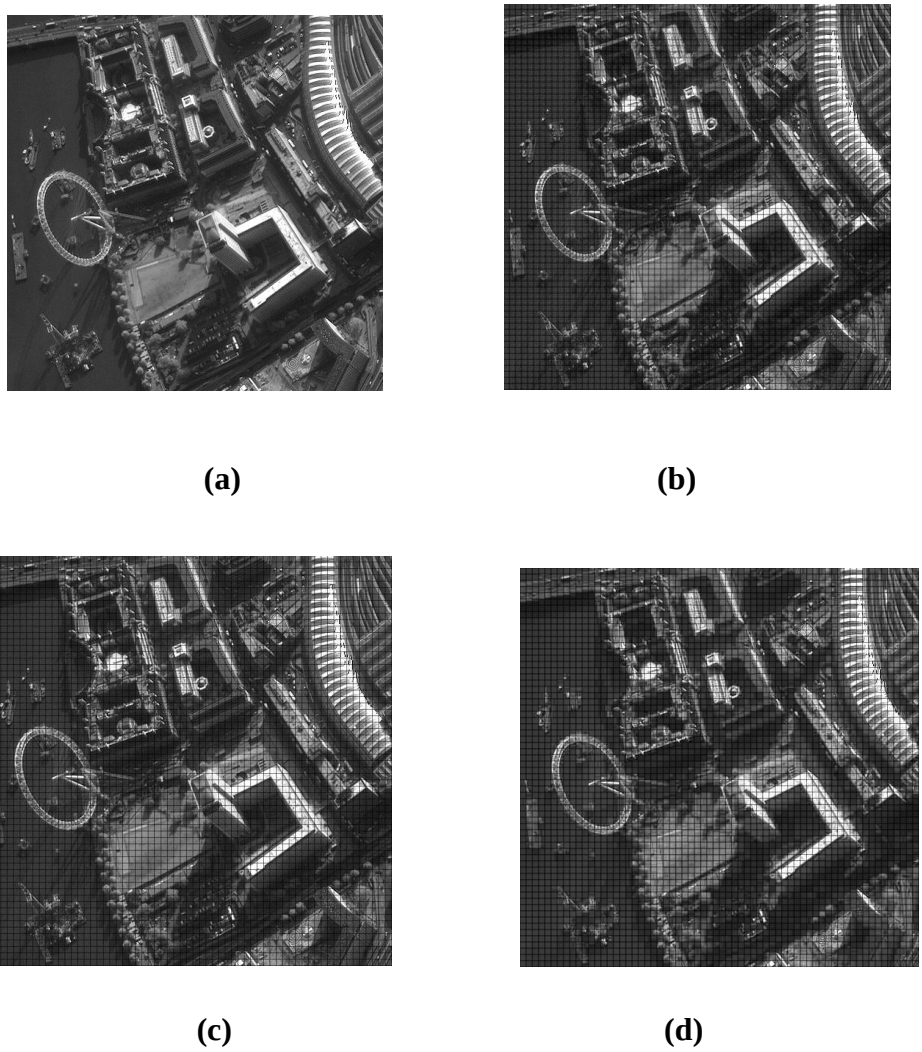

(a) **(b)**

(c) **(d)**

Figure 5.24 Satellite Image 1 at different value of fractional order (a) original images, (b) decompressed image at '0.5' fractional order , (c) decompressed image at optimum fractional order '0.98' and (d) decompressed image at fractional order '1

At 50 % of Compression Ratio

Similarly at 50 % CR, if we compared the four satellite images shown in figure 5.25, than it is clear that figure 5.25 (c) is the best quality of decompressed image and having best results as at this fractional order the minimum MSE and maximum PSNR obtained.

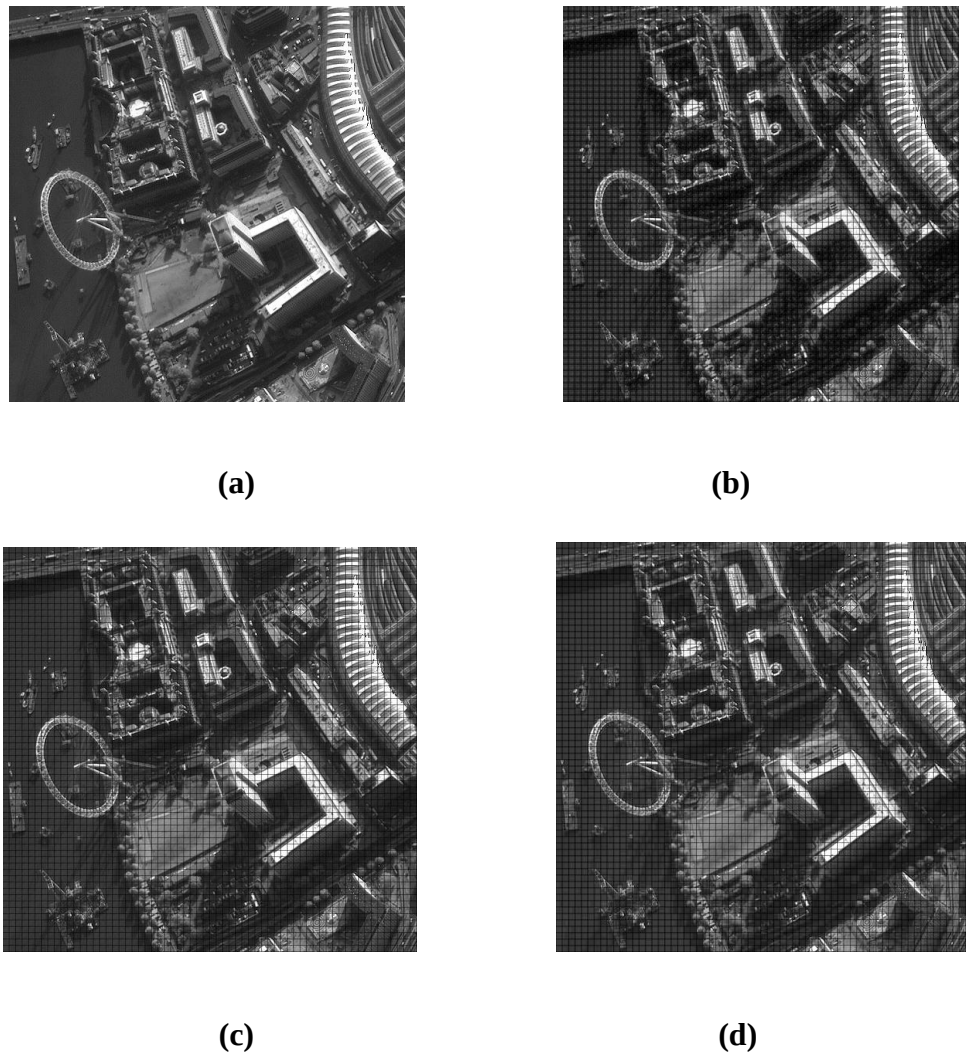

(a) **(b)**

(c) **(d)**

Figure 5.25 Satellite Image 1 at different value of fractional order (a) original images, (b) decompressed image at '0.5' fractional order , (c) decompressed image at optimum fractional order '0.97' and (d) decompressed image at fractional order '1'

At 70 % of Compression Ratio

Using DFrFT, the results are shown in figure 5.6 at 70% CR. Figure 5.26 (a) is original

satellite image and remaining three images shown in figure 5.26 (b) to 5.26 (d) are decompressed satellite images at fractional order 0.5, 0.8 and 1 respectively..

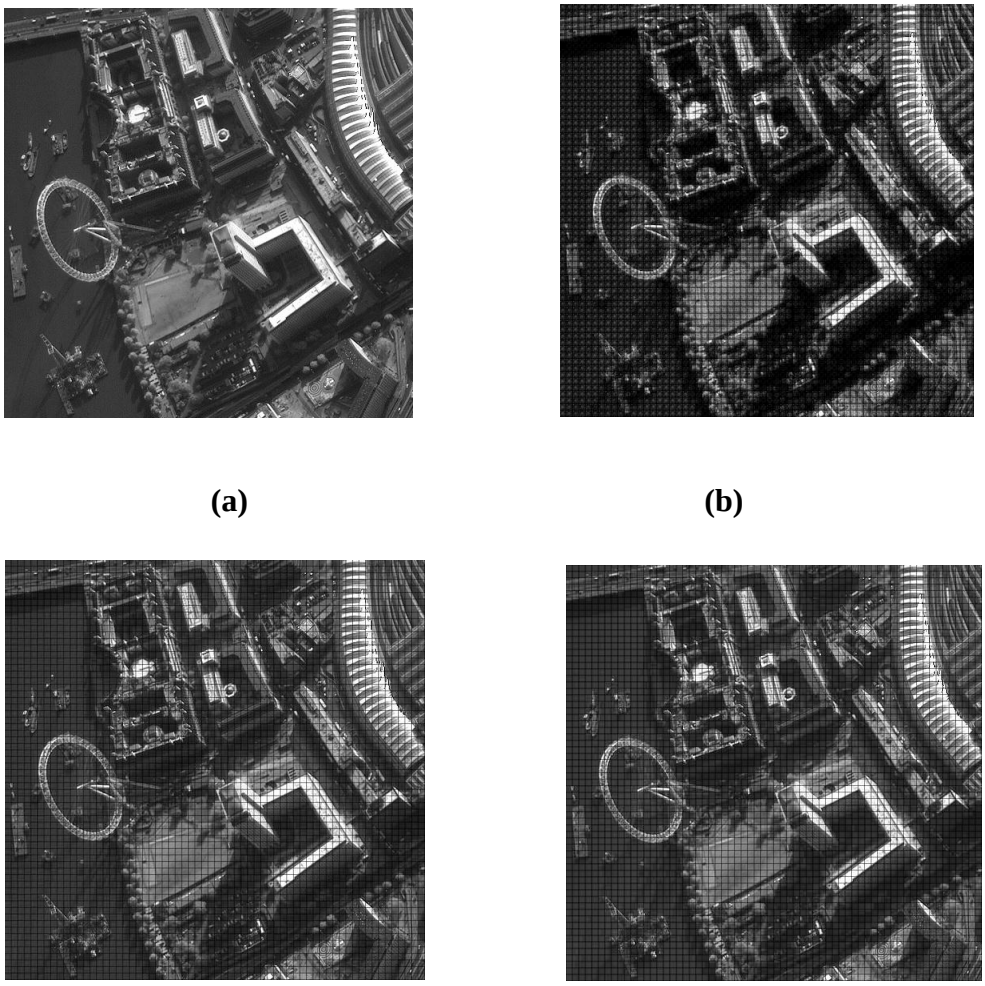

(a) **(b)**

(c) **(d)**

Figure 5.26 Satellite Image 1 at different value of fractional order (a) original images, (b) decompressed image at '0.5' fractional order , (c) decompressed image at optimum fractional order '0.96' and (d) decompressed image at fractional order '1'

By using DFrCT , it is clear that for same CR, it gives better-decompressed image as compared to FT. Figure 5.24 (c) ,5.25 (c) and 5.26 (c) shows decompressed images at optimum fractional orders a=0.98, 0.97 and 0.96 in which best result are achieved for 30%, 50% and 70% CR respectively. The corresponding MSE and PSNR are shown in table 5.10.

Table 5.5 Result of Satellite image compression using DFrCT of Image 1 at different CR%

Fractional Order(a)	PSNR 10%	MSE 10%	PSNR 30%	MSE 30%	PSNR 40%	MSE 40%	PSNR 50%	MSE 50%
0.1	17.79	1035	16.9	1264.158	15.69	1704	13.93	2592
0.2	19.19	7832.76	18.41	7977.002	17.137	1214.43	14.456	2051
0.3	20.25	587.08	19.64	668.42	18.41	963.32	15.67	1739.93
0.4	21.03	506.89	20.53	558.35	18.84	811.95	16.14	1545.2
0.5	21.05	509	20.98	567.21	20.277	601.633	18.17	951.05
0.6	20.63	561.03	20.58	578.26	20.435	587.86	19.7	668.918
0.7	20.53	575.0212	20.509	558.66	20.453	586.2	20.35	594.26
0.8	20.67	557.044	20.65	544.27	20.6121	564.13	20.44	585.12
0.9	20.78	543.083	20.77	543.2	20.73	548.69	20.57	569.62
0.91	20.786	542.39	20.78	543.517	20.741	548.13	20.576	569.22
0.92	20.791	541.84	20.7821	543	20.745	547.58	20.579	568.847
0.93	21	541.3	20.786	542.42	20.749	547.074	20.6	566.166
0.94	20.798	540.9	20.79	542.02	20.75	542.51	20.58	567.91
0.95	20.801	540.66	20.793	541.68	20.758	546.02	20.59	567.38
0.96	20.803	540.4	20.79	541.39	20.76	545.61	20.61	566.77
0.97	20.804	540.24	20.795	541.61	20.7644	545.28	20.59	566.51
0.98	20.805	540.133	20.7977	541.11	20.76	545.05	20.606	565.92
0.99	20.806	540.09	20.799	540.95	20.76	599.99	20.6081	565.26
1	20.79	541.09	20.27	540.89	20.74	544.98	20.59	563.96

5.4.2 Result of satellite image 2 of 512×512 Size:

Image 2 is satellite image of 512×512 pixel size. Figure 5.27 shows the variation of PSNR with fractional order at different CR. Figure 5.28 shows the variation of MSE with fractional order at different CR.

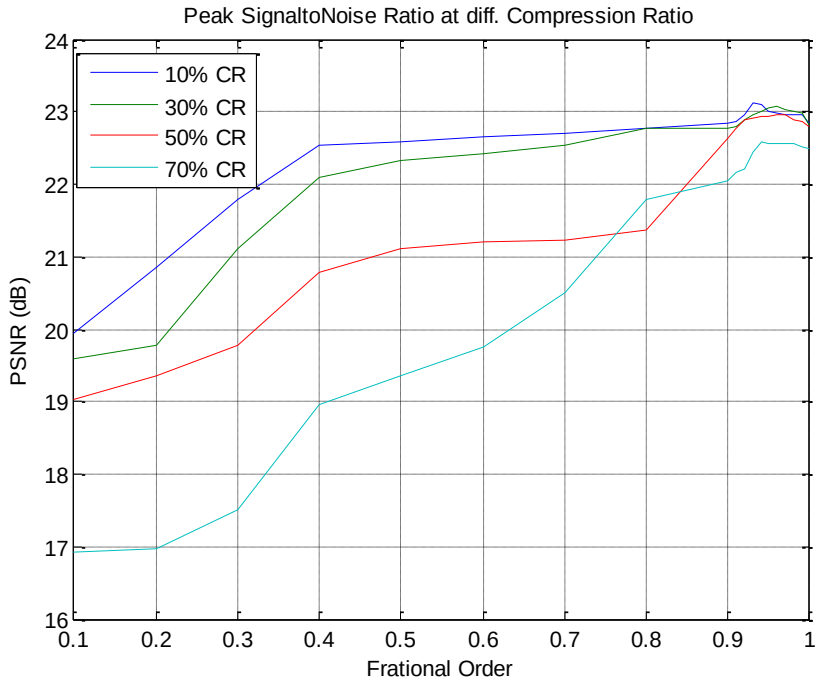

Figure 5.27 PSNR versus fractional order at different CR

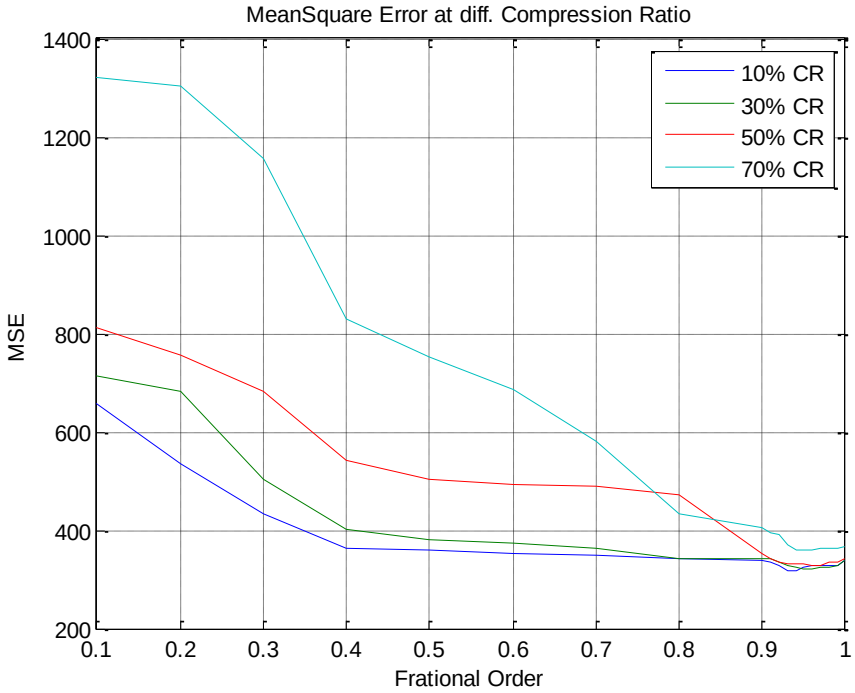

Figure 5.28 MSE versus fractional order at different CR

At 30 % of Compression Ratio

Using DFrFT, the results are shown in figure 5.29 at 30% CR The optimum domain of DFrFT is a=0.95 and corresponding decompressed image shown in figure 5.29 (c) and figure 5.29 (d) is decompressed image having fractional order 1.

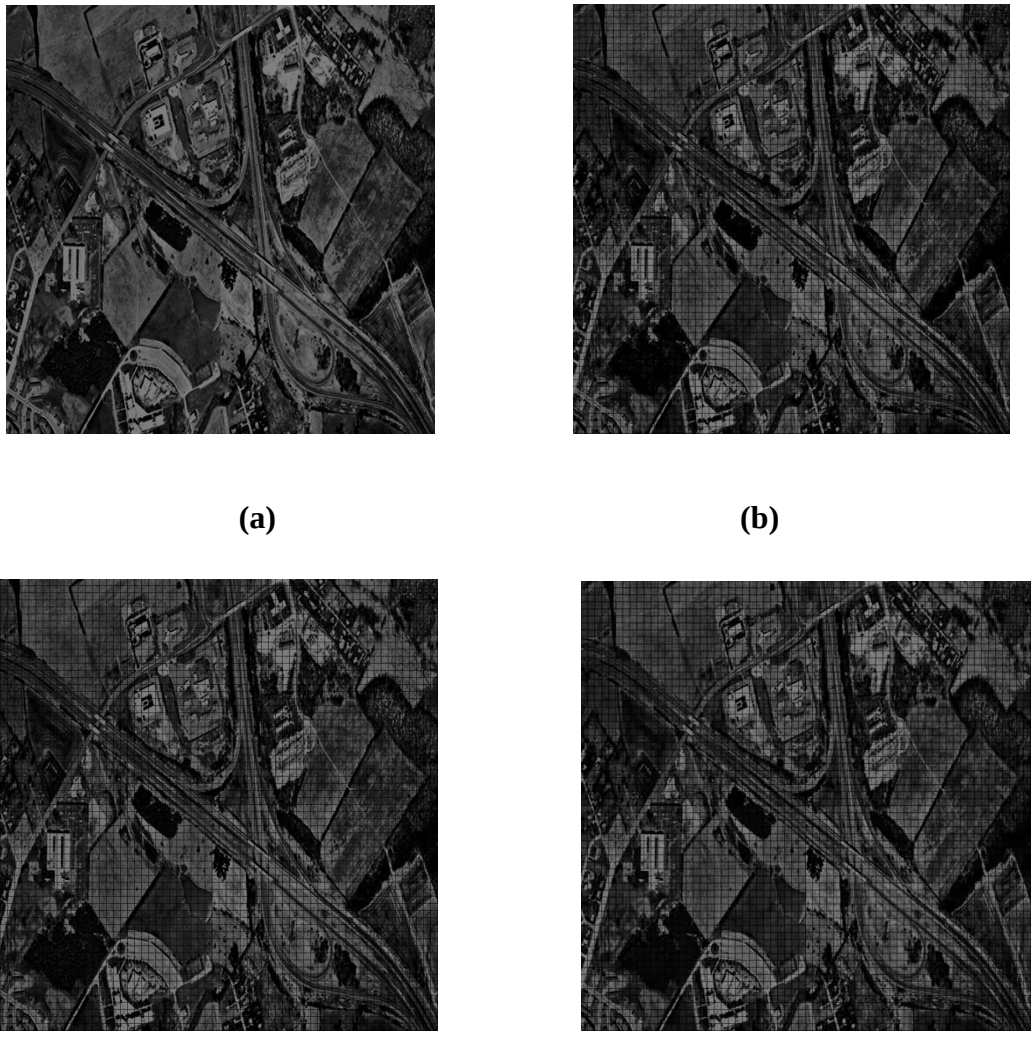

(a) **(b)**

(c) **(d)**

Figure 5.29 Satellite Image 2 at different value of fractional order (a) original images, (b) decompressed image at '0.5' fractional order , (c) decompressed image at optimum fractional order '0.95' and (d) decompressed image at fractional order '1'

At 50 % of Compression Ratio

In case of 50% CR, the results of satellite image compression of satellite image 3 are shown in figure 5.30. The optimum domain of DFrFT is a=0.91 and corresponding decompressed image shown in figure 5.30(c) and figure 5.30 (d) is decompressed image having fractional order 1.

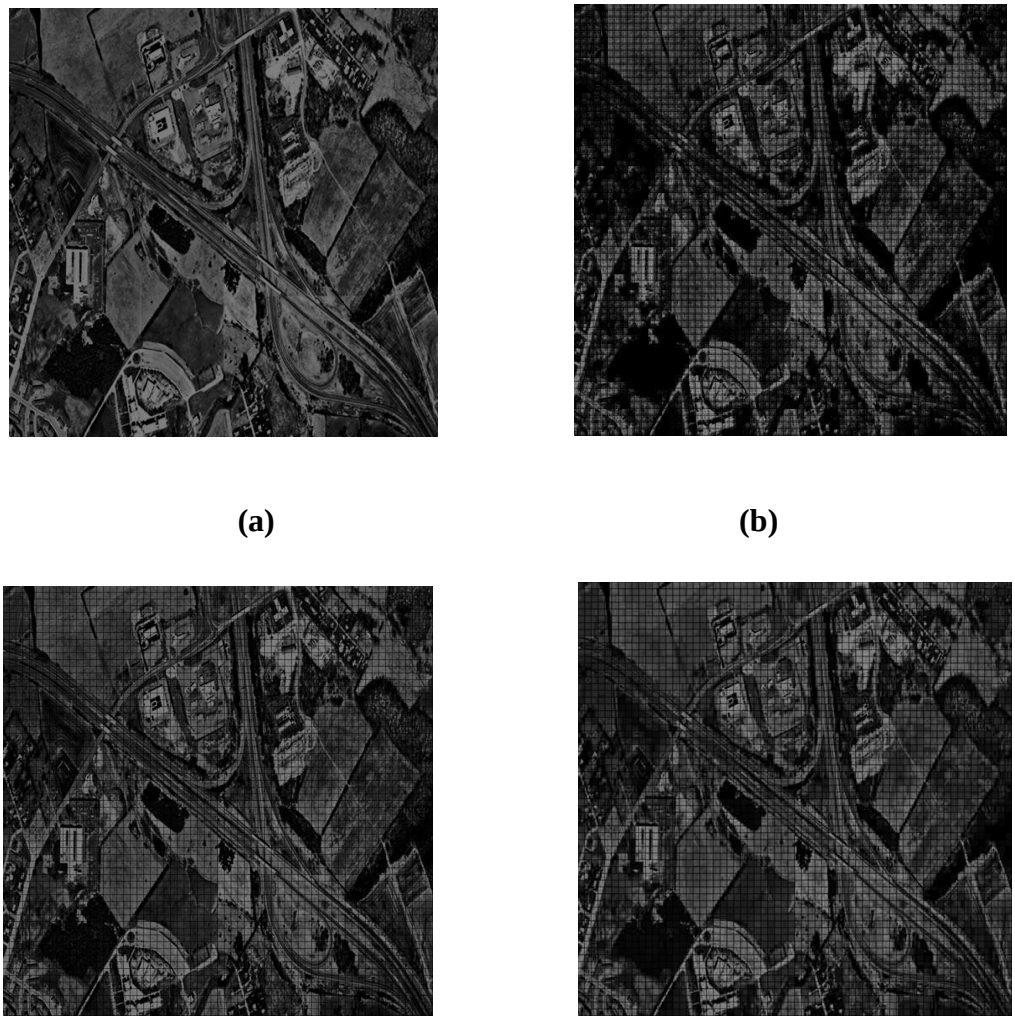

(a) **(b)**

(c) **(d)**

Figure 5.30 Satellite Image 2 at different value of fractional order (a) original images, (b) decompressed image at '0.5' fractional order, (c) decompressed image at optimum fractional order '0.97' and (d) decompressed image at fractional order '1'

At 70 % of Compression Ratio

Similarly at 70 % CR, if we compared the four satellite images shown in figure 5.31, then it is clear that figure 5.31 (c) is the best quality of decompressed image and having best results as at this fractional order the minimum MSE and maximum PSNR obtained. Figure 5.31 (d) is decompressed satellite image at fractional order 1 i.e. conventional Cosine transform.

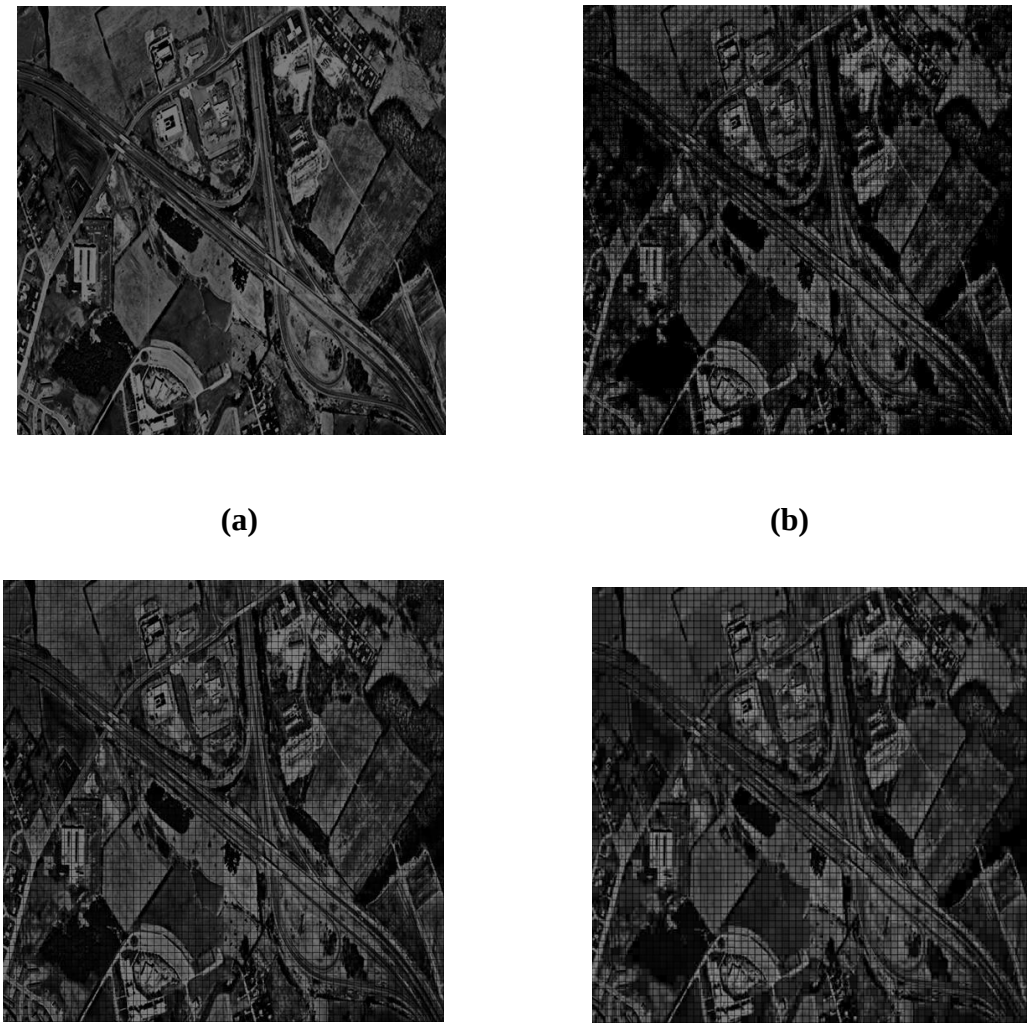

(a) **(b)**

(c) **(d)**

Figure 5.31 Satellite Image 2 at different value of fractional order (a) original images, (b) decompressed image at '0.5' fractional order, (c) decompressed image at optimum fractional order '0.96' and (d) decompressed image at fractional order '1'

The decompressed images at optimum fractional order a=0.95, 0.97 and 0.96 in which best result are achieved for 30 % , 50% and 70% CR are shown in figure 5.29 (c) , 5.30 (c) and 5.31 (c) respectively. The corresponding MSE and PSNR are shown in table 5.10.

Table 5.6 Result of Satellite image compression using DFrCT of Image 2 at different CR%

Fractional Order(a)	PSNR 10%	MSE 10%	PSNR 30%	MSE 30%	PSNR 50%	MSE 50%	PSNR 70%	MSE 70%
0.1	19.94	659.17	19.58	714.793	19.03	811.297	16.92	1321.54
0.2	20.86	533.43	19.78	684.038	19.35	755.231	16.98	1303.40
0.3	21.78	431.59	21.10	504.754	19.78	684.038	17.50	1156.32
0.4	22.54	362.31	22.10	400.940	20.78	543.350	18.95	828.095
0.5	22.58	358.98	22.33	380.259	21.11	503.593	19.36	753.494
0.6	22.65	353.24	22.41	373.319	21.21	492.130	19.76	687.195
0.7	22.71	348.40	22.54	362.310	21.22	490.998	20.55	579.535
0.8	22.78	342.83	22.78	342.831	21.38	473.238	21.78	431.598
0.9	22.85	337.34	22.77	343.621	22.64	354.062	22.04	405.910
0.91	22.87	335.79	22.79	342.042	22.78	342.831	22.17	394.530
0.92	22.95	329.67	22.89	334.256	22.89	334.256	22.22	390.014
0.93	23.13	316.28	22.95	329.670	22.91	332.721	22.45	369.896
0.94	23.11	317.74	23.00	325.896	22.93	331.192	22.58	358.988
0.95	22.99	326.27	23.05	322.166	22.94	330.430	22.57	359.815
0.96	22.99	326.64	23.07	320.686	22.96	328.912	22.56	360.645
0.97	22.97	328.15	23.03	323.653	22.95	329.670	22.55	361.476
0.98	22.96	328.91	23.00	325.896	22.88	335.027	22.55	361.476
0.99	22.95	329.67	22.98	327.401	22.87	335.799	22.51	364.821
1	22.84	338.12	22.83	338.906	22.79	342.042	22.48	367.350

5.4.3 Result of satellite image 3 of 256×256 Size

Image 3 is satellite image of 256×256 pixel size. Figure 5.32 shows the variation of PSNR with fractional order atdifferent CR. Figure 5.33 shows the variation of PSNR with fractional order at different CR.

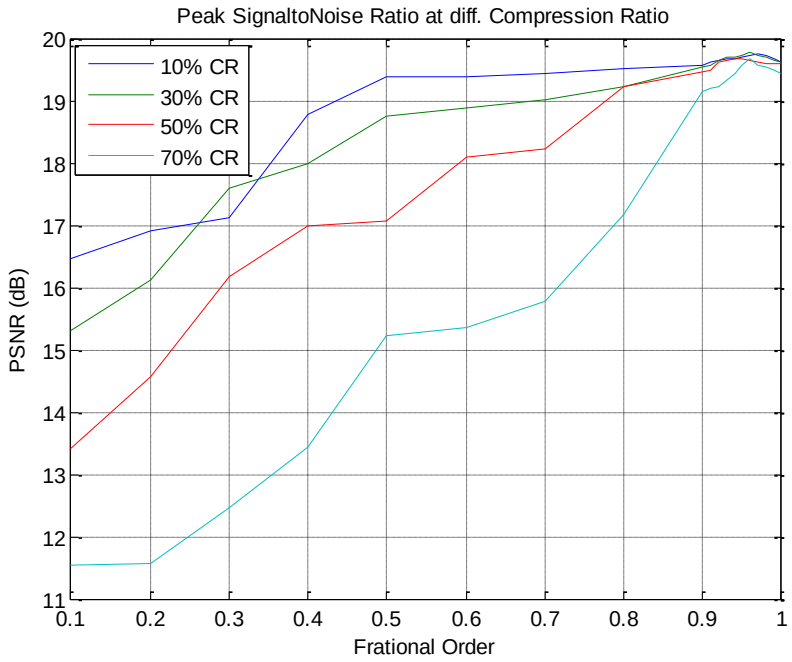

Figure 5.32 PSNR versus fractional order at different CR

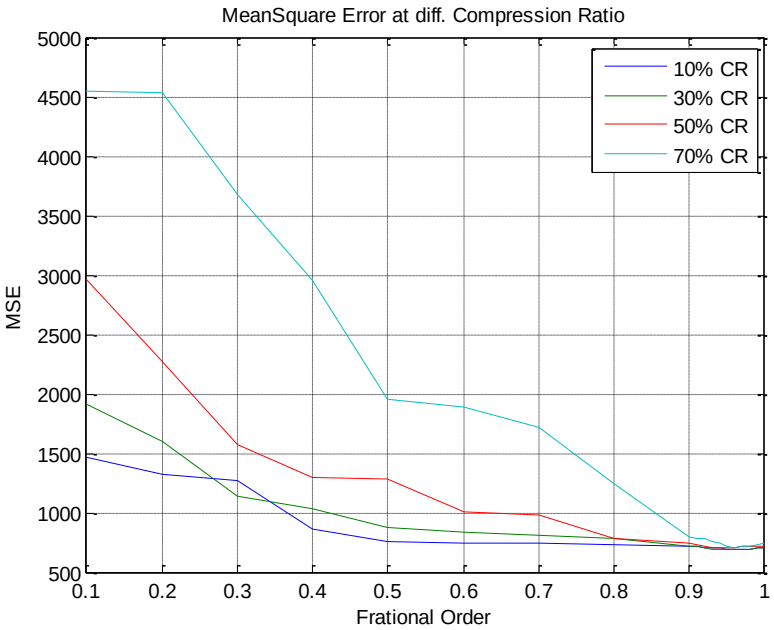

Figure 5.33 MSE versus fractional order at different CR

At 30 % of Compression Ratio

Using DFrFT, the results are shown in figure 5.34 at 30% CR. The optimum domain of DFrFT is a=0.97 and corresponding decompressed image shown in figure 5.34 (c) and figure 5.34 (d) is decompressed image having fractional order 1.

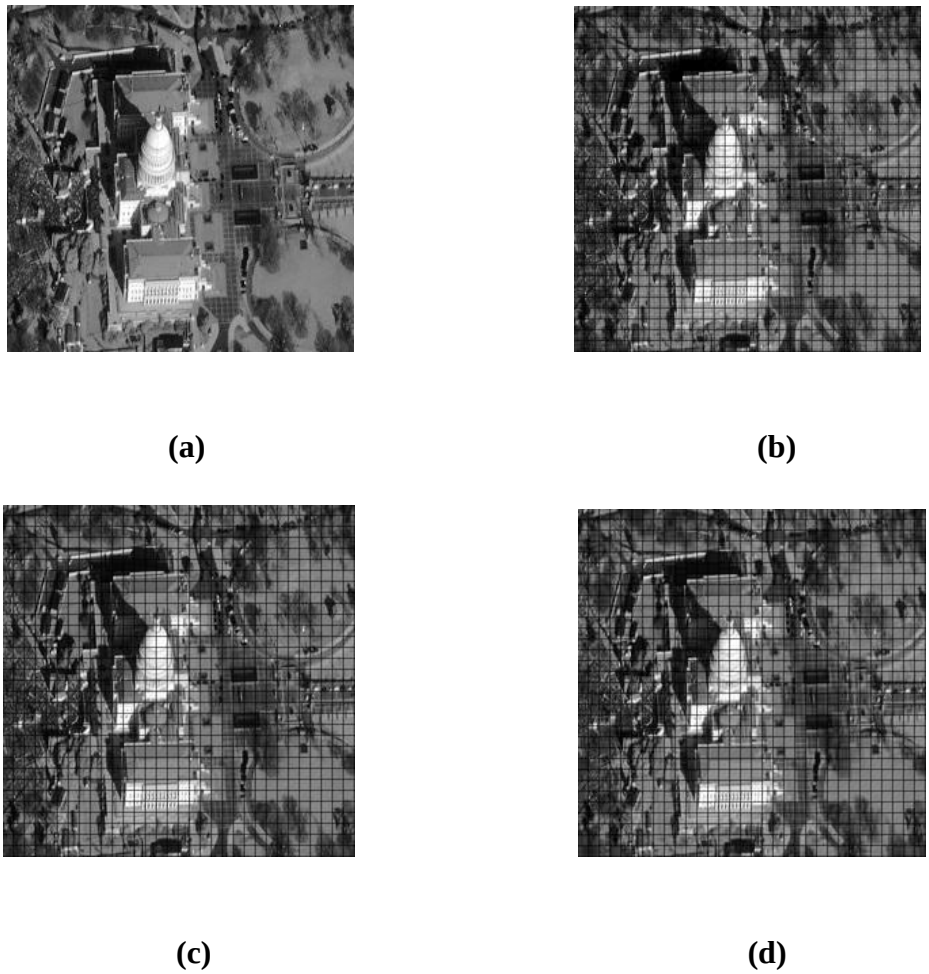

(a) **(b)**

(c) **(d)**

Figure 5.34 Satellite Image 3 at different value of fractional order (a) original images, (b) decompressed image at '0.5' fractional order, (c) decompressed image at optimum fractional order '0.97' and (d) decompressed image at fractional order '1'

At 50 % of Compression Ratio

Now at 50 % CR, if we compared the four satellite images shown in figure 5.35, then it is clear that figure 5.35 (c) is the best quality of decompressed image and having best results as at this fractional order the minimum MSE and maximum PSNR obtained.

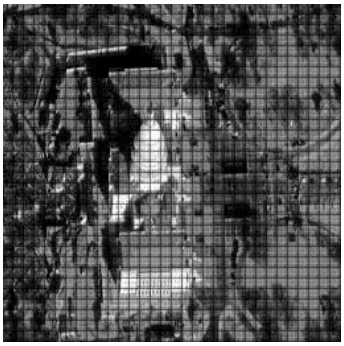

.

(a) **(b)**

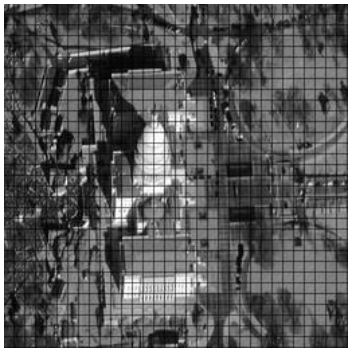

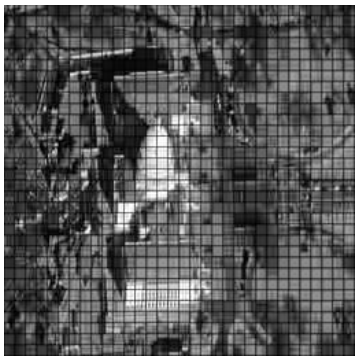

(c) **(d)**

Figure 5.35 Satellite Image 3 at different value of fractional order (a) original images, (b) decompressed image at '0.5' fractional order, (c) decompressed image at optimum fractional order '0.98' and (d) decompressed image at fractional order '1'

At 70 % Compression Ratio

The compression results of satellite image using discrete fractional Fourier transform are shown in figure 5.36 at 70 % CR. The decompressed satellite images at different fractional order are shown in figure 5.36 (b), 5.36 (c) and 5.36 (d). Figure 5.36 (c) is satellite decompressed images having optimum fractional order.

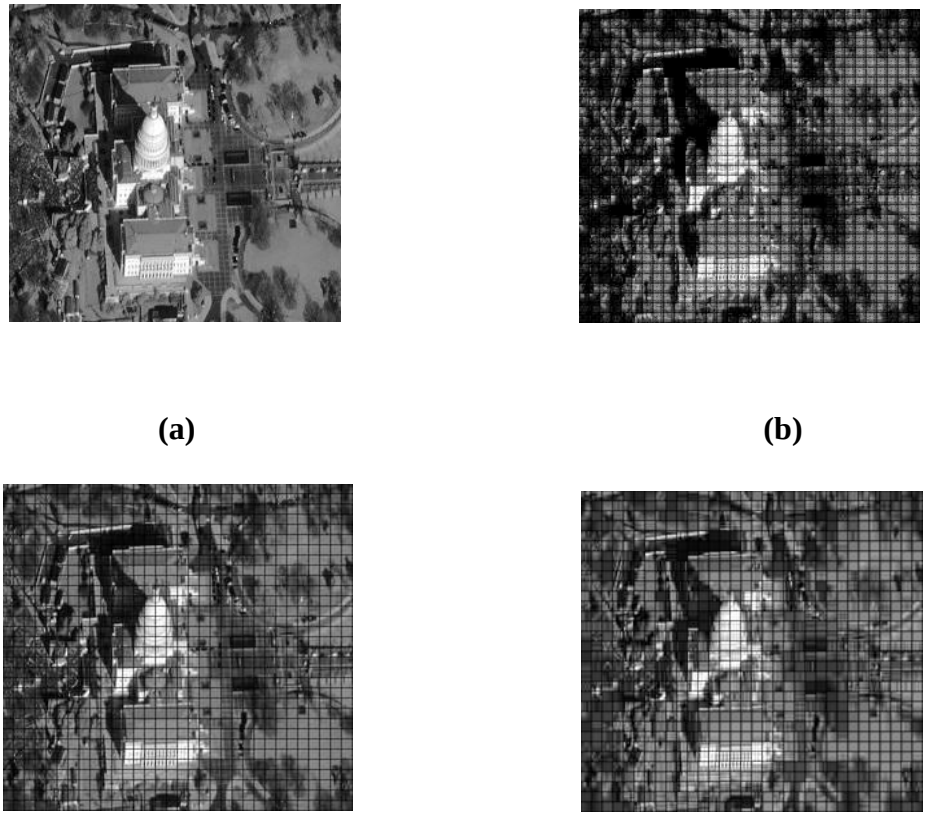

(a) **(b)**

(c) **(d)**

Figure 5.36 Satellite Image 3 at different value of fractional order (a) original images, (b) decompressed image at '0.5' fractional order, (c) decompressed image at optimum fractional order '0.95' and (d) decompressed image at fractional order '1

For satellite images, the at optimum fractional order a=0.97, 0.98 and 0.95 in which best result are achieved, for 30 %, 50% and 70% CR respectively. The decompressed images shown in figure 5.34(c) at 30% CR, in figure 5.35 (c) at 50% CR and in figure 5.36 (c) at 70% CR. The corresponding MSE and PSNR are shown in table 5.10.

Table 5.7 Result of Satellite image compression using DFrCT of Image 3 at different CR%

Fractional Order(a)	PSNR 10%	MSE 10%	PSNR 30%	MSE 30%	PSNR 50%	MSE 50%	PSNR 70%	MSE 70%
0.1	16.46	1469.19	15.31	1914.61	13.41	2965.38	11.55	4550.72
0.2	16.91	1324.58	16.11	1592.50	14.57	2270.28	11.57	4529.81
0.3	17.11	1264.97	17.59	1132.60	16.17	1570.65	12.47	3681.97
0.4	18.78	861.153	18.00	1030.57	16.99	1300.41	13.43	2951.75
0.5	19.3705	751.675	18.74	869.121	17.06	1279.61	15.22	1954.70
0.6	19.39	748.307	18.88	841.550	18.10	1007.11	15.36	1892.69
0.7	19.44	739.742	19.02	814.855	18.22	979.671	15.78	1718.22
0.8	19.51	727.914	19.22	778.180	19.22	778.180	17.18	1244.74
0.9	19.57	717.927	19.54	722.903	19.45	738.040	19.14	792.647
0.91	19.61	711.345	19.57	717.927	19.5	729.592	19.20	781.772
0.92	19.64	706.448	19.65	704.823	19.61	711.345	19.22	778.180
0.93	19.66	703.202	19.7	696.755	19.65	704.823	19.33	758.717
0.94	19.68	699.971	19.71	695.152	19.66	703.202	19.44	739.742
0.95	19.71	695.152	19.72	693.554	19.67	701.585	19.56	719.582
0.96	19.73	691.958	19.77	685.615	19.64	706.448	19.66	703.202
0.97	19.74	690.367	19.72	693.554	19.61	711.345	19.57	717.927
0.98	19.72	693.554	19.71	695.152	19.60	712.984	19.55	721.240
0.99	19.68	699.971	19.65	704.823	19.59	714.628	19.48	732.960
1	19.63	708.076	19.62	709.709	19.58	716.275	19.42	742.694

5.4.4 Result of satellite image 4 of 256×256 Size

Image 4 is satellite image of 256×256 pixel size. Figure 5.37 shows the variation of PSNR with fractional order atdifferent CR. Figure 5.38 shows the variation of PSNR with fractional order at different CR.

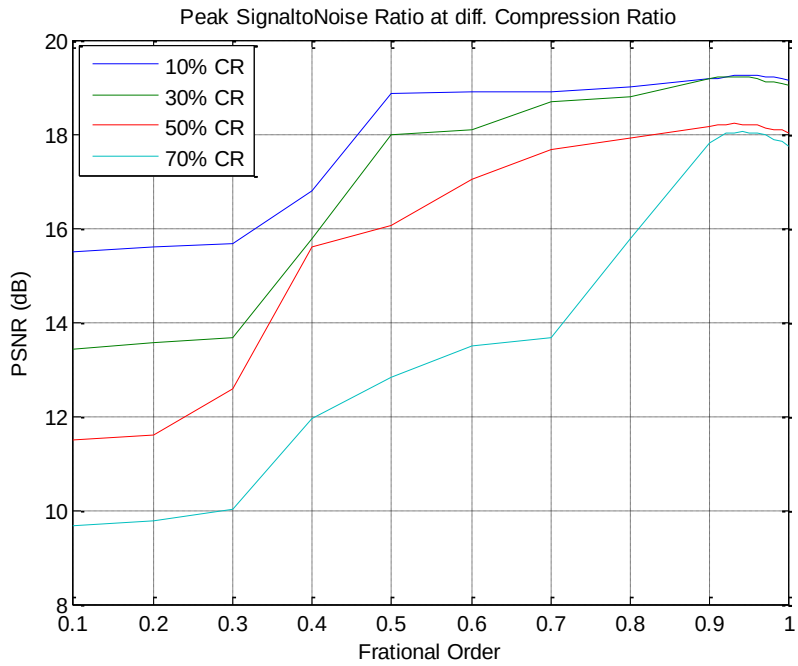

Figure 5.37 PSNR versus fractional order at different CR

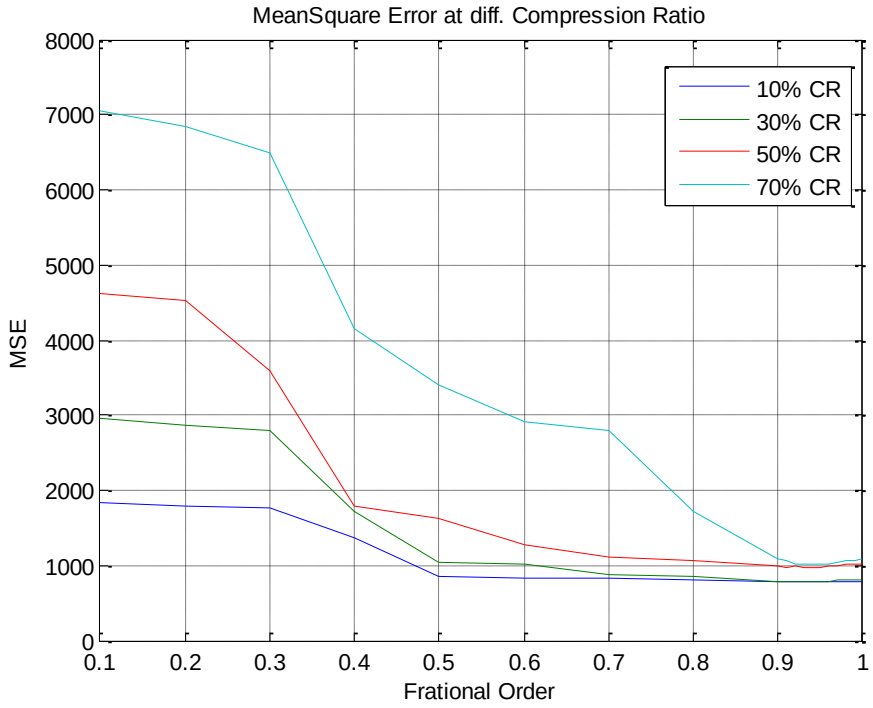

Figure 5.38 MSE versus fractional order at different CR

Table 5.8 Result of Satellite image compression using DFrCT of Image 4 at different CR%

Fractional Order(a)	PSNR 10%	MSE 10%	PSNR 30%	MSE 30%	PSNR 50%	MSE 50%	PSNR 70%	MSE 70%
0.1	15.48	1841.11	13.41	2965.38	11.49	4614.02	9.65	7048.23
0.2	15.58	1799.20	13.56	2864.70	11.58	4519.39	9.78	6840.38
0.3	15.68	1758.24	13.68	2786.63	12.58	3589.88	10.01	6487.54
0.4	16.78	1364.83	15.78	1718.22	15.58	1799.20	11.95	4150.30
0.5	18.8510	847.189	17.98	1035.33	16.044	1616.88	12.81	3404.71
0.6	18.9	837.684	18.09	1009.43	17.05	1282.56	13.5	2904.56
0.7	18.91	835.757	18.68	881.211	17.68	1109.38	13.68	2786.63
0.8	19.01	816.733	18.78	861.153	17.9	1054.58	15.78	1718.22
0.9	19.1732	786.611	19.166	787.916	18.166	991.928	17.81	1076.66
0.91	19.18	785.380	19.21	779.974	18.21	981.929	17.90	1054.58
0.92	19.20	781.772	19.2	781.772	18.2	984.193	18.01	1028.20
0.93	19.234	775.676	19.22	778.180	18.22	979.671	18.02	1025.84
0.94	19.233	775.854	19.21	779.974	18.21	981.929	18.04	1021.12
0.95	19.232	776.033	19.21	779.974	18.21	981.929	18.02	1025.84
0.96	19.23	776.390	19.18	785.394	18.18	988.736	18.01	1028.20
0.97	19.21	779.974	19.12	796.306	18.12	1002.49	17.98	1035.33
0.98	19.2	781.772	19.10	799.982	18.10	1007.11	17.88	1059.44
0.99	19.18	785.380	19.08	803.674	18.08	1011.76	17.85	1066.79
1	19.14	792.647	19.02	814.855	18.02	1025.84	17.746	1092.03

5.5 COMPARATIVE ANALYSIS OF DFrFT AND DFrCT

The comparative analysis of DFrFT and DFrCT are shown in table 5.1 and table 5.2. These tables are constructed according to the optimum value of fractional order ‘a’ in which the best result are obtained at different CR. The performace of the DFrFT is much better than the performance of DFrCT as shown in table 5.9 and table 5.10.

Table 5.9 Results at optimum fractional order with different CR using DFrFT

	Image 1 (512X512)			Image 2 (512X512)			Image 3 (256X256)			Image4 (256X256)		
CR%	**a_{opt}**	**PSNR**	**MSE**	**a_{opt}**	**PSNR**	**MSE**	**a_{opt}**	**PSNR**	**MSE**	**a_{opt}**	**PSNR**	**MSE**
10%	0.8	63.42	0.0295	0.8	64.33	0.0245	0.7	66.06	0.00892	0.7	67.89	0.0160
20%	0.88	53.66	0.2796	0.8	55.38	0.1883	0.9	56.17	0.1531	0.7	51.74	0.4301
30%	0.9	47.71	1.1012	0.8	49.81	0.6783	0.9	50.38	0.5761	0.9	45.88	1.6771
40%	0.88	43.47	2.9221	0.8	45.42	1.8641	0.9	46.09	1.6132	0.9	41.52	4.5775
50%	0.86	40.15	6.2712	0.8	41.83	4.2625	0.92	42.33	3.8962	0.91	37.83	10.5701
70%	0.74	38.85	8.4764	0.9	35.93	16.5667	0.91	36.78	13.6421	0.93	38.02	10.2504

Table5.10 Result at optimum fractional order with different CR using DFrCT

	Image 1 (512X512)			Image 2 (512X512)			Image 3 (256X256)			Image4 (256X256)		
CR%	**a_{opt}**	**PSNR**	**MSE**	**a_{opt}**	**PSNR**	**MSE**	**a_{opt}**	**PSNR**	**MSE**	**a_{opt}**	**PSNR**	**MSE**
10%	0.99	20.806	540.10	0.96	23.61	282.540	0.97	19.74	690.367	0.94	19.82	677.766
20%	0.95	20.793	541.72	0.98	23.53	288.456	0.95	19.81	679.32	0.96	19.65	704.8235
30%	0.98	20.799	540.97	0.95	23.40	297.221	0.96	19.77	685.615	0.93	19.32	760.467
40%	0.94	20.781	543.22	0.93	23.36	299.971	0.94	19.69	698.36	0.97	19.02	814.855
50%	0.97	20.764	545.30	0.97	23.22	309.799	0.95	19.67	701.5	0.95	18.21	981.92
70%	0.96	20.612	565.04	0.96	23.01	325.14	0.96	19.66	703.2	0.94	18.04	1021.211

5.6 SUMMARY

It is summarized that the two fractional transforms DFrFT and DFrCT have been used for compression in satellite images. PSNR and MSE have been used as parameters to evaluate the performance of these transforms. Different satellite images have been selected to obtain the generalized results. Satellite image compression has been performed for different CRs and the value of optimum *'a'* that provided best compression results for different CRs has been recorded. It is clear that for all images a $\in$[0.8-1) is an optimum domain for which better-decompressed image is retained with better PSNR. Performance of DFrFT is observed to be better than DFrCT for image compression.

CHAPTER-6

SATELLITE IMAGE ENCRYPTION USING DISCRETE FRACTIONAL TRANSFORMS

6.1INTRODUCTION

With rapid growth in the new generation satellite and internet technologies, the satellite system can provide extremely more secure communication as the satellite imagery data transmission and distribution over the shared network such as (Internet, LAN, WAN, etc.). The major issue for shared network is to prevent the important satellite imagery information from being disclosed to illegal users. Thus, satellite industry is constantly striving to make their communications more secure than ever. So, it is important to provide high security to unauthorized access to sensitive satellite data. For this reason the Satellite image encryption techniques are introduced. Most encryption techniques have been proposed recently and used in the field of information security [5], [40], [61]. It has been noticed that FRFT widely used in the field of image processing. The significant feature of discrete fractional Fourier domain in image encryption benefits from its extra degree of freedom that is provided by its fractional orders.

6.2 FRACTIONAL TRANSFORM BASED MODEL OF ENCRYPTION

In this encryption process cascaded multistage fractional transform has been utilized. The n-stage of fractional transform can provide n-dimensional extra keys indicated by the fractional orders. In case of two-dimensional fractional transform transform, there are two different fractional orders along x-axis and y-axis respectively. The n-stage of fractional transform has total encryption keys can be increased to as many as 3n-1. Thus the security strength of the encryption keys may be greatly enhanced. For simplicity, the order α along x and y direction are taken to be same i.e. $\alpha_x = \alpha_y = \alpha$ and in this encryption scheme, three stages of fractional transform are cascaded together. Algorithm consists of two parts, encryption to encrypt image and decryption to retrieve image. The satellite image encryption and decryption model using DFrFT and DFrCT are shown in figure 1. If $f(x_0,y_0)$, a real value data

two-dimensional data, denote the image that is to be encrypted. Fractional transform is applied continuously three time with the fractional order of α_1, α_2 and α_3, respectively.

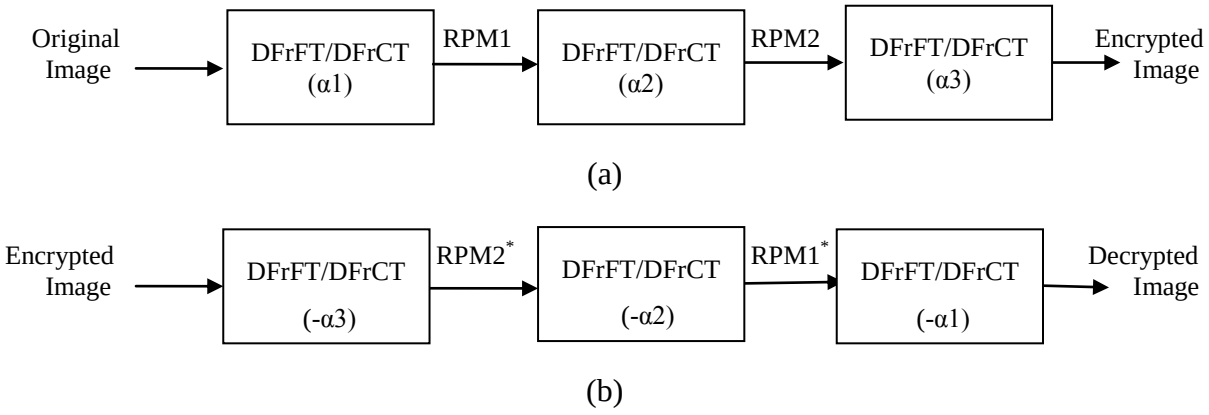

Figure 6.1 Satellite Image Encryption Model (a) Encoder (b) Decoder

Thus the resultant transformed function $\psi(x,y)$ can be written as

$$\psi(x,y)=F^{\alpha 3}[\psi_2(x_2,y_2)*RPM2]$$

with $$\psi_2(x_2,y_2)=F^{\alpha 2}[\psi_1(x_1,y_1)*RPM1]$$

and $$\psi 1(x_1,y_1)=F^{\alpha 1}[f(x_0,y_0)]$$

where RPM1and RPM2 are the random phase masks.

the resultant transform function $\psi(x,y)$ can be regarded as the encrypted image. The decrypted process is the reverse operation with respect to the encryption. Firstly, we take the fractional transform of order $-\alpha_3$ on the encrypted image $\psi(x,y)$.The midterm function $\psi 2(x_2,y_2)$ is obtained by convolving the conjugate of RPM2. Then by performing fractional transform of order of α_2 on function $\psi 2(x_2,y_2)$, function $\psi 1(x,y)$ is recovered. After another fractional transform of order α_1 on the function $\psi 1(x_1,y_1)$ and convolving with conjugate of RPM1, the original $f(x_0,y_0)$ is obtained.

6.3 PARAMETERS USED IN SATELLITE IMAGE ENCRYPTION

The quality of decrypted image can be measured by many parameters. The most commonly used parameters are Mean square Error and Peak Signal to Noise Ratio. The PSNR can be defined as the difference between the decrypted image and its original image. The larger the

PSNR value, the better will be the decrypted image quality. The average of the square of the difference between the desired response and the actual system output (the error) or the mean square error is a measure of the differences between values predicted and the values actually observed. MSE and PSNR are defined as:

$$MSE = \frac{1}{MN} \sum_{i=0}^{M-1} \sum_{j=0}^{N-1} [\overline{f}(i, j) - f(i, j)]^2$$

$$PSNR = 10 \log_{10} \left[\frac{M \times N}{MSE} \right]$$

Where $M \times N$ the size of the images is, $\overline{f}(i, j)$ is the matrix elements of the decompressed and $f(i, j)$ is the matrix elements of the original images at (i, j) pixel.

6.4 SIMULATION RESULTS USING DFrFT

Result of four different satellite images using discrete fractional Fourier transform are presented as given below.

6.4.1 Result of satellite image 1 of 512×512 size

Image 1 is satellite image of 512×512 pixel size. The result of satellite image 1 is shown in figure 6.2. Figure 6.2 (a) is original image, figure 6.2 (b) shows the encrypted image with encrypted key (0.99, 0.9, 0.8), figure 6.2 (c) shows decrypted image with wrong key (0.7, 0.3, 0.6) and figure 6.2 (d) shows the decrypted image with correct encrypted keys. Figure 6.3 and figure 6.4 shows the deviation of MSE and PSNR using DFrFT with fractional order (key) keeping other two keys are correct respectively.

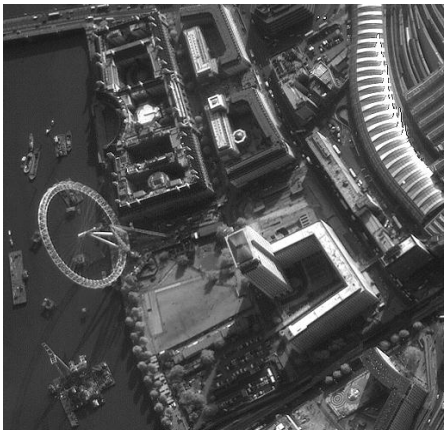

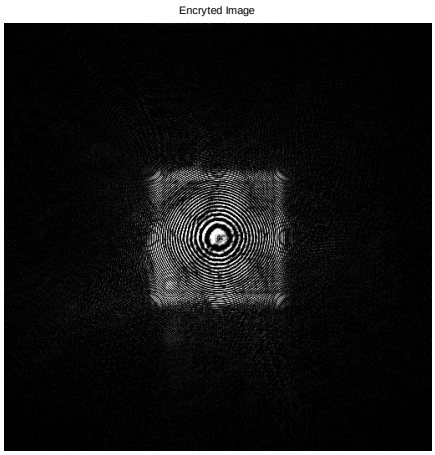

(a) **(b)**

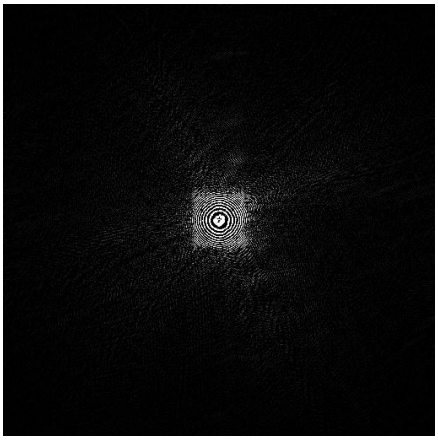

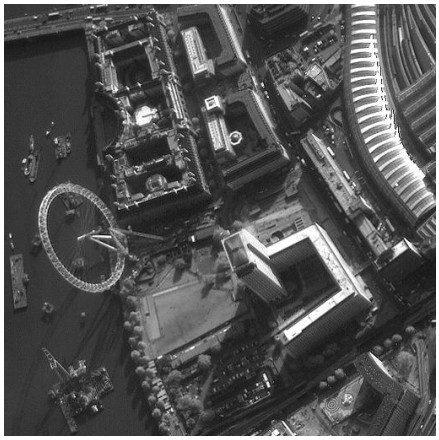

(c) **(d)**

Figure 6.2 Encryption of satellite image 1(a) Original Image of 512x512 size , (b) Encrypted Image having key (0.99, 0.9, 0.8), (c) Decrypted Image with wrong keys and (d) Decrypted Image with right key

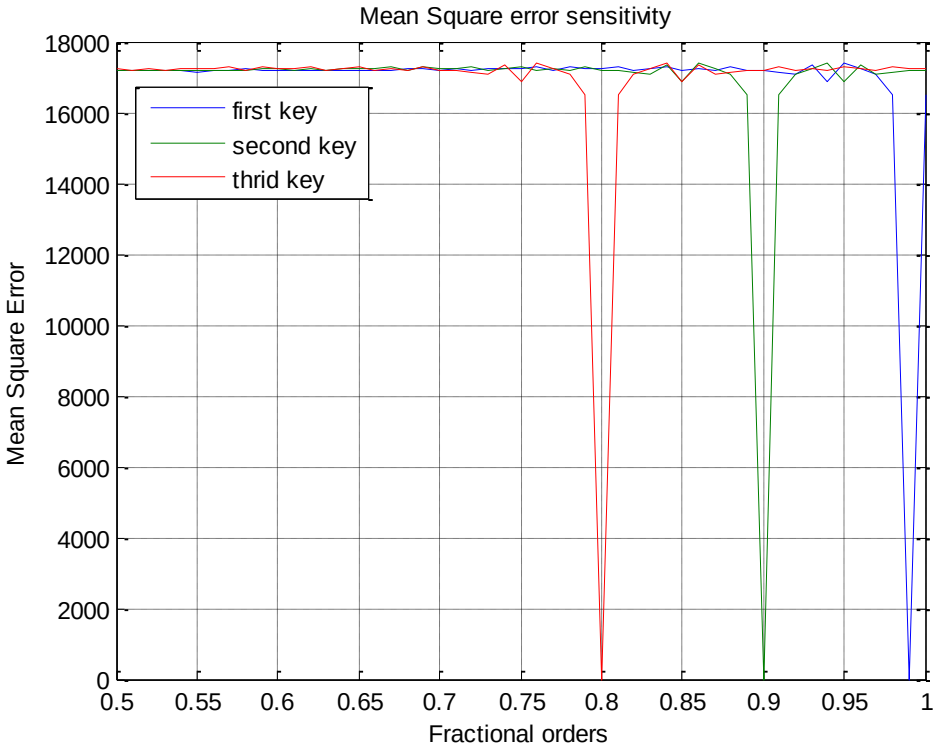

Figure 6.3 Deviation of MSE with fractional order keeping two keys correct of three keys

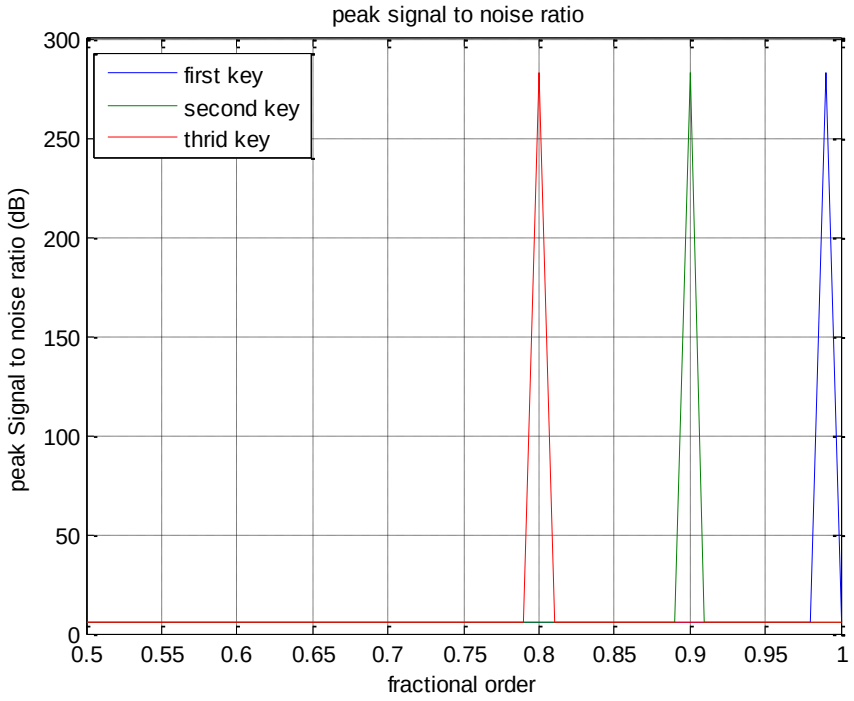

Figure 6.4 Deviation of PSNR with fractional order keeping two keys correct of three keys

6.4.2 Result of satellite image 2 of 512×512 size

The size of Satellite Image 2 is 512×512 pixel. Figure 6.5 (a) is original image , figure 6.5 (b) shows the encrypted image with encrypted key (0.96, 0.84, 0.7), figure 6.5 (c) shows decrypted image with wrong key and figure 6.5 (d) shows the decrypted image with correct encrypted keys. Figure 6.6 and figure 6.7 shows the deviation of MSE and PSNR using DFrFT with fractional order (key) keeping other two keys are correct respectively.

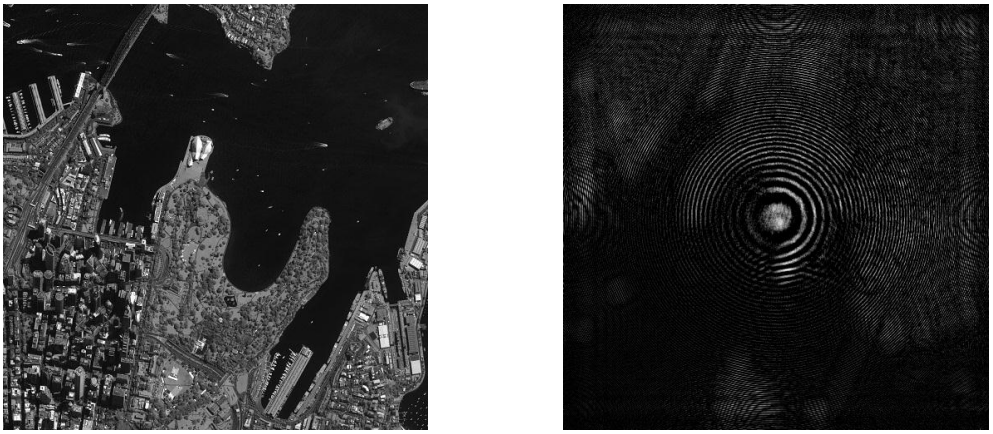

(a) **(b)**

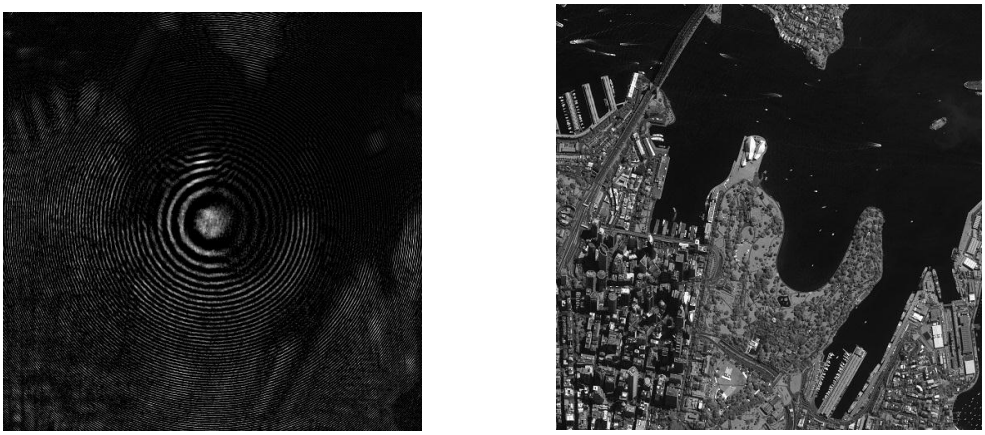

(c) **(d)**

Figure 6.5 Encryption of satellite image 2, (a) Original Image, (b) encrypted image with keys (0.96, 0.84, 0.7), (c) decrypted image with wrong keys and (d) decrypted image with right keys

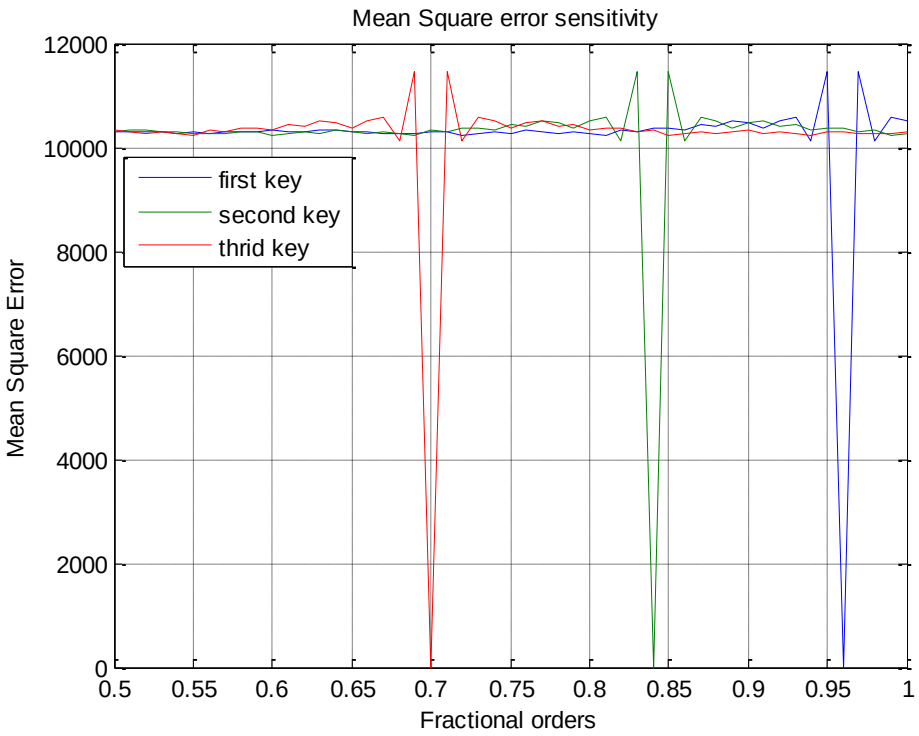

Figure 6.6 Deviation of MSE with fractional order keeping two keys correct of three keys

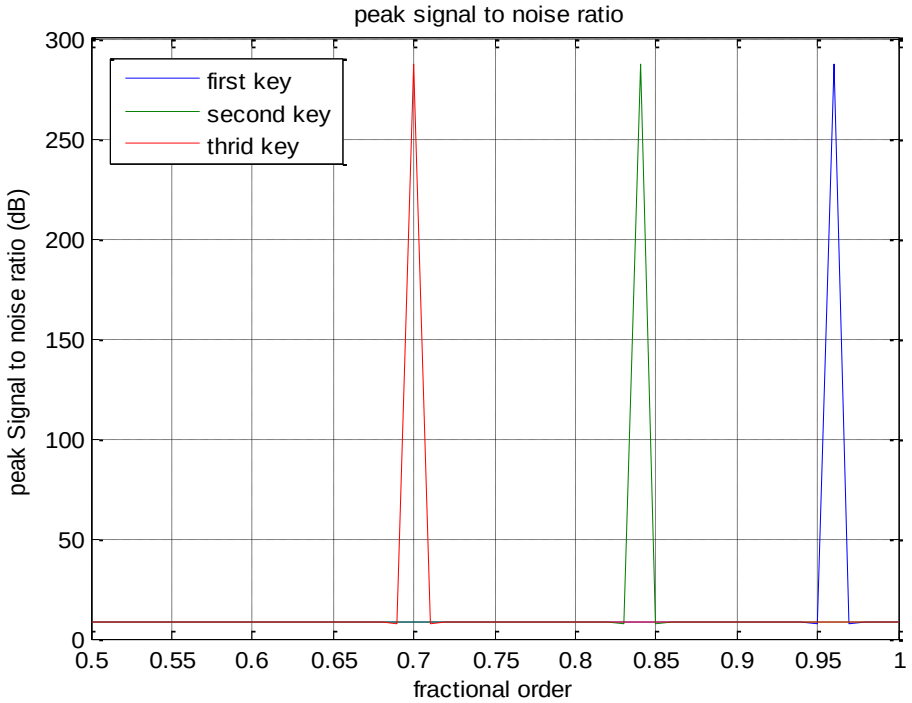

Figure 6.7 Deviation of PSNR with fractional order keeping two keys correct of three keys

6.4.3 Result of satellite image 3 of 512×512 size

Satellite image 3 is of 512×512 pixel size. Figure 6.9 shows the deviation of MSE and figure 6.10 shows deviation of PSNR using DFrFT with fractional order (key) keeping other two keys are correct. Original image is shown in figure 6.8 (a), figure 6.8 (b) shows the encrypted image with encrypted key (0.9, 0.96, 0.7), figure 6.8 (c) shows decrypted image with wrong key and figure 6.8 (d) shows the decrypted image with correct encrypted keys.

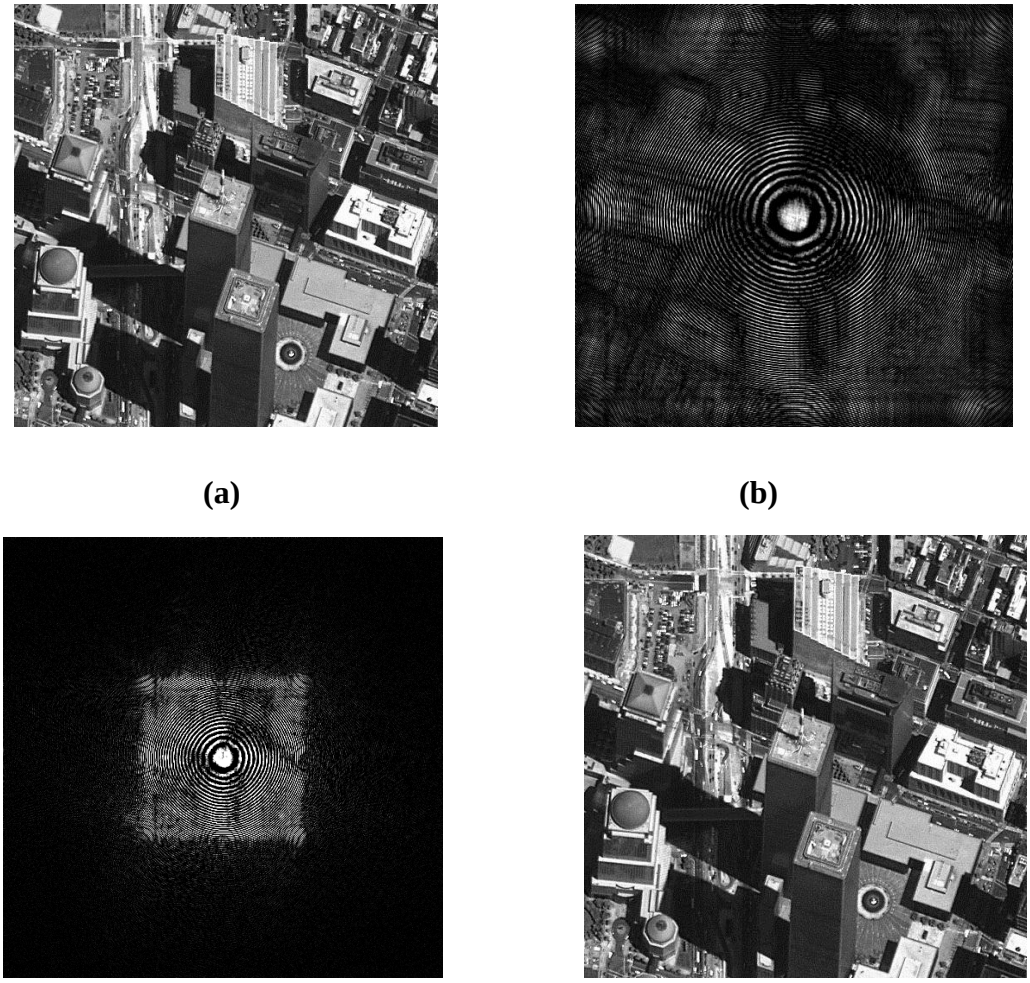

(a) **(b)**

(c) **(d)**

Figure 6.8 Encryption of satellite image 3, (a) Original Image 512x512 size, (b) Encrypted Image having keys (0.9, 0.96, 0.7), (c) Decrypted Image with wrong keys and (d) Decrypted Image with right key

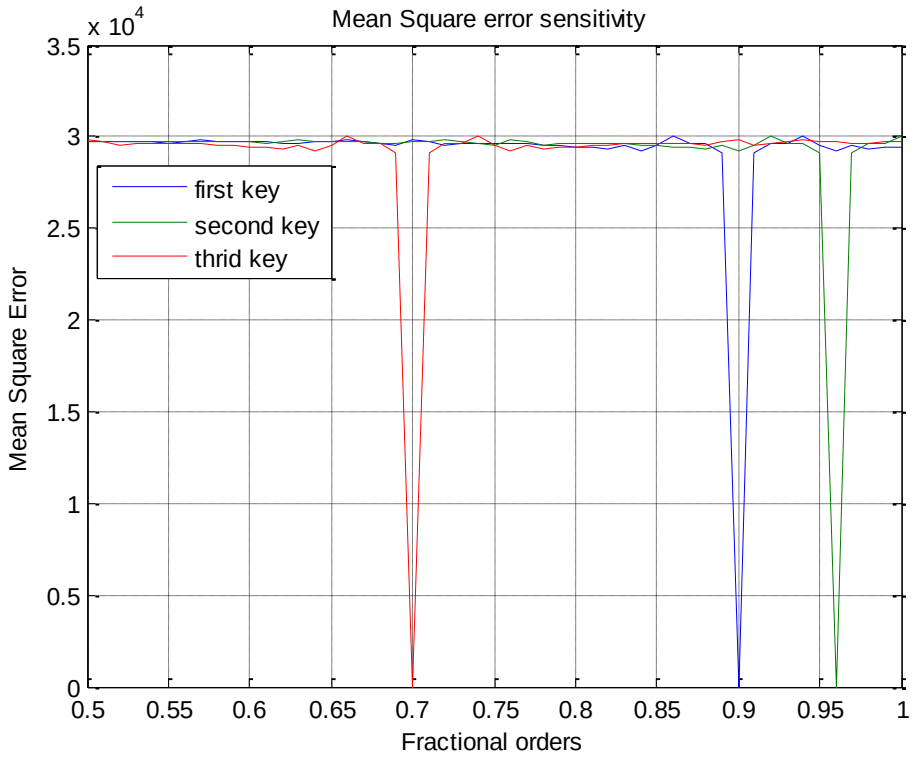

Figure 6.9 Deviation of MSE with fractional order keeping two keys correct of three keys

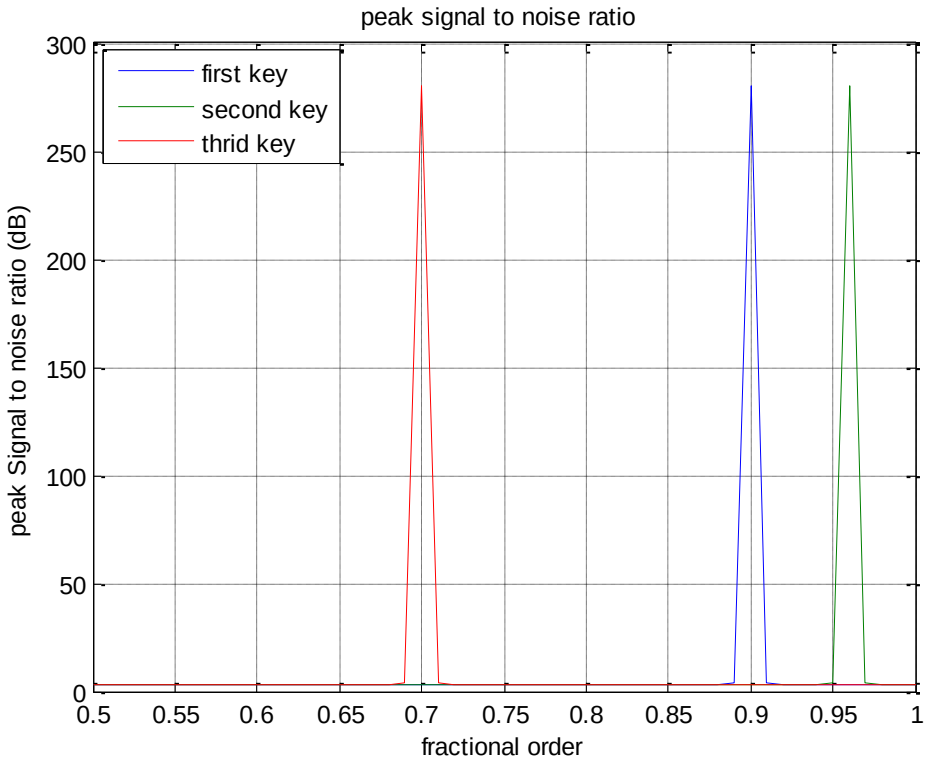

Figure 6.10 Deviation of PSNR with fractional order keeping two keys correct of three key

6.4.4 Result of satellite image 4 of 256×256 size

The result of satellite image encryption on satellite image 2 is shown in figure 6.11. Figure 6.11 (a) is original image, the encrypted image with encrypted key (0.99, 0.34, 0.8) in figure 6.11 (b), figure 6.11 (c) shows decrypted image with wrong keys and figure 6.11 (d) shows the decrypted image with correct encrypted keys. Figure 6.12 and figure 6.13 shows the deviation of MSE and PSNR using DFrFT with fractional order (key) keeping other two keys are correct respectively.

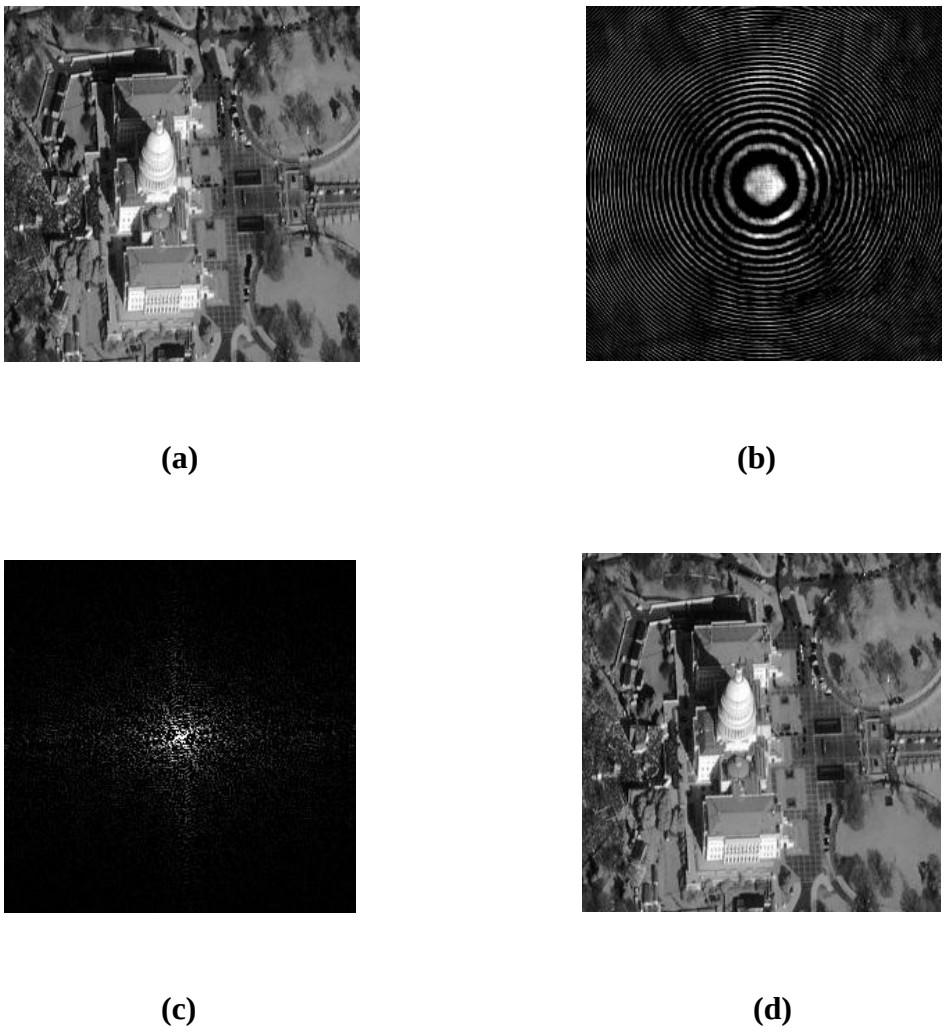

(a) **(b)**

(c) **(d)**

Figure 6.11 Encryption of satellite image 4, (a) Original Image 256x256 size, (b) Encrypted Image having keys (0.99, 0.34, 0.8), (c) Decrypted Image with wrong keys and (d) Decrypted Image with right key

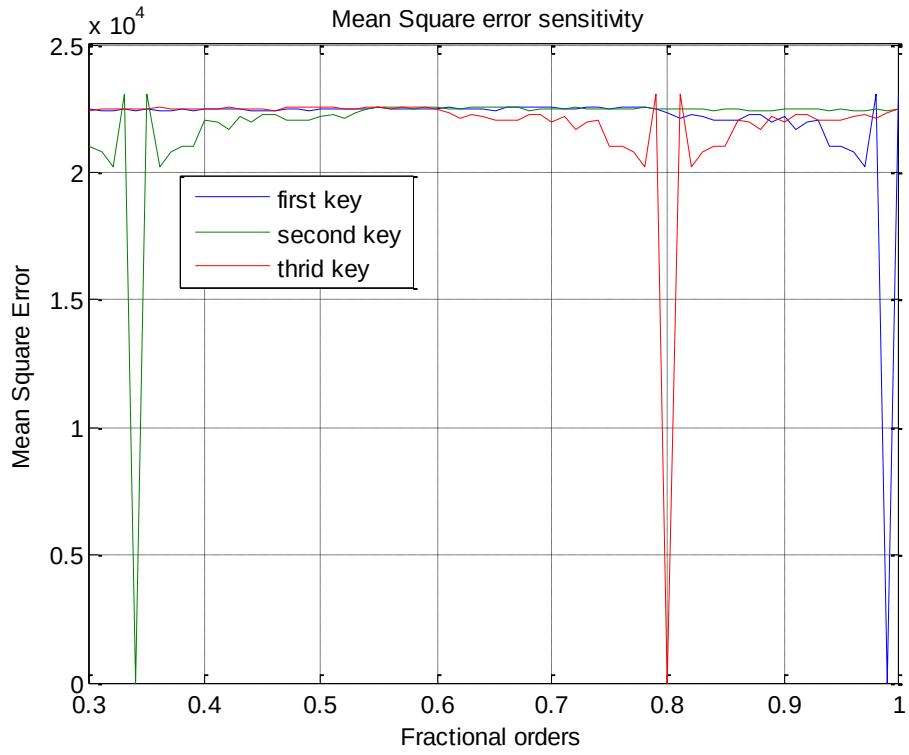

Figure 6.12 Deviation of MSE with fractional order keeping two keys correct of three keys

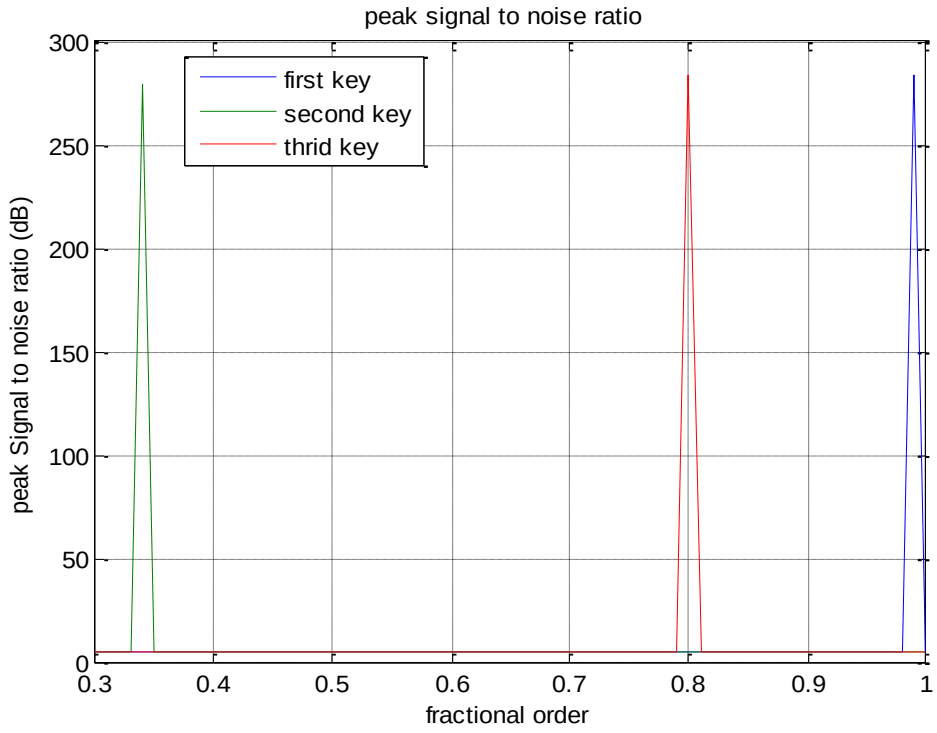

Figure 6.13 Deviation of PSNR with fractional order keeping two keys correct of three keys

6.5 SIMULATION RESULTS USING DFrCT

Result of satellite image encryption on four different satellite images using discrete fractional Cosine transform are presented as given below.

6.5.1 Result of satellite image 1 of 512×512 size

Using DFrCT, the result of satellite image encryption on satellite image 1 is shown in figure 6.14. Four images are shown out of which figure 6.14 (a) is original image, figure 6.14 (b) is the encrypted image with encrypted key (0.99, 0.89, 0.67), figure 6.14 (c) is decrypted image with wrong key and figure 6.14 (d) is the decrypted image with correct encrypted keys.

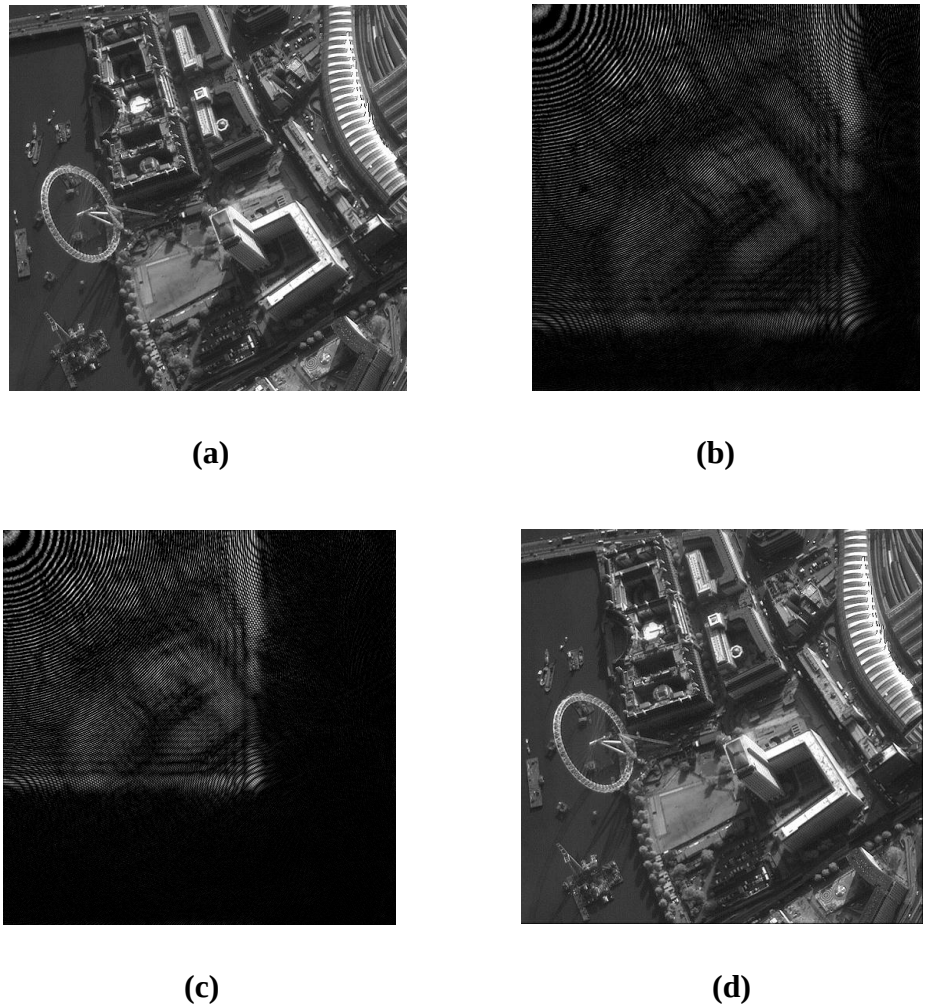

(a) **(b)**

(c) **(d)**

Figure 6.14 Encryption of satellite image 1, (a) Original Image 512x512 size, (b) Encrypted Image having keys (0.99,0.89,0.67), (c) Decrypted Image with wrong keys and (d) Decrypted Image with right key

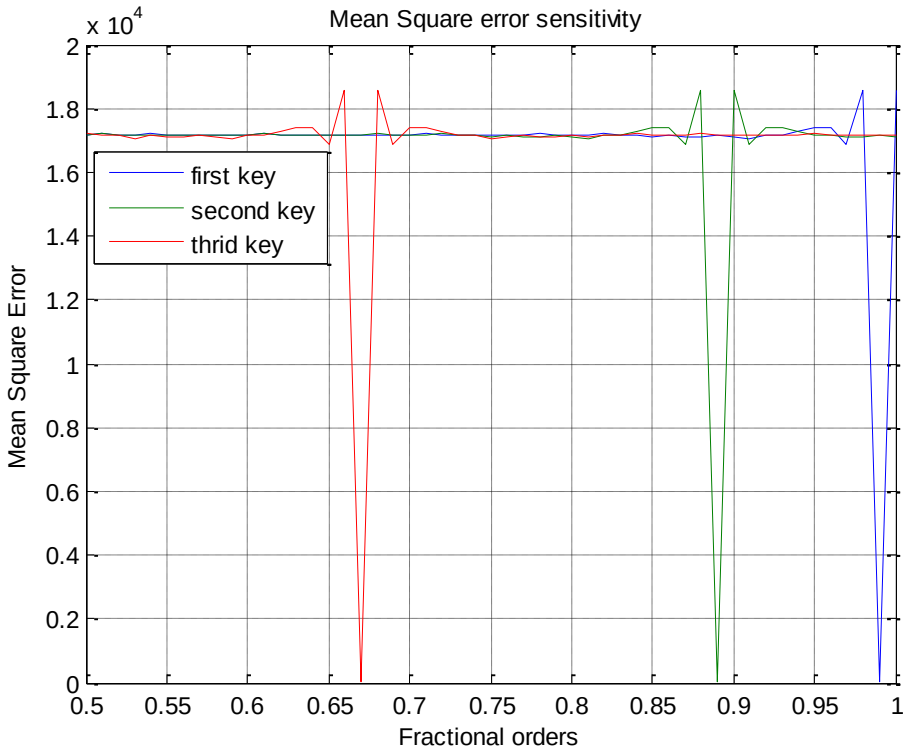

Figure 6.15 Deviation of MSE with fractional order keeping two keys correct of three keys

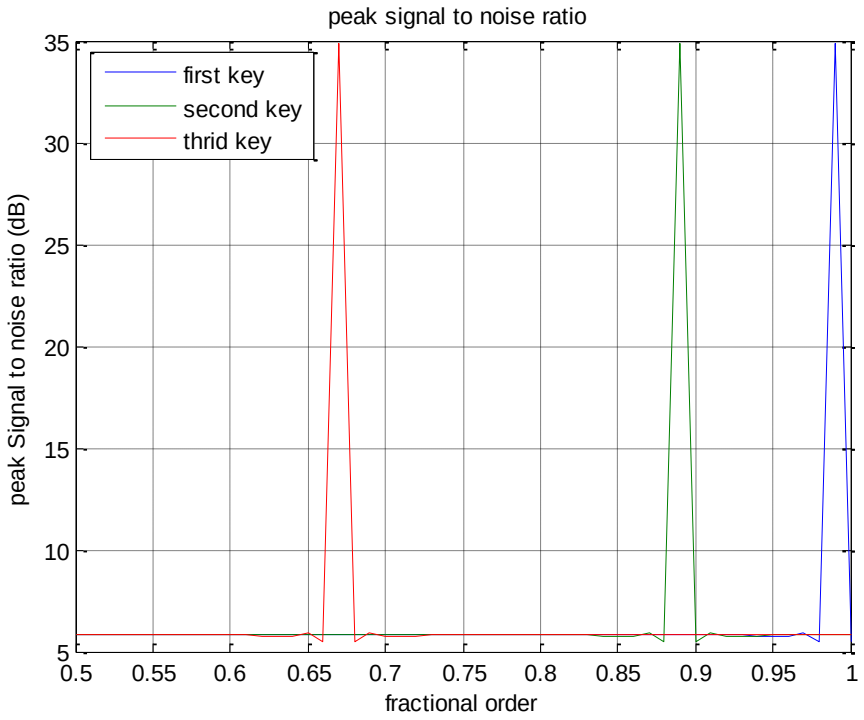

Figure 6.16 Deviation of PSNR with fractional order keeping two keys correct of three keys

6.5.1 Result of satellite image 2 of 512×512 size

Size of satellite image 2 is of 512×512. This image is encrypted using DFrCT and result is shown in figure 6.17. Figure 6.17 (a) is original image, figure 6.17 (b) shows the encrypted image with encrypted key (0.94, 0.89, 0.67), decrypted image with wrong key (0.5, 0.2, 0.6) is shown in figure 6.17 (c) and the decrypted image with correct encrypted keys is shown figure 6.17 (d). Figure 6.18 and figure 6.19 shows the deviation of MSE and PSNR using DFrFT with fractional order (key) keeping other two keys are correct respectively.

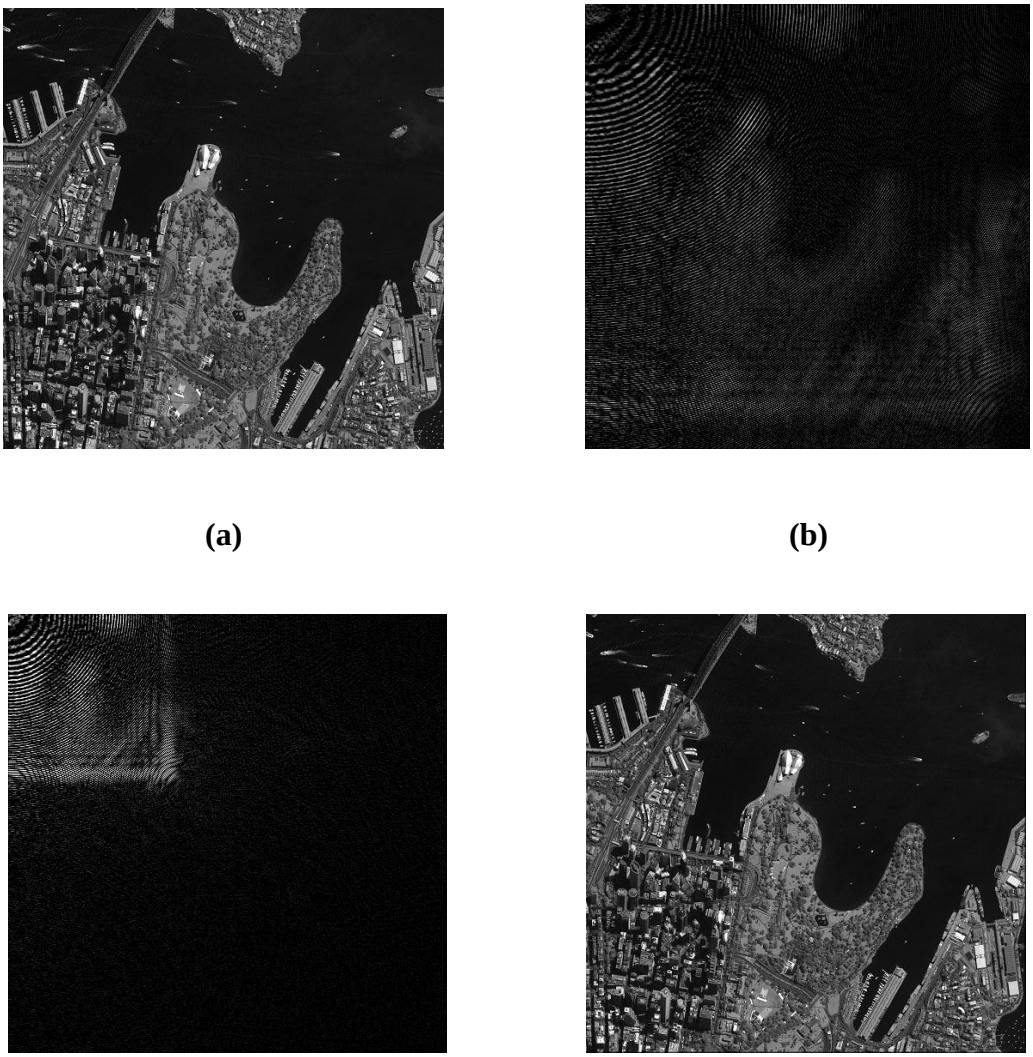

(a) **(b)**

(c) **(d)**

Figure 6.17 Encryption of satellite image 2, (a) Original Image (b) encrypted image with keys(0.94,0.89,0.67), (c) decrypted image with wrong keys (d) decrypted image with right keys

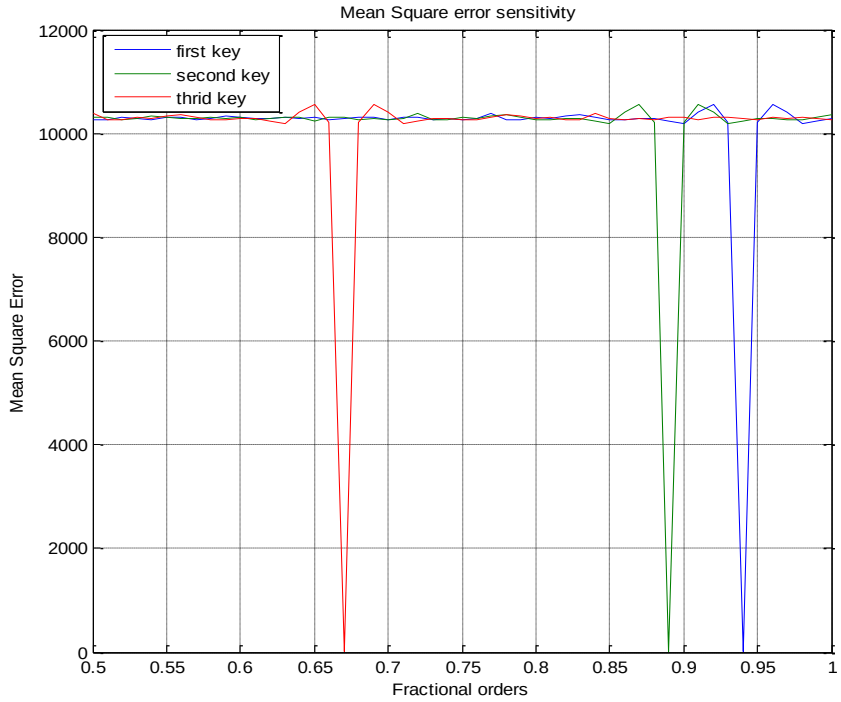

Figure 6.18 Deviation of MSE with fractional order keeping two keys correct of three keys

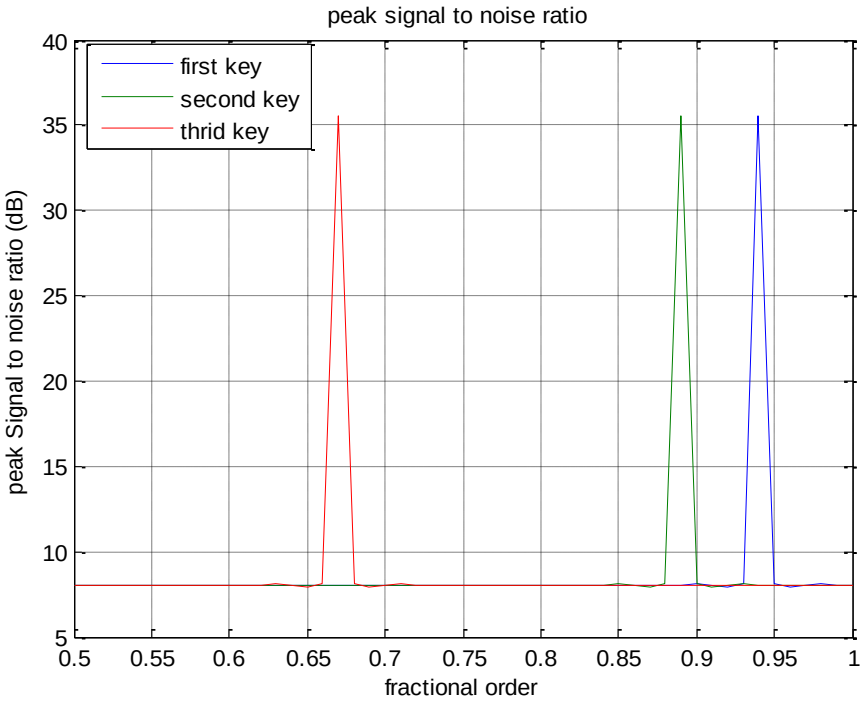

Figure 6.19 Deviation of PSNR with fractional order keeping two keys correct of three keys

6.5.3 Result of satellite image 3 of 512×512 size

The result of Satellite image encryption on satellite image 3 of size 512×512 is shown in figure 6.20. This image is encrypted with encrypted key (0.9, 0.89, 0.6) shown in figure 6.20(c). Figure 6.21 and figure 6.22 shows the deviation of MSE and PSNR using DFrFT with fractional order (key) keeping other two keys are correct respectively.

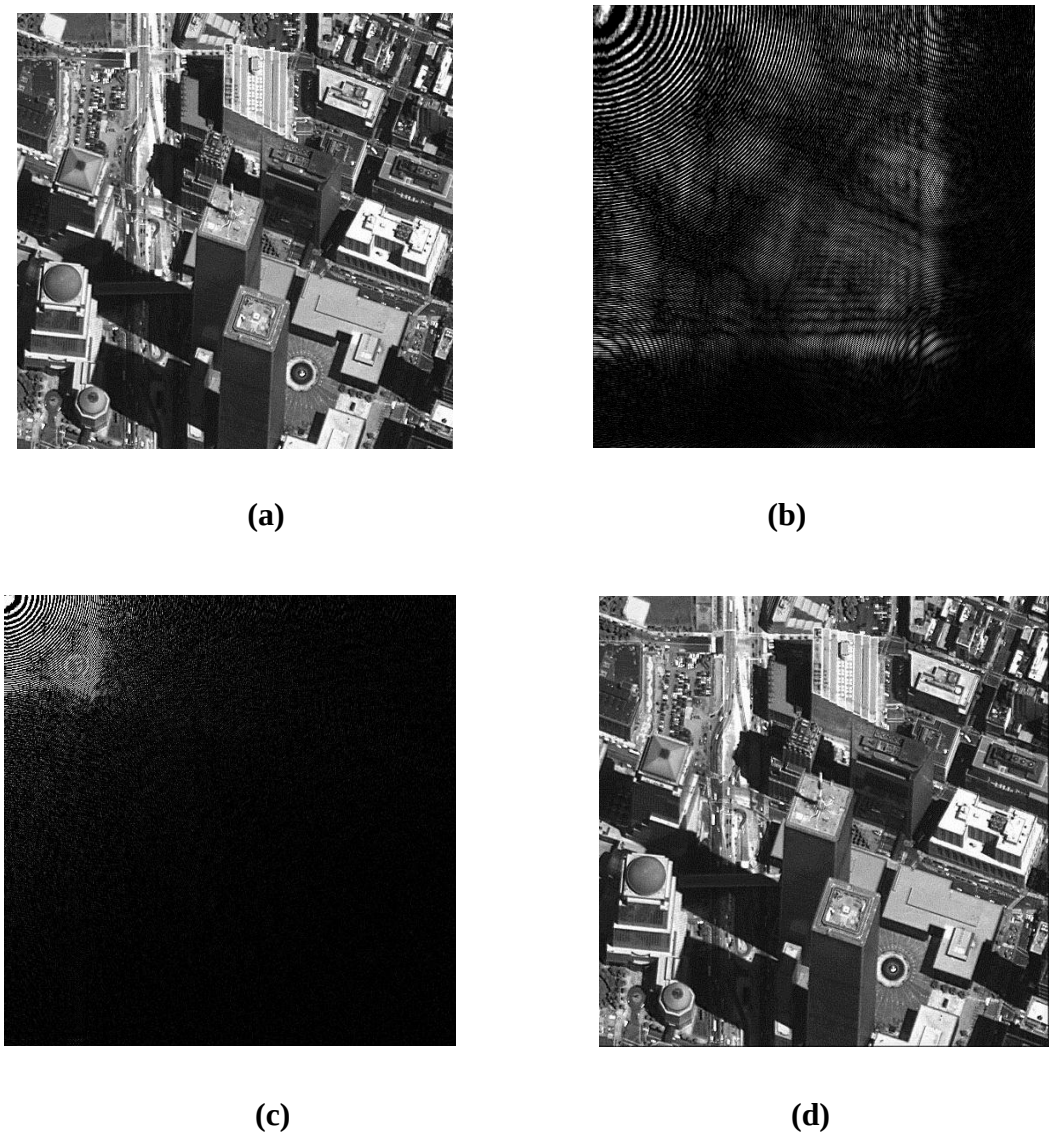

(a) **(b)**

(c) **(d)**

Figure 6.20 Encryption of satellite image 3 (a) Original Image 512x512 size, (b) Encrypted Image having keys (0.9, 0.89, 0.6), (c) Decrypted Image with wrong keys and (d) Decrypted Image with right key

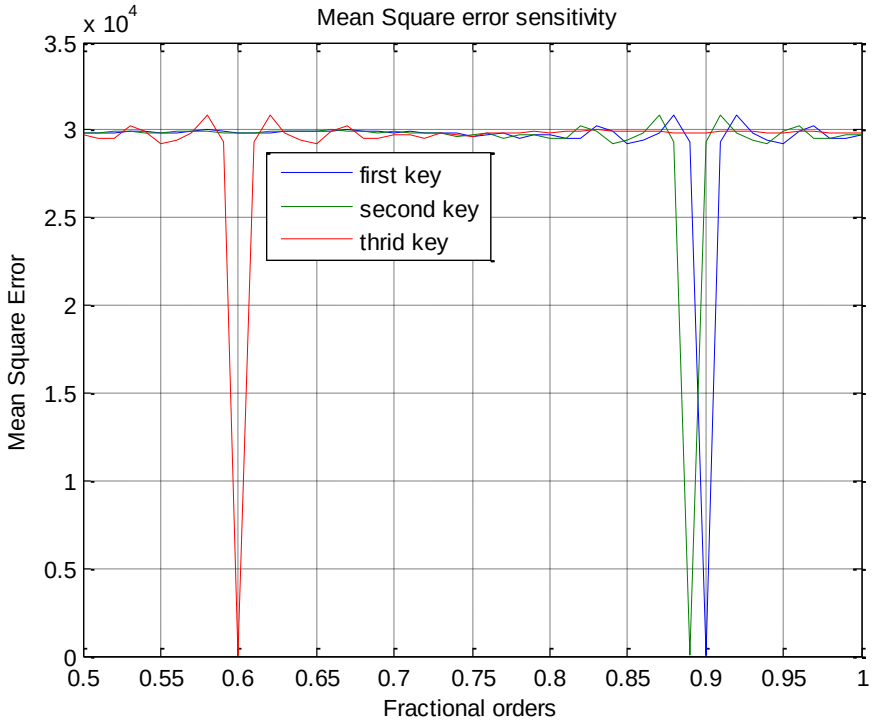

Figure 6.21 Deviation of MSE with fractional order keeping two keys correct of three keys

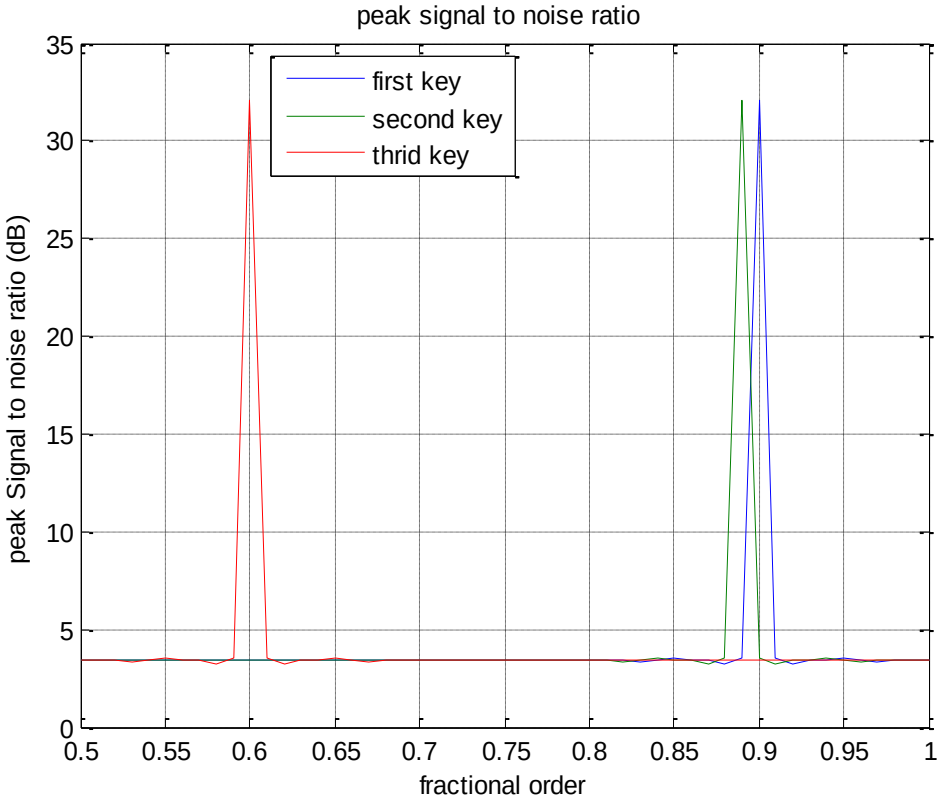

Figure 6.22 Deviation of PSNR with fractional order keeping two keys correct of three keys

6.5.4 Result of satellite image 4 of 256×256 size

Encryption result of satellite image 4 is shown in figure 6.23. Original image is shown in figure 6.23 (a), the encrypted image with encrypted key (0.88, 0.9, 0.68) is shown in figure 6.23 (b) and figure 6.23 (d) shows the decrypted image with correct encrypted keys. The deviation of MSE and PSNR using DFrFT with fractional order (key) keeping other two keys are correct plotted in figure 6.24 and figure 6.25 respectively.

(a)

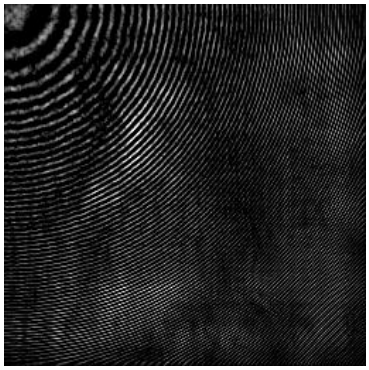

(b)

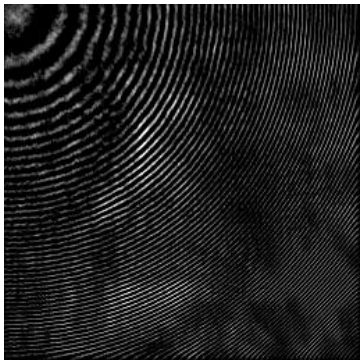

(c)

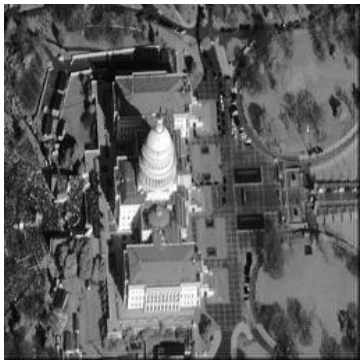

(d)

Figure 6.23 Encryption of satellite image 4 (a) Original Image 256×256 size, (b) Encrypted Image having keys (0.88, 0.9, 0.68), (c) Decrypted Image with wrong keys and (d) Decrypted Image with right key

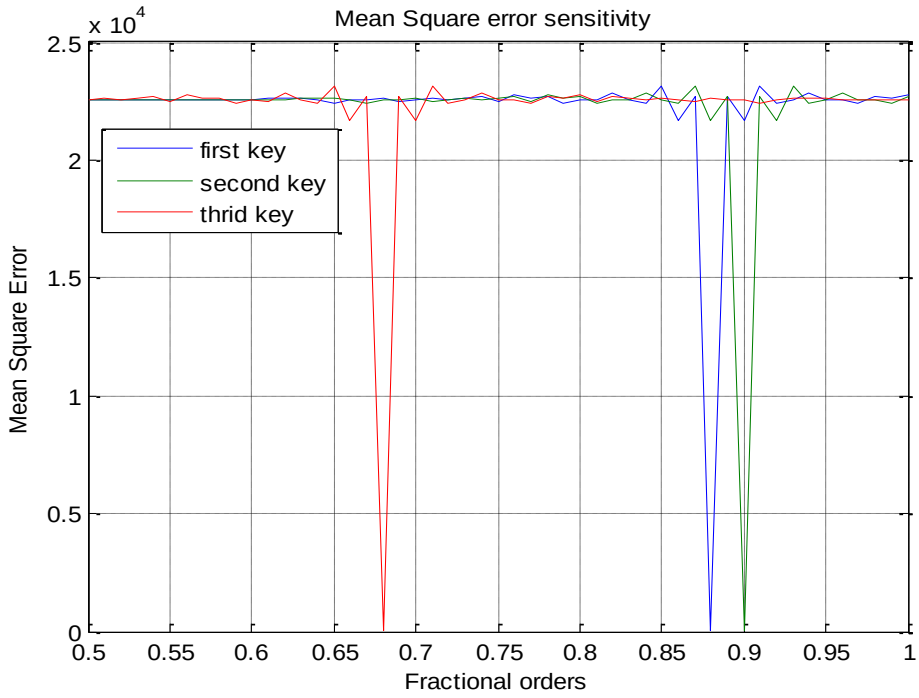

Figure 6.24 Deviation of MSE with fractional order keeping two keys correct out of three keys

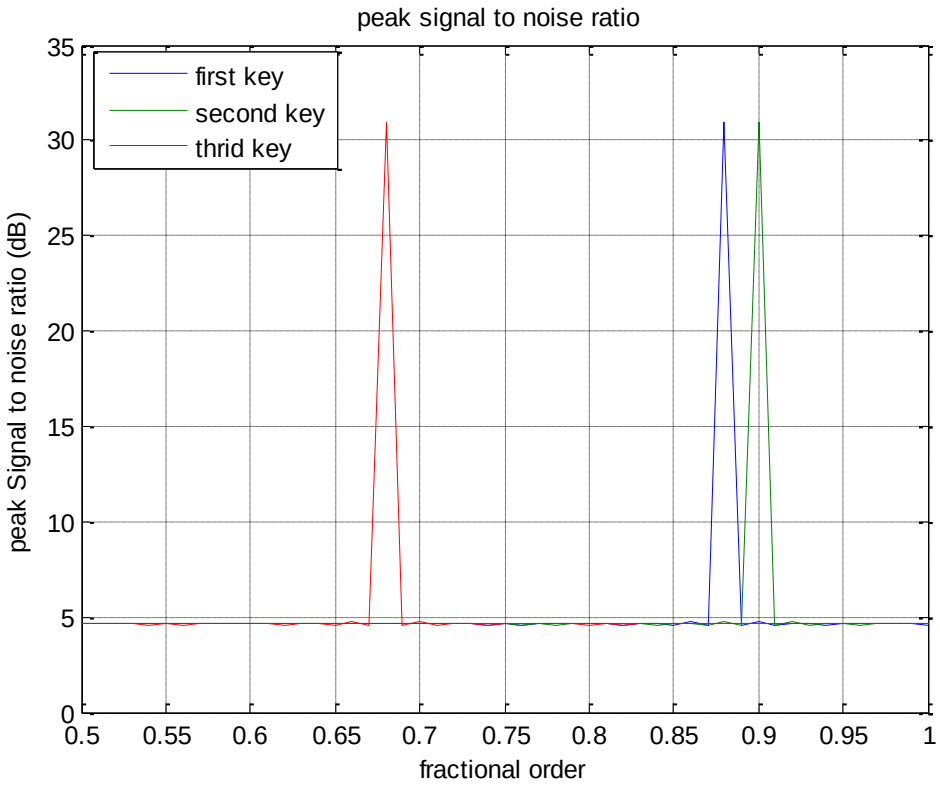

Figure 6.25 Deviation of PSNR with fractional order keeping two keys correct of three keys

6.6 COMPARISON OF PERFORMANCE OF DFRFT AND DFRCT

The comparison can be made on the basis of PSNR obtained. Comparing PSNR in the figure 6.3 with figure 6.19 of satellite image 1, it is observed that the PSNR by using DFrFT is much greater than that of using DFrCT. Similarly, the remaining three images can be compared**.**

6.7 SUMMARY

The multistage cascaded encryption algorithms using fractional transform is demonstrated for satellite image encryption, which provides extra key for encryption as extra degree of freedom available with fractional transforms. PSNR and MSE have been used as parameters to evaluate the performance of these transforms. The security strength is greatly enhanced by two factors namely multistage cascaded and extra degree of freedom provided by fractional transform. It is observed that the performance of DFrFT better than DFrCT as PSNR in case of DFrFT is more than DFrCT.

CHAPTER-7

CONCLUSION AND FUTURE SCOPE

7.1 CONCLUSION

This thesis describes the satellite image compression and encryption using discrete fractional transforms.

Firstly, the new generation satellites generate very high resolution images and these images require lager memory space for storing on satellite and large bandwidth requires to send these images on earth receiver. Image compression reduces the amount of data required to represent the image. The discrete fractional transforms like DFrFT and DFrCT are used for the compression of satellite images. It is observed that fractional transforms makes the full use of the additional degree of freedom provided by its fractional order 'a' to achieve an optimum domain for which compression is more, MSE is minimum and corresponding maximum PSNR and better-decompressed image is retained. The two fractional transforms, discrete fractional Fourier transform and discrete fractional Cosine transforms has been examined and the results are obtained as a function of the overall CR and PSNR. It is clear that for all satellite images a $\in$[0.8-1) is an optimum domain for which better-decompressed image is retained with better PSNR. It has been observed that DFrFT gives better compression in satellite image as compared to DFrCT.

Secondly, with the large-scale development in satellite and network communication technologies, there is inherent risk on satellite images from unauthorized access and illegal usage. The multistage cascaded encryption algorithms using fractional transforms are demonstrated for satellite image encryption, which provides extra key for encryption as extra degree of freedom available with fractional order 'a'. The security strength is greatly enhanced by using multistage cascaded encryption technique based on fractional transforms algorithms. The discrete fractional Fourier transform and discrete fractional Cosine transform are used as fractional transform. The performance of the DFrFT and DFrCT is compared based on PSNR. It is observed that the performance of DFrFT better than DFrCT in case of satellite image encryption.

7.2 FUTURE SCOPE

The suitability of various other fractional transforms like fractional Hartley transform, fractional Wavelet transform etc. may be examined. The results can be compared with the existing fractional transforms. For further compression the quantized coefficients can be entropy encoded. By entropy encoding more compression may be achieved. And for the case of encryption, using random mask encoding the security strength may further increased.

REFERENCES

[1] A. B. Watson, *"Image Compression using the DCT"*, Mathematica Journal, vol. 8, pp. 81-88, 1995.

[2] A. C. McBride and F.H. Keer, *"On Namia's Fractional Fourier Transform"*, IMA Journal of Applied Mathematics, vol. 239, pp. 159-175, 1987.

[3] A. J. Richardson, C. Risien and F.A. Shillington, "*Using self-organizing maps to identify patterns in satellite imagery*", Progress in Oceanography, vol. 59 , pp. 223–239, 2003.

[4] A. K. Jain, "*Fundamentals of Digital Image Processing*", Prentice-Hall Incorporated, Englewood Cliffs, 1989.

[5] A. S. Alghamdi, H. Ullah, M. U. Khan, I. Ahemad and K. Alnafajan , "*Satellite Image Encryption for C4I System*", International Journal of the Physical Sciences, vol. 6, no. 17, pp. 4255-4263, 2011.

[6] A. W. Lohmann, D. Mendlovic, Z. Zalevsky and R.G. Dorsch, "*Some important fractional transformations for signal processing*", Optical Communication, vol. 125, pp. 18-20, 1996.

[7] A.W. Lohmann, Z. Zalevsky and D. Mendlovic, "*Synthesis of Pattern Recognition Filters for Fractional Fourier Processing"*, Optics Communications, vol. 128, pp. 199-204, 1996.

[8] B. Purna Kumaria and V.P. Subramanyam Rallabandi, "*Modified patchwork-based watermarking scheme for satellite imagery*" ,Signal Processing, vol. 88, pp. 891–904, 2008.

[9] B. Schneier, "*Applied Cryptograp*hy", John Wiley and Sons, Second Edition, New York, 1996.

[10] B. W. Dickinson and K. Steiglitz, "*Eigenvectors and functions of the discrete Fourier transform*," IEEE Transaction on Acoustic, Speech and Signal Processing, vol. 30, pp. 25-31, 1982.

[11] C. Candan, M. A. Kutay and H.M. Ozaktas, *" Discrete fractional Fourier transform"*, IEEE Transactions on Signal Processing, vol. 48, no. 5, pp. 1329-1337, 2000.

[12] C. D. Clark, S. M. Garrod and M. Parker Pearson, "*Landscape archaeology and Remote Sensing in southern Madagascar*", International Journal of Remote Sensing, vol. 19, no. 8, pp. 1461-1477, 1998.

[13] C. Saravanan and R. Ponalagusamy, *"Lossless Grey-scale Image Compression using Source Symbols Reduction and Huffman Coding"*, International Journal of Image Processing, vol. 3, no. 5, pp. 246-251, 2009.

[14] C.W. Chen et al., "*A Near Lossless Wavelet-Based Compression Scheme for Satellite Images*", IEEE Conference on Computer Science and Information Engineering, pp. 528-532, 2009.

[15] D. Anil, Karthik K.V. and Kumar K.S., "*A Modified Three Level Block Truncation Coding or Image Compression*", International Conference on Pattern Analysis and Intelligent Robotics, 2011.

[16] D. Kaimaris and P. Patias, "*Best period for high spatial resolution satellite images for the detection of marks of buried structures*", The Egyptian Journal of Remote Sensing and Space Sciences, 2012.

[17] D. Mendlovic and H. M. Ozaktas, *" Fractional Fourier Transforms and their optical Implementation-I"*, Journal of Optical Society of America-A, vol. 10, no. 9, pp. 1875-1881, 1993.

[18] D. Landgrebe, "*The evolution of Landsat Data Analysis*", Photogrammetric engineering and remote sensing, vol. 63, No. 7, pp. 859-867, July 1997.

[19] E. Elharar, A. Stern, O. Hadar and B. Javidi, *"A Hybrid Compression Method for Integral Images using Discrete Wavelet Transform and Discrete Cosine Transform"*, Journal of Display Technology, vol. 3, pp. 321-325, 2007.

[20] F. Nencini, A. Garzelli, S. Baronti and L. Alparone, "*Remote sensing image fusion using the curvelet transform*", Information Fusion, vol. 8, pp. 143–156, 2007.

[21] G. Yu, T. Vladimirova and M. Sweeting, "*A New Automatic On-Board Multispectral Image Compression System for Leo Earth Observation Satellites*", IEEE Conference on Digital Signal Processing, pp. 395-398, 2007.

[22] G.M. Nair, "*Role of communications satellites in national development*", IETE Technical Review, vol. 25, pp. 3-8, 2008.

[23] H. M. Ozaktas and D. Mendlovic, *" Fractional Fourier Transforms and their optical Implementation-II"*, Journal of Optical Society of America-A, vol. 10, no. 12, pp. 2522- 2531, 1993.

[24] H.M. Ozaktas, B. Billur, D. Mendlovic, and L. Onural, "*Convolution, Filtering and Multiplexing in Fractional Domains and their Relation to Chirp and Wavelet Transforms*", Journal of Optical Society of America-A, vol. 11, no. 2, pp. 547-559, 1994.

[25] H. M. Ozaktas, O. Arikan, M.A. Kutay and G. Bozdagi, *"Digital Computation of the Fractional Fourier Transforms"* , IEEE Transactions on Signal Processing, vol. 44, no. 9, pp. 2141-2150, 1996.

[26] I. Hacihaliloglu and M. Kartal, "*DCT And DWT Based Image Compression In Remote Sensing Images*", IEEE Conference on Recent Advances in Space Technologies**,** pp. 3856-3858, 2003.

[27] I. S. Yetik and M.A. Kutay, "*Image representation and compression with the Fractional Fourier transform",* Optics Communication, vol. 197, pp. 275-278, 2001.

[28] J. Grazzini, A. Turiel, H. Yahia and I. Herlin," *A multifractal approach for extracting relevant textural areas in satellite meteorological images*", Environmental Modeling & Software, vol. 22, pp. 323-334, 2007.

[29] J. H. McClellan and T. W. Parks, "*Eigenvalue and eigenvector decomposition of the discrete Fourier transform*", IEEE Transactions on Audio and Electroacoustics, vol. 20, pp. 66-74, 1972.

[30] J. H. Pujar and L. M. Kadlaskar, *"A New Lossless Method of Image Compression and Decompression using Huffman Coding Techniques"*, Journal of Theoretical and Applied Information Technology, vol. 15, no. 1, pp. 18-22, 2010.

[31] J. J. Drake , "*Mapping vegetation, soils and geology in semiarid shrublands using spectral matching and mixture modelling of SWIR AVIRIS imagery*", Remote Sensing of Environment, vol. 68, pp.12-25, 1999.

[32] K. Rajesh, K. Roy, S. Sengupta and S. Sinha, "*Satellite image restoration using statistical models*", Signal Processing, vol. 87, pp. 366–373, 2007.

[33] L. B. Almeida, "*The Fractional Fourier Transform and Time-Frequency Repersentation*", IEEE Transaction on Signal Processing, vol. 42, pp. 3084-3091, 1994.

[34] L. Kocarev, "*Chaos-Based Cryptography: A Brief Overview"*, IEEE Circuit System Magazine, vol. 1, pp. 6-21, 2001.

[35] M. A. Sid. Ahmed, "*Image Processing Theory Algorithms and Architectures*", McGraw Hill, International Edition, 1995.

[36] M. Ashtiyani, P. M. Birgani, and H. M. Hosseini, "*Chaos-Based Medical Image Encryption Using Symmetric Cryptography"*, International Conference on Information and Communication Technologies, pp. 1-5, 2008.

[37] M. Liu, "*Digital Image and Video Compression Techniques*", Research Project, Multimedia Authoring, 2003.

[38] M. Jahjah and C. Ulivieri, "*Automatic archaeological feature extraction from satellite VHR images*", Acta Astronautic, vol. 66, pp. 1302–1310, 2010.

[39] M. Sharma, *"Compression Using Huffman Coding"*, International Journal of Computer Science and Network Security, vol. 10, no. 5, 2010.

[40] M. Usama, M. K. Khan, K. Alghathbar and C. Lee "*Chaos-based secure satellite imagery cryptosystem*", Computers and Mathematics with Applications, vol. 60, pp. 326-337, 2010.

[41] O. Akay and G.F. Boudreaux-bastel, "*Fractional Convolution and Correlation via Operator methods and an Application to Detection of Linear FM Signals*", IEEE Trans. on Signal Processing, vol. 49, no. 5, pp. 979-993, 2001.

[42] P. Pellegri, G. Novati and R. Schettini, *"Multispectral loss-less compression using approximation methods"* IEEE International Conference on Image Processing (ICIP), vol. 2, pp. 638-641, 2005.

[43] Ridley, H. M., Atkinson, P. M., Aplin, P., Muller, J.P., and Dowman, I.,"*Evaluating the potential of the forthcoming commercial U.S. high-resolution satellite sensor imagery at the Ordnance Survey"*, Photogrammetric engineering and remote sensing, vol. 63, No 8, pp. 997-1005, 1997.

[44] R. C. Gonzalez and R. E. Woods, "*Digital Image Processing*", Addison-Wesley Co., 1991.

[45] R. Hassan and B. Nath, "*Data compression using Huffman coding-A Novel Approach"*, International Conference on Applied Computing, vol. 2, pp.143-148, 2005.

[46] R. Saxena and K. Singh, *"Fractional Fourier transform: A novel tool for signal processing"*, Indian Institute of Science, vol. 85, pp. 11-26, 2005.

[47] S. A. Coron and M.R. Dagnino, "*Bi-Level Image Compression Estimating the Markov Order of Dependencies*", IEEE Journal of selected topics in Signal Processing, vol. 4, pp. 605-611, 2010.

[48] S. C. Pei and M. H. Yeh," *Discrete fractional Fourier transform"* IEEE International Symposium on Circuits and Systems, vol. 2, pp. 536-539, 1996.

[49] S. C. Pei and M. H. Yeh, "*Two dimensional discrete fractional Fourier transform*", Signal Processing, vol. 67, pp. 99-108, 1998.

[50] S.C. Pei, M.H. Yeh and C.C. Tseng, *" Discrete fractional Fourier transform Based on Orthognal Projections"* , IEEE Transactions on Signal Processing, vol. 47, pp. 1335- 1348, 1999.

[51] S. C. Pei and J. J. Ding, "*Closed-Form Discrete Fractional and Affine Fourier Transforms*" IEEE Transactions On Signal Processing, vol. 48, pp. 1338-1353, 2000.

[52] S. C. Pei, M.H. Yeh, "*The Discrete Fractional Cosine and Sine Transform*", IEEE Transaction on Signal Processing, vol. 49, pp. 1198-1207, 2001.

[53] S. Li and X. Zheng, "*On The Security of An Image Encryption Method"*, IEEE International Conference on Image Processing, vol. 2, pp. 925 928, 2002.

[54] S. Sarmaha and Dhruba K. Bhattacharyya, "*A grid-density based technique for finding clusters in satellite image*", Pattern Recognition Letters, vol. 33, pp. 589-604, 2012.

[55] T. Alieva and M. J. Bastiaans, "*Fractional Cosine and Sine Transform in Relation to Fractional Fourier and Hartley Transform*", IEEE symposium on Signal Processing and its Applications, Paris, France, pp. 561-564, 2003.

[56] T. H. Tsai and L. T. Tsui, " *REG2000 Encoder Architecture Design with Fast EBCOT Algorithm*" IEEE International Symposium on VLSI design, pp. 279-282, 2005.

[57] U. B. Shankar, *"Image compression techniques"*, International Journal of Information Technology and Knowledge Management, vol. 2, pp. 265-269, 2010.

[58] V. Namias, "*The fractional order Fourier transform and its application to quantum mechanics*," Journal of Institute of Mathematics and its Applications, vol. 25, pp. 241-265, 1980.

[59] V. Namias, *"Fractionalization of Hankel Transforms"*, Journal of the Institute of Math Applications, vol. 26, pp. 187-197, 1980.

[59] V.A. Narayanan and K.M.M. Prabhu, *"The Fractional Fourier transform: theory, implementation and error analysis"*, Microprocessors and Microsystems, vol. 27, pp. 511-521, 2003.

[60] X. Delaunay, M. Chabert, V. Charvillat and G. Morin, "*Satellite image compression by post-transforms in the wavelet domain*", Journal for Signal Processing, vol. 90, pp. 599-610, 2010.

[61] X. Zhang, G. Zhu, S. Ma, "*Remote-sensing image encryption in hybrid domains*" Optics Communications, vol. 285, pp. 1736–1743, 2012.